VACUUM RABI SPLITTING IN A COMPACT NEAR-CONCENTRIC CAVITY

by

FLORENTIN THIERRY ADAM

*(M.S. (Subatomic Physics), Université Claude Bernard Lyon 1,
Magistère de Physique Fondamentale d'Orsay, Université Paris-Sud XI)*

A THESIS SUBMITTED FOR THE DEGREE OF

DOCTOR OF PHILOSOPHY

CENTRE FOR QUANTUM TECHNOLOGIES
NATIONAL UNIVERSITY OF SINGAPORE

2024

Thesis Advisor:
Professor Christian KURTSIEFER

Examiners:
Associate Professor David WILKOWSKI
Associate Professor Rainer DUMKE
Professor Christoph WESTBROOK, CNRS Institut d'Optique

Declaration

I hereby declare that this thesis is my original work and it has been written by me in its entirety. I have duly acknowledged all the sources of information which have been used in the thesis.

This thesis has also not been submitted for any degree in any university previously.

Florentin Thierry ADAM

May 19, 2024

Acknowledgments

I would like to express my gratitude to my PhD advisor, Professor Christian Kurtsiefer, for trusting me with this project and supporting me throughout the journey. Special thanks to Adrian, who taught me everything there is to know in a quantum optics lab, your guidance and expertise have been invaluable for the project. I am also grateful to the members of the Quantum Optics Group, especially my office mates at #01-04, for their camaraderie and collaboration.

On a personal note, je remercie ma famille, dont le soutien et les encouragements ont été décisifs durant les temps difficiles malgré la très longue distance et le décalage horaire. Special thanks to my partner, for the countless moments shared and the emotional support in times of need, for the discovery of various food places, and for indulging in a coffee obsession together. Alex, I want to express my sincere thanks for your help and dedicated support, for all the bad jokes (that were not that bad in the end), and for all the games and singing we enjoyed together. Long, thank you very much for your support, for the many endless gathering days on the weekends, and for introducing me to a new addiction: board games. Alfred, merci beaucoup pour ces longs appels vidéo menant à maintes discussions enrichissantes et à une connexion indispensable. Jonathan, Vielen Dank für die Freundlichkeit und alle angenehmen Diskussionen. Sie haben viele Tage erhellt. Bis bald für eine weitere Mindbug Partie! Rishav, I am grateful for the games we shared and your hilarious memes and videos. Amon, danke, dass du mir Calisthenics beigebracht hast – ich bin zuversichtlich, dass die Muscle-ups bald kommen werden. Finally, I extend my gratitude to everyone in CQT, whose interactions enriched my experience during my PhD and my time as part of the CQT Graduate Student Club.

Contents

Abstract

Vacuum Rabi Splitting in a Compact
Near-Concentric Cavity

by

Florentin Thierry ADAM

Doctor of Philosophy

Centre for Quantum Technologies

National University of Singapore

The exploration of strong atom–light interaction is crucial as a building block for engineering quantum computing nodes. Such nodes can be realised with atoms, which require mediators to enhance their interaction with incoming photons, due to their small cross-section. Optical cavities, tools governed by cavity quantum electrodynamics (cavity-QED), fulfil this mediator role by confining the photons in a small mode volume. While a small mode volume can be implemented in conventional high-finesse optical cavities, less-explored configurations, such as near-concentric cavities, also exhibit this feature. Near-concentric cavities provide a unique balance of a small mode volume and significant optical access for atom manipulation, while only requiring low finesse to operate. However, it is sensitive to misalignment when operating close to the concentric regime.

This thesis presents a near-concentric optical cavity system to address this longitudinal and transverse stability close to the concentric regime. The cavity system features a compact cage-like tensegrity mirror support structure, with a cavity length of 11 mm. This structure displays a residual cavity length variation of $\delta L_{C,rms} = 0.36(2)\,\text{Å}$ at a close critical distance from the concentric regime of $d = 1.06(5)\,\mu\text{m}$, while allowing control of all necessary degrees of freedom. With this stability, vacuum Rabi splitting is observed in the presence of trapped atoms. For 10 atoms trapped in the cavity, the atom–cavity coupling strength is $g_{10} = 2\pi \times 25.4(4)\,\text{MHz}$, resulting in the atom–cavity system being in the strong coupling regime and displaying a cooperativity of $C = 5.1(5)$.

This near-concentric cavity geometry provides a viable alternative to near-planar cavity geometries for cavity-QED experiments. One notable advantage is its high optical access to the centre of the cavity mode, beneficial for atomic state preparation in quantum information processing schemes. Leveraging the mechanical stability and strong interaction capabilities of the developed near-concentric cavity opens up new possibilities for implementing quantum logic gates with low-finesse resonators.

List of Figures

List of Tables

Chapter 1

Introduction

At the end of the 19th century, we thought we knew all there is to know about physics. Only two major problems remained, both coming from Maxwell's equations. The first one: Maxwell's equations are not invariant by Galilean transformation. This led to the search for an absolute wave medium named ether, as it was assumed that all waves require a medium to propagate. However, Michelson's experiment in 1881 [1], and later Morley's in 1887 [2], showed that the speed of light is independent of the reference frame, which is in opposition to the known theory's predictions. The reference frame independence of the speed of light only holds if the hypothesis of the length contraction, enunciated by George Fitzgerald in 1889, Voigt two years earlier, and Hendrik Antoon Lorentz independently in 1892 [3], is taken into account. We have to wait until 1905 for Albert Einstein [4] to deliver the final blow to the ether model, which led to the abandon of the notion of absolute time: special relativity was born, and later on general relativity in 1916 [5]. Many other famous physicists, such as Henry Poincaré and Paul Langevin, contributed to the establishment of this new theory.

The second problem is related to the conception of matter and its thermal radiation. From the discovery of the electron by William Crookes in 1886, two models of the atom coexisted at the same time: on the one hand, Joseph John Thomson proposed a point-like electron in a positive ball [6]; on the other hand, Ernest Rutherford, who conducted his gold foil scattering experiment in 1909, later proposed a planetary model where the electron orbits around the nucleus [7]. The latter model supplanted Thomson's model. However, Rutherford's model cannot account for the stability of the atom where the electron should continually radiate energy and collapse into the nucleus, nor explain the discretisation of the spectral lines. This model is later quantised by Niels Bohr in 1913 [8]. Conjointly, it was also known from thermodynamics that emission spectra of heated bodies also experience divergent results when Wien's law [9] is applied for long wavelengths in 1896. Four years later, Lord Rayleigh with the help of James Jeans came up with the famous Rayleigh–Jeans law [10] with the use of statistical mechanics, stating that the radiating power of electromagnetic waves is proportional to the temperature and inversely proportional to the wavelength to the power of four. However, this law produces abnormal results for short wavelength, later referred as "the ultraviolet catastrophe" by Paul Ehrenfest. Once again in 1905, Albert Einstein proposes a corpuscular description of light [11] which agreed with the observations and led to a wave-particle duality description of light, making use of Max Planck quantisation of energy [12]. Later on in 1923, Louis De Broglie extended this wave-particle duality to matter [13], which was formulated in the form of a diffusion equation by Erwin Schrödinger in 1926 [14] and in the form of a matrix by Werner Heisenberg in 1925 [15]. These two models are reunited in 1930 by Paul Dirac as he demonstrated that they are two representations of the same linear algebra [16], a work which was preceded by John von Neumann a few years earlier but only published in 1932 [17]. Quantum mechanics was born.

One discovery leading to another, from this new conceptualisation of physics, the field grew larger and ramified to several subfields. In particular, atom-light interaction became quite prominent at the end of the 20^{th} century. We learnt how to tame matter, first by slowing it down using laser light in 1975 by Hänsch and Schawlow [18]. Thereafter, the prolific 80's brought significant achievements: from the complete stop of neutral sodium atoms using counter-propagating laser beams by Phillips and Metcalf in 1982 [19], to the first realisation of an optical molasses of sodium atoms by Chu in 1985 [20]. We first trapped sodium atoms using a magneto-optical trap, utilising the atomic structure, by Raab in 1987 [21] which brought down the atom's temperature to $600\,\mu\mathrm{K}$ with a density of $2 \times 10^{11}\,\mathrm{atoms\,cm^{-3}}$. In addition to these techniques, at the same time, other tools and properties are discovered to enhance the interface with matter. That is the case for cavity quantum electrodynamics (cavity-QED), a subfield of quantum electrodynamics theory, the latter being fully developped by Richard Feynman, Julian Schwinger and Tomonaga Shin'ichirō in the 40's [22]. With the Jaynes-Cummings model, introduced in 1963 [23], at its core, cavity-QED aims to utilise resonators to amplify the electric field strength of a photon to interact with confined atoms. Inherently, the scattering probability of the photon increases as the number of round trips of the photon inside the cavity increases. One of the pioneer experiments using cavity-QED is the work of Serge Haroche in the 80's [24]. These first demonstrations were conducted with Rydberg atoms in the microwave regime, and showcased the capability to manipulate a single atom in a cavity system. After these first steps, several experiments with different cavity systems started to appear, targeting different atomic regimes and various cavity configurations. We would note the work of Kimble in 1999 [25] with caesium atoms who led the field of neutral atoms in cavity-QED. Since then, optical resonator designs for atom interaction diversified [26]. Notable cavity configurations are: the well-known Fabry-Pérot cavities such as the one used by Serge Haroche, where two highly reflective mirrors form the resonator which couple to atoms trapped within it, the microtoroid and bottle resonators [27], which employ whispering-gallery modes circulating in glass structures to couple with atoms, and photonic-crystal cavities [28], where atoms are trapped near the surface of the crystal utilising standing-wave optical tweezers and couple to the electromagnetic field propagating inside the crystal. Recent works explore the capabilities offered by such cavity systems, e.g., displaying strong interaction with single atoms to generate coherent light field, such as Schrödinger cat-like fields via an optical wave-mixing scheme [29], or making use of the defined cavity modes to probe collective behavior of atom arrays [30], or utilising the cavity as a mediating tool to sustain narrow resonances in a system with strong inhomogeneous broadening [31]. Additionally, the highly sought-after quantum logic gate can be effectively operated with a cavity system [32]. The ability to operate quantum logic gates is essential for building a quantum network, and an atom–cavity system would excel as a computing node in this context, due to the strong coupling interaction displayed by the system as well as the optical frequency range in used to interface with atomic transition. Moreover, as the number of platforms available to create quantum logic gates grows [33, 34, 35], a lot of efforts are put to make systems of different nature coincide together, each as nodes of a larger quantum network [36, 37].

In this thesis, we follow the footsteps of developing a compact Fabry-Pérot cavity exhibiting strong atom–light interaction, making it an ideal candidate to act as a qubit node hosting a logical computation. Our cavity is operated at a particular Fabry-Pérot geometrical regime called near-concentric (NC), where the length of the cavity is close to the sum of the spherical mirrors' radii of curvature and the cavity modes are strongly focused at the center. Compared to near-planar microcavities, NC cavities provide easy optical access through the relatively large mirror separation, while retaining the highly confined light field. However, as opposed to the former, NC cavities are challenging to work with, as transverse displacement of the mirrors affects the cavity resonance. As the optical cavity resonance needs to have a well-defined relation to fixed atomic resonances in cavity-QED applications, the mechanical cavity stability is critical. In NC cavities, there is the additional requirement for transverse adjustability and stability, leading to the need for control of three degrees of freedom for relative mirror positions.

Firstly, in Chapter 2, we present a brief review of the dynamics of an atom–cavity system via cavity-QED, and we highlight the unique aspects of the near-concentric geometry. Following this, Chapter 3 covers the design choices and limitations of our NC cavity, as well as the associated challenges. In Chapter 4, we discuss the various tools and techniques used to characterise the performance of the cavity. Finally, in Chapter 5, we showcase the observed vacuum Rabi splitting, resulting from Rubidium atoms interacting with the cavity mode, and discuss further applications of the system.

Chapter 2

Theory

2.1 Dynamics and Hamiltonian

In this chapter, we provide a brief summary of the theoretical concepts of cavity-QED. The dynamics of the interaction between a two-level system and a cavity is first introduced using a non-dissipative model, before discussing the more realistic dissipative model. Then, the different configurations of the optical cavity are outlined, with particular focus on the near-concentric (NC) regime and the different atom–cavity coupling regions.

2.1.1 Jaynes-Cummings Model

In the absence of dissipation, the Jaynes-Cummings Hamiltonian [38] describes the interaction of a two-level system, e.g., an atom, with a quantised electromagnetic field resonant to the $|g\rangle \rightarrow |e\rangle$ dipole transition, e.g., a cavity mode. For an atom with ground state $|g\rangle$ and excited state $|e\rangle$, the atomic dipole operator $\mathbf{d}$ is defined as

$$\mathbf{d} = \mu_{ge}(\sigma^\dagger + \sigma)\mathbf{e_d} \ , \tag{2.1}$$

where μ_{ge} is the atomic dipole moment, $\sigma^\dagger = |e\rangle\langle g|$ and $\sigma = |g\rangle\langle e|$ are the raising and lowering Pauli operators between the ground an excited states of the atom, and $\mathbf{e_d}$ the polarisation direction of the dipole. For a cavity mode, the confined electric field $\mathbf{E}$ is given as

$$\mathbf{E} = E_0(a^\dagger + a)\mathbf{e}_\lambda \ , \tag{2.2}$$

where E_0 is the electric field amplitude, $a^\dagger$ and a are the photon creation and annihilation operators in the cavity mode, and $\mathbf{e}_\lambda$ the polarisation direction of the electric field. The interaction between the dipole operator and the confined electric field is given by the interaction Hamiltonian $\mathcal{H}_{int}$, and its form resembles the energy associated with a classical dipole in a radiation field:

$$\begin{aligned}\mathcal{H}_{int} &= -\mathbf{d}\cdot\mathbf{E} \\ &= \hbar g(\sigma^\dagger a^\dagger + \sigma^\dagger a + \sigma a^\dagger + \sigma a) \\ &\approx \hbar g\left(\sigma^\dagger a + \sigma a^\dagger\right) ,\end{aligned} \tag{2.3}$$

where g is the atom–cavity coupling strength, and the directions for the dipole and the polarisation of the electric field are assumed to be identical for simplicity, i.e.: $\mathbf{e}_\lambda = \mathbf{e}_\mathbf{d}$. The last line is obtained using the rotating-wave approximation. From this interaction Hamiltonian, ignoring a global phase term, the atom–cavity coupling strength g is given by

$$g = \frac{\mu_{ge}E_0}{\hbar} = \mu_{ge}\sqrt{\frac{\omega_c}{2\epsilon_0\hbar V}} , \tag{2.4}$$

where the effective mode volume V quantifies the confinement of the electric field E_0 within the cavity [39], i.e., a smaller mode volume indicates a more confined electric field, and is determined by the cavity geometry.

The total Jaynes-Cummings Hamiltonian is obtained by combining the interaction Hamilotnian with the bare atom and cavity Hamiltonians such that

$$\begin{aligned}\mathcal{H}_{JC} &= \mathcal{H}_a + \mathcal{H}_{cav} + \mathcal{H}_{int} \\ &= \hbar\omega_a\, \sigma^\dagger\sigma + \hbar\omega_c\, a^\dagger a + \hbar g\left(\sigma^\dagger a + \sigma a^\dagger\right) ,\end{aligned} \tag{2.5}$$

where ω_a and ω_c are the angular frequencies of the atom and the cavity, respectively. This Hamiltonian can be solved analytically by diagonalising the Equation 2.5. The respective eigenstates are given by the product of the atomic and cavity eigenstates $|g,n\rangle$ and $|e,n-1\rangle$

$$\begin{aligned}|+,n\rangle &= \sin\theta\,|g,n\rangle + \cos\theta\,|e,n-1\rangle , \\ |-,n\rangle &= \cos\theta\,|g,n\rangle - \sin\theta\,|e,n-1\rangle ,\end{aligned} \tag{2.6}$$

where $\pm$ denotes the two normal modes, n reflects the total excitation quanta of the system, and θ is the mixing angle that denotes the relative contribution of the atom

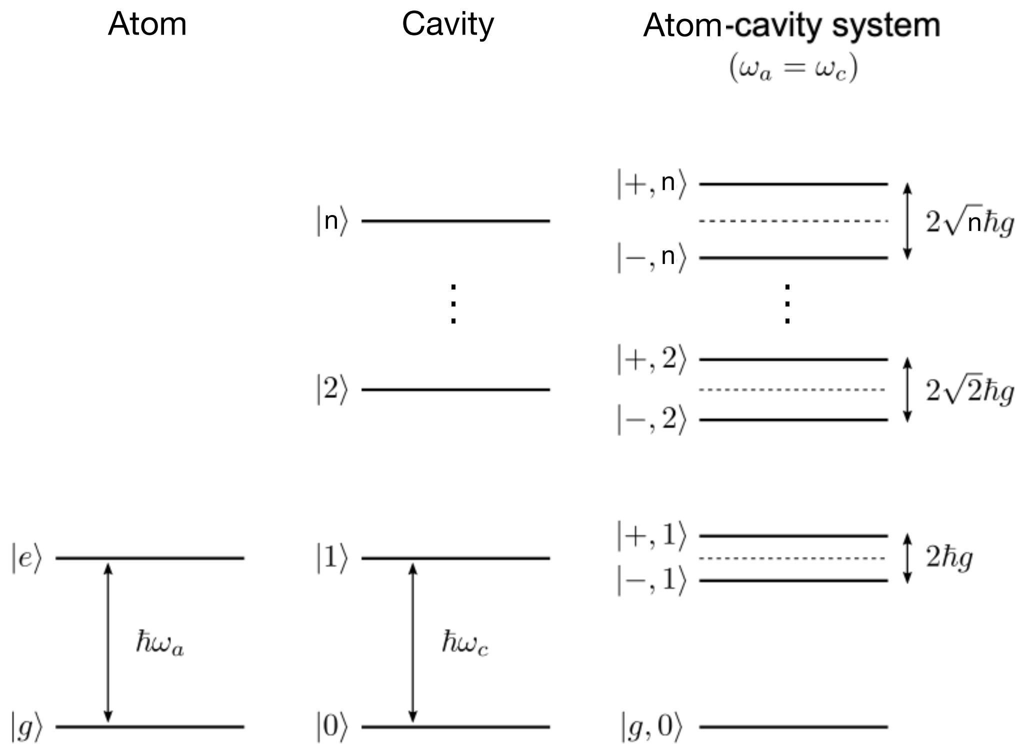

Figure 2.1: The energy level diagram of the bare atom, cavity, and coupled system. The coupled system is also commonly referred to as Jaynes-Cummings ladder.

and the cavity to the coupled states. θ is proportional to the coupling strength g and the atom–cavity detuning $\Delta_{ac} = \omega_a - \omega_c$ such that

$$\theta = \arctan \frac{2g\sqrt{n}}{\Delta_{ac} + \sqrt{4g^2 n + \Delta_{ac}^2}} \ . \tag{2.7}$$

In the limit of no interaction, i.e., the coupling strength $g \to 0$, the eigenstates of the system are simply $|g, n\rangle$ and $|e, n-1\rangle$.

The level diagram of the coupled energy states is shown in Figure 2.1, and the eigenvalues are given by:

$$E_{\pm,n} = n\hbar\omega_c + \hbar\frac{\Delta_{ac}}{2} \pm \frac{\hbar}{2}\sqrt{\Omega_n^2 + \Delta_{ac}^2} \ , \tag{2.8}$$

where $\Omega_n = 2g\sqrt{n}$ is the n-quantum Rabi frequency.

On resonance ($\Delta_{ac} = 0$), the coupling of the atom and the cavity creates a splitting of the energy levels by $2\sqrt{n}\hbar g$ (see Figure 2.1), with the eigenstates

$$|\pm, n\rangle = \frac{1}{\sqrt{2}}(|g, n\rangle \pm |e, n-1\rangle) \ . \tag{2.9}$$

This doublet of energy levels is called the vacuum-Rabi splitting [40]. From this splitting, the photon blockade effect [41] can be observed, where the excitation of the atom–cavity system by a single photon blocks the transmission of subsequent photons for a specific laser frequency. Furthermore, the superposition state given by Equation 2.9 informs us on the dynamics of the coupled atom–cavity system. For example, assume a resonant atom in the excited state $|e\rangle$ inside a cavity with $n-1$ photons. The initial state $|e, n-1\rangle$ is a linear superposition of the eigenstates

$$|\Psi(t=0)\rangle = |e, n-1\rangle = \frac{1}{\sqrt{2}}(|+, n\rangle - |-, n\rangle) \ . \tag{2.10}$$

Calculating the probability of the atom being in the excited state $|e\rangle$ at a certain time t gives us:

$$P_{|e\rangle}(t) = \cos^2\left(\frac{\Omega_n t}{2}\right) \ . \tag{2.11}$$

This indicates that the system undergoes an oscillation between the states $|g, n\rangle$ and $|e, n-1\rangle$ at a Rabi frequency of Ω_n. When the cavity is initially in the vacuum state $n-1=0$, $\Omega_{n=1} = 2g$ is referred as the vacuum-Rabi frequency. Note that for experimental observation of the vacuum-Rabi oscillation, the latter needs to be faster than all dissipative processes in the system, as explained in the next section.

2.1.2 Damped system

In the real atom–cavity system, dissipation and decoherence occur as the system couples to its environment. The environment considered is the quantum electromagnetic vacuum, consisting of a continuous background of modes, and introduces losses via two loss channels.

First, the atomic polarisation decays at the rate γ. This results either from an atomic decay to an uncoupled state, which is avoided in our system by using a closed loop transition, or from the emission of a photon by the atom into free space rather than the cavity mode. For the latter, consider the solid angle $\Delta\Omega$ of a cavity and assume the atoms radiates isotropically, the atomic decay rate is given by:

$$\gamma = \frac{\Gamma}{2}\left(1 - \frac{\Delta\Omega}{4\pi}\right) \ , \tag{2.12}$$

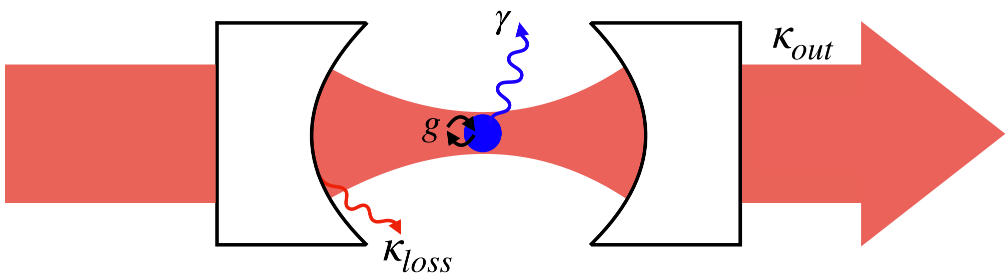

Figure 2.2: The atom–cavity interaction scheme with the different loss channels. Here, γ represents the loss of an atom inside the cavity. κ_{loss} and κ_{out} represent the losses due to the mirror's imperfection. g represents the interaction between an atom and the cavity field.

where Γ is the free-space spontaneous emission rate. Furthermore, from coupling the atomic dipole to the free-space modes [42], the atomic decay rate can be written as

$$\gamma = \frac{\mu_{ge}^2 \omega_a^3}{6\pi\epsilon_0 \hbar c^3} \ . \tag{2.13}$$

in terms of atomic dipole moment and atomic frequency.

The second loss channel is due to the decay of the cavity mode's electric field as a result of scattering and absorption losses κ_{loss} by both mirrors, and coupling to a propagating field mode κ_{out} (see Figure 2.2). The total decay rate is $\kappa = \kappa_{loss} + \kappa_{out}$. Additionally, considering that the resonance frequency broadening is a consequence of the energy decay inside the cavity, κ amounts to half of the cavity linewidth $\delta\nu$, which can be related to the cavity finesse $\mathcal{F}$. The latter represents the number of round trips a photon undergoes inside a resonator (see Section 2.2). κ can be written in terms of the cavity parameters

$$\kappa = 2\pi\frac{\delta\nu}{2} = \frac{\pi c}{2L\mathcal{F}} \ , \tag{2.14}$$

where L is the cavity length. This equation shows that the higher the finesse of a resonator, the longer photons remain trapped inside the cavity.

To solve the dynamics of the open atom–cavity system, the standard approach is to describe the evolution of the density operator ρ of the system via a master equation in the Linblad form [43]

$$\dot{\rho} = \frac{1}{i\hbar}[\mathcal{H}_{JC}, \rho] + \sum_i \left[L_i \rho L_i^\dagger - \frac{1}{2}(L_i^\dagger L_i \rho + \rho L_i^\dagger L_i) \right] \ , \tag{2.15}$$

where L_i are the jump operators and describe the respective decays in the system, and $L_1 = \sqrt{2\gamma}\sigma$ and $L_2 = \sqrt{2\kappa}a$ correspond to the atomic and cavity decays, respectively. The degree of coherence of the system then depends on the ratio of the rates (g, κ, γ), which varies for different solutions of the master equation, and is expressed in terms of the cooperativity factor

$$C = \frac{g^2}{2\kappa\gamma} \ . \tag{2.16}$$

Note that the cooperativity is sometimes defined without the factor 2 in the denominator such that $C = \eta_P$, where η_P is the Purcell factor. The Purcell factor corresponds to the enhancement of the scattering probability of a photon undergoing round trips in the cavity [44, 45]. Besides, the inverse of C is the critical atom number, below which the transmission of the cavity decreases substantially. In addition to the master equation approach, it is also possible to solve the dynamics of the system using an effective Hamiltonian [45].

2.1.3 Different coupling regimes

From the ratio of the rates (g, κ, γ), three coupling regimes are observed for an atom–cavity system, namely the weak, Purcell, and strong coupling regimes. We give a basic explanation of each regime in this section.

Weak coupling regime

When $g \ll (\kappa, \gamma)$, the losses dominate the dynamics and the atom–cavity system is uncoupled. Therefore, the interaction of the atom with the cavity can be ignored and the dynamics of the atom is close to a free-space atom. The vacuum-Rabi splitting cannot be observed in this regime.

Purcell regime

When $\gamma \ll g \ll \kappa$ and $C \gg 1$, the atom–cavity system enters the Purcell regime, or fast cavity regime. In this regime, a photon emitted into a cavity mode is lost before it can be absorbed by an atom, therefore the vacuum-Rabi splitting still cannot be observed. However, the presence of the cavity strongly impacts the atomic decay rate γ. The latter can be increased [46] or decreased [47] depending on the detuning of the cavity resonance compared to the targeted atomic resonant frequency.

The modified atomic decay rate can be derived by solving Equation 2.15 [48]

$$\gamma_c = \frac{g^2\kappa}{\kappa^2 + \Delta_{ac}^2} \ . \tag{2.17}$$

On resonance, the modified atomic decay rate can be enhanced and much larger than the original atomic decay rate

$$\gamma_c = 2C\gamma \ , \tag{2.18}$$

which means that the cavity modes dominate the radiative emission over the free-space modes. This effect has been exploited for different applications, especially to create single photon sources into well-defined optical modes [49, 50].

Strong coupling regime

When $g \gg (\kappa, \gamma)$, which implies $C \gg 1$, the atom–cavity system is in the strong coupling regime, and the dynamics of the system is led by the coherent exchange of energy between the atom and the cavity. As the atom-photon coupling strength g is higher than the losses, the vacuum-Rabi splitting can be observed. However, the generalised Rabi frequency slightly differs from the ideal case as discussed in Section 2.1.1. The rate $\Omega_{n=1}$ at which the atom exchanges energy with the cavity is now dependent on the detuning between the two

$$\Omega_{n=1} = \sqrt{4g^2 + \Delta_{ac}^2} \ . \tag{2.19}$$

In addition, for interaction with more than one atom, the Jaynes-Cummings model can be generalised to the Tavis-Cummings model [51, 52], where the coupling strength of the atom–cavity system scales with the square root of the number of atoms N, represented by $g_N = \sqrt{N}g$. This scaling results in an increased cooperativity of $C_N = N \times C$. Consequently, augmenting the number of atoms within the cavity becomes advantageous for attaining higher cooperativity regimes. It also serves to offset potential losses attributed to the cavity decay rate κ, ultimately enabling the system to achieve the strong coupling regime.

2.2 Fabry-Pérot cavities and their characteristics

To confine light, the most common tools used are Fabry-Pérot cavities, or optical cavities, and consist of two mirrors with radii R_1 and R_2, separated by a distance

L. Once a photon enters the cavity, it will bounce back and forth between the two mirrors and will undergo a number $N_{rt} = \mathcal{F}/\pi$ of round trips inside the resonator. The cavity finesse is

$$\mathcal{F} = \frac{\nu_{\mathrm{FSR}}}{\delta\nu} = \frac{\pi(\mathcal{R}_1\mathcal{R}_2)^{1/4}}{1-\sqrt{\mathcal{R}_1\mathcal{R}_2}} , \tag{2.20}$$

where $\nu_{\mathrm{FSR}} = c/2L$ is the free spectral range and is defined as the frequency spacing between two transmission or reflection maxima (see Figure 2.3), $\delta\nu$ is the cavity linewidth or full width at half maximum (FWHM) of the transmission spectrum, and $\mathcal{R}_1$ and $\mathcal{R}_2$ are the mirror reflectivities.

2.2.1 The different geometrical regimes

To sustain a light field inside the cavity or cavity mode, i.e., the mode retains its size and divergence even after several round trips, a resonator needs to satisfy stability requirements. The stability parameters G_1 and G_2 of a Fabry-Pérot cavity [53] are defined such that

$$0 < G_1 G_2 < 1 \tag{2.21}$$

and

$$G_i = 1 - \frac{L}{R_i} , \tag{2.22}$$

with $i = (1, 2)$. The different types of cavities are represented in Figure 2.4 with respect to their corresponding stability parameters. From Equation 2.21, the region

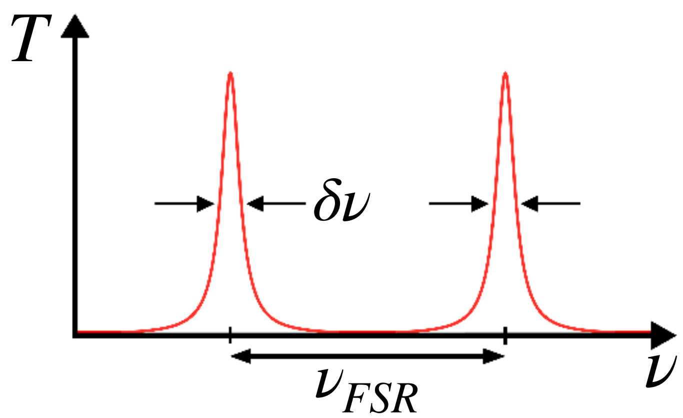

Figure 2.3: The transmission spectrum of a Fabry-Pérot cavity with respect to frequency ν. Here, $\delta\nu$ represents the FWHM of the transmission peaks, and ν_{FSR} is the frequency spacing between two transmission maxima.

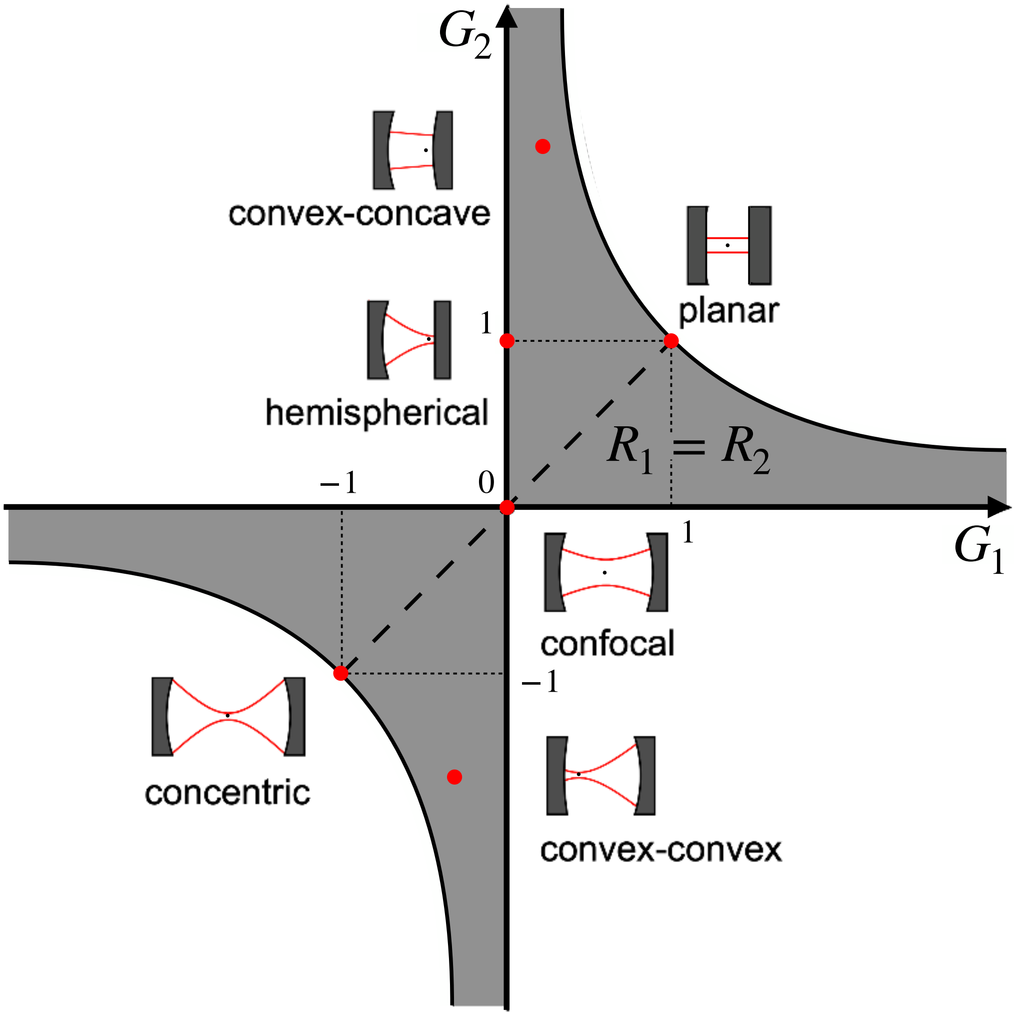

Figure 2.4: The stability diagram of Fabry-Perot cavities. The cavities in the grey area are stable. The configurations of interest lie on the diagonal dashed line, which represents symmetrical cavities with $R = R_1 = R_2$. From these regimes, the near-planar and near-concentric designs are common choices in atom–cavity experiments.

of stable cavity configurations is the shaded region shown in Figure 2.4 corresponding to the constraint $0 < G_1 G_2 < 1$. In this region, where spherical boundary conditions are set by the mirrors, the sustained cavity modes belong to the Gaussian beam family. Beyond this region, cavities are unstable and cannot sustain their modes.

Frequently studied configurations include symmetrical cavities, where $R = R_1 = R_2$. Of particular interest for this thesis are the concentric and near-concentric configurations, as they offer highly focused cavity modes. However, concentric cavities, with stability parameters $G_1 = G_2 = -1$, are only partially stable with respect to the radial isotropic modes. In contrast, near-concentric cavities, positioned in close proximity to this concentric point, fall within the stable regime of Fabry-Pérot resonators. The distance from the concentric point is quantified by the critical distance d

$$d = 2R - L \ , \tag{2.23}$$

where $d = 0$ at the concentric point, and with the stability parameter

$$G_{NC} = -1 + \frac{d}{R} \ . \tag{2.24}$$

Both the coupling strength g and the decay rate κ depend on the cavity geometry. The cavity length L directly impacts κ (see Equation 2.14) and is also related to the mode volume V of a cavity by

$$V = \frac{1}{2}\sigma_w L = \frac{1}{4}\pi w_0^2 L \ , \tag{2.25}$$

where $\sigma_w = \pi w_0^2/2$ is the focal point of a Gaussian beam in free-space [54], and w_0 is the cavity beamwaist

$$w_0^2 = \frac{\lambda L}{\pi}\sqrt{\frac{2R}{L} - 1} \ . \tag{2.26}$$

As shown in Equation 2.4, maintaining a small mode volume V is crucial for achieving a high coupling strength g. This can be accomplished through two Fabry-Pérot configurations, namely the near-planar regime and the near-concentric regime, as illustrated in Figure 2.5.

- **Near-planar cavity:** The mirrors' radii of curvature are much bigger than the cavity length, $L \ll R$. The mode volume approximates to

  $$V_{Pl} \approx \frac{\lambda}{8}\sqrt{2RL^3} \ . \tag{2.27}$$

  However, the use of this geometry is usually limited by the required small cavity length to achieve small V [55]. The lack of optical access due to small cavity lengths makes it difficult to implement additional trapping or probing techniques to control the trapped atoms.

- **Near-concentric cavity:** For small critical distance, $d \ll R$, using the paraxial approximation, the cavity waist radius approximates to

  $$w_0^2 = \frac{\lambda(2R - d)}{2\pi}\sqrt{\frac{d}{2R - d}} \approx \frac{\lambda L}{\pi}\sqrt{\frac{Rd}{2}} \ , \tag{2.28}$$

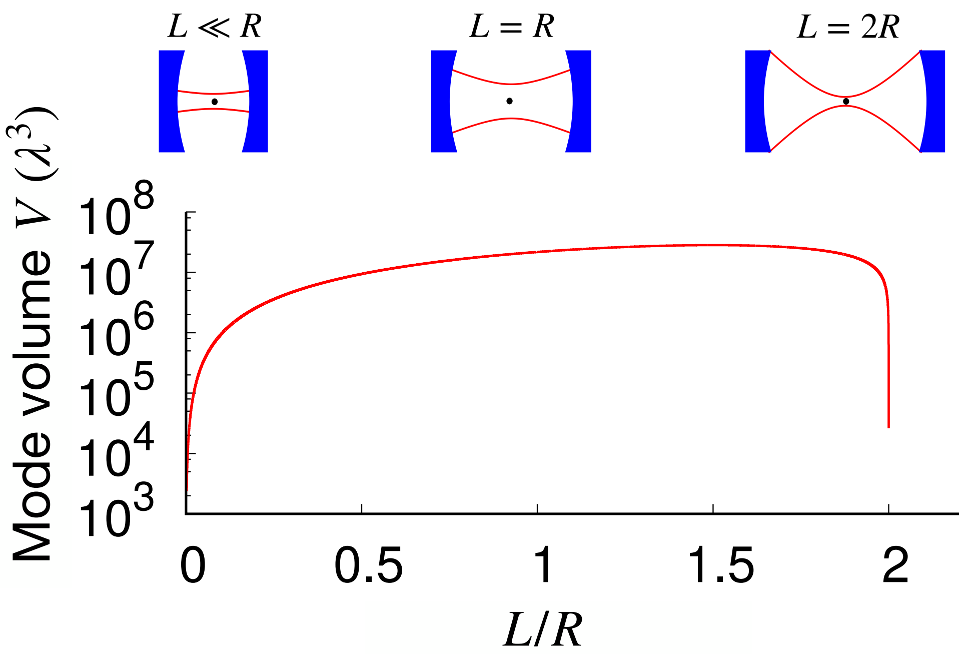

Figure 2.5: The mode volume variation in symmetrical cavities with respect to the length-to-radius ratio For this graph, the mirror radius and wavelength are set to $R = 5.5\,\mathrm{mm}$ and $\lambda = 780\,\mathrm{nm}$, respectively.

leading to the modified mode volume

$$V_{NC} \approx \frac{\pi}{4}\left(\frac{\lambda}{\pi}\sqrt{\frac{Rd}{2}}\right) L \ . \tag{2.29}$$

Due to the geometry of NC cavities, a small mode volume is achievable while still retaining a relatively large optical access in the resonator. A cavity length generally on the order of centimeter is practical for atomic experiments where several lasers need to be added to the system to trap particles. Additionally, compared to near-planar cavities, the strong focusing NC geometry allows the use of lower cavity finesse, as $\mathcal{F} \propto 1/L$ (see Equation 2.14). Lower finesse mirrors are easier and cheaper to manufacture.

2.2.2 Transverse modes frequency spacing

NC cavities exhibit support for various families of Gaussian modes, including Hermit-Gaussians (HG) and Laguerre-Gaussians (LG). This diversity results in the potential observation of transverse mode resonances in the cavity transmission spectrum, showcasing near-degeneracy in resonant frequencies. This near-degeneracy, a distinctive feature of the cavity transverse modes, is of particular interest in NC cavities due to the highly focused cavity modes and small frequency spacing between the cavity transverse modes. Nearing the concentric point, this degeneracy disappears as the Gouy phase of all transverse modes becomes multiples of π, resulting in the overlap of all modes.

As a spherical optical resonator, an straightforward representation of the NC cavity eigenmodes involves the use of LG functions. These functions serve as a complete basis for solutions to the paraxial wave equation [56], and are expressed as LG_{qpl} where q, p, and l are integers and represent the longitudinal, radial and azimuthal components, respectively. The transverse mode profile is expressed through a complex amplitude and takes the form

$$U_{p,l}(\rho,\phi,z) = A_{p,l}\frac{w_0}{w(z)}\left(\frac{\rho}{w(z)}\right)^l \mathcal{L}_p^l\left(\frac{2\rho^2}{w^2(z)}\right)\exp\left(-\frac{\rho^2}{w^2(z)}\right)\exp\left(i\Psi_{p,l}(\rho,\psi,z)\right), \tag{2.30}$$

where $A_{p,l}$ is the normalization constant, $w(z) = w_0\sqrt{1+(z/z_0)^2}$ is the beam radius along the z direction, $z_0 = \pi w_0^2/\lambda$ is the Rayleigh range, and w_0 is the waist radius. $\mathcal{L}_p^l$ is the generalised Laguerre polynomial, and $\Psi_{p,l}(\rho,\phi,z)$ is the real-valued phase of the LG beam

$$\Psi_{p,l}(\rho,\phi,z) = -kz - k\frac{\rho^2}{2R(z)} - l\phi + (2p+l+1)\zeta(z), \tag{2.31}$$

where $R(z) = z + z_0^2/z$ is the radius of curvature for the wavefront, and $\zeta(z) = \arctan(z/z_0)$ is the Gouy phase. The LG modes adhere to boundary conditions set by the two spherical mirror radii R_1 and R_2, aligning their wavefront with the surface of the mirrors. Consequently, the resonance frequencies of the cavity are contingent upon the transverse mode numbers p and l,

$$v_{q,p,l} = \left(q + (2p+l+1)\frac{\Delta\zeta}{\pi}\right)\nu_{FSR}, \tag{2.32}$$

where $\Delta\zeta = \zeta(z_{M2}) - \zeta(z_{M1})$ is the Gouy phase difference between the two cavity mirrors. The resonances are illustrated in Figure 2.6.

The transverse modes of a NC cavity adhere to Equation 2.32, preserving the applicability of the paraxial approximation within our operational range, up to the final stable resonance. The paraxial approximation begins to falter only at very

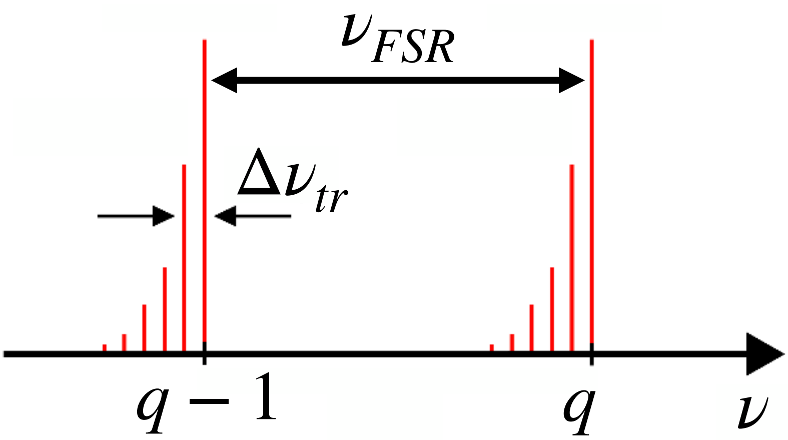

Figure 2.6: The schematic of the cavity transverse mode resonances in the cavity transmission spectrum, being near-degenerate for a frequency spacing $\Delta\nu_{\mathrm{tr}} \ll \nu_{\mathrm{FSR}}$.

short critical distances, as the cavity mode radius $w(z)$ experiences swift divergence along the cavity axis owing to the limited Rayleigh range z_0, prompting potential non-paraxial treatments [57].

From Equation 2.32, the transverse mode spacing $\Delta\nu_{tr}$ between the consecutive modes LG_{q00} and LG_{q01} is expressed as

$$\Delta\nu_{tr} = \nu_{q,0,0} - \nu_{q,0,1} = \frac{\nu_{FSR}}{\pi} \arccos\left(1 - \frac{d}{R}\right), \tag{2.33}$$

such that $\Delta\nu_{tr} \to 0$ when $d \to 0$ and the non-degeneracy is recovered at the concentric point, resulting in coresonance of all transverse modes. In addition, for small critical distances, as the transverse mode spacing $\Delta\nu_{\mathrm{tr}}$ reduces, the spacing provides a straightforward measurement of d.

Chapter 3

Designing a near-concentric cavity

This chapter outlines the construction process of a near-concentric (NC) cavity tailored for interaction with the D_2 transition of Rubidium-87 (^{87}Rb). It delves into the detailed characteristics of our cavity system, providing an overview of its previous iterations. Operating in the NC regime demands robust stabilisation in three degrees of freedom due to the highly focused cavity modes. Any shift in the relative position of the two mirrors, either longitudinally or transversely, induces changes in the cavity length, impacting the resonance. This causes difficulties in maintaining the resonance to target a specific atomic transition. Addressing these challenges, our current compact NC cavity design displays significantly lower susceptibility to external mechanical noise compared to earlier iterations [58, 59]. This enables operation in close proximity to the concentric point, up to the last stable resonance. This chapter provides thorough details on assembly and control protocols, with a more in-depth discussion of measurement techniques and results reserved for Chapter 4. In addition, the current cavity structure presented in this Chapter has been published in the Review of Scientific Instruments [60].

3.1 Cavity characteristics

To construct a NC cavity, certain specifications must be established initially. Tailoring the cavity system to resonate with a specific atomic transition is crucial for effective interaction. In our instance, the cavity system is crafted for interaction with the D_2 line of ^{87}Rb, specifically the $5^2\mathrm{S}_{1/2}\ F = 2 \rightarrow 5^2\mathrm{P}_{3/2}\ F' = 3$ transition, ensuring resonances at integer multiples of the wavelength $\lambda = 780.24\,\mathrm{nm}$. The critical parameters for interaction are contingent on the characteristics of the cavity mirrors. The reflectivity and radii of curvature of the mirrors determine the finesse and the length of the cavity, directly influencing the system's coupling strength g (see Equation 2.4) and cavity decay rate κ (see Equation 2.14). Additionally, for trapping neutral Rubidium atoms using a magneto-optical trap (MOT) [61] and a dipole trap [62] (see Section 5.1), the cavity must operate within an ultra-high-vacuum (UHV) environment. To minimise the size of the vacuum system, reduce the size of the coils required for a magneto-optical trap, and optimise optical access facilitated by the NC geometry, we encase the cavity in a glass cuvette. The cuvette features anti-reflection coating, ensuring reflectivity $R < 1\,\%$ at 780 nm, 850 nm, 980 nm, and 1060 nm, with internal dimensions measuring 25 mm × 25 mm × 150 mm. Consequently, the cavity must fit within the cuvette, imposing certain constraints on the characteristics of the cavity mirrors.

3.1.1 Cavity mirrors

The constraints imposed on the NC cavity size dictate the maximum radius of curvature of the cavity mirrors. These mirrors (see Figure 3.1 (a)) are designed with a spherical profile on the concave side to form the cavity and an elliptical profile on the convex side to facilitate mode-matching between a collimated laser beam and the cavity modes. The mirrors are manufactured and coated by Asphericon GmbH, and made of N-SF11 glass. The selection of the mirror characteristics was based on prior work conducted by our group [39]. The concave side's radius of curvature is set at 5.5 mm to achieve the desired cavity length L in the NC regime of $L = 2R - d \sim 1.1\,\text{cm}$, to fit inside the glass cuvette. This surface is coated with a highly reflective coating with reflectivity $\mathcal{R} = (99.5 \pm 0.1)\,\%$ at 780.24 nm, corresponding to a finesse of $\mathcal{F} = 627$. On the convex side, the elliptical profile is given by

$$h(r) = \frac{r^2}{R_{as} + \sqrt{R_{as}^2 - (1+k)r^2}} \,, \tag{3.1}$$

with h representing the height of the aspheric interface at radius r from the optical axis, R_{as} the radius of curvature, and k the conic constant. Here, R_{as} and k are the mode-matching parameters and are contingent upon the refractive index of the material and the angle of incidence of the incoming light beam with respect to the aspherical surface. This surface is coated with an anti-reflective coating at

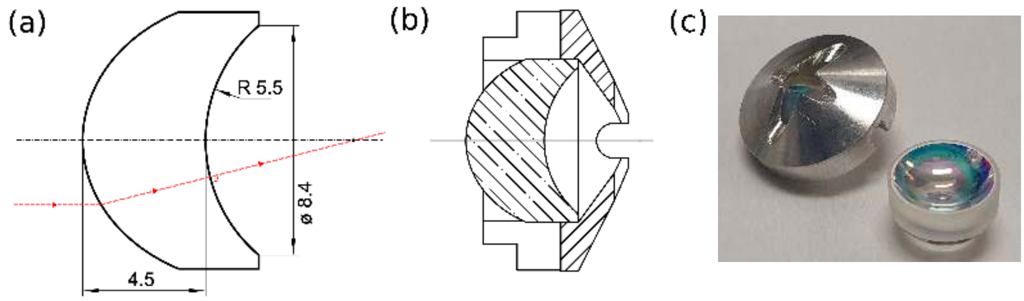

Figure 3.1: The schematic of the cavity mirror: (a) with an example of a parallel beam propagating through the mirror in red, showing the focal point of the mirror (units in mm), (b) with the mirror shield, (c) pictures of the mirrors with and without the shield.

780.24 nm, with a transmission loss less than 0.5 %. The root mean square surface deviation measures 19 nm on the aspherical side, while the clear aperture diameter remains 7.8 mm on both sides. In practice, the clear aperture diameter is 4.07 mm on the mirror side (NA = 0.37).

This configuration, consisting of these two air-glass interfaces with elliptical and spherical profiles, provides a straightforward mode-matching between a collimated input/output and a highly focused cavity mode, and is referred to as anaclastic lens-mirror. It is interesting to note that this anaclastic concept with an ellipsoidal surface first emerged in the 10$^{\text{th}}$ century in Persia [63, 64].

Additionally, the cavity mirrors are glued with an UHV compatible epoxy to a mirror support (see Figure 3.1 (b)), which also acts as a mirror shield. The purpose of the shield is to protect the mirrors during handling, and from the possible line-of-sight contamination from the atomic source. The gaps at the center of the shield provide optical access to the center of the cavity where the atoms are trapped.

From the properties of the cavity mirrors, we can deduce the cavity's ability to reach the strong coupling regime by evaluating crucial parameters: the coupling strength g (see Equation 2.4) and the cavity decay rate κ (see Equation 2.14). It's important to highlight that g solely depends on the cavity's geometry for a fixed dipole transition. Assuming $d \ll R$ as we operate really close to the concentric point, from Equations 2.4 and 2.29, we can approximate the coupling strength

$$g \approx \frac{\mu_{ge}}{\lambda}\sqrt{\frac{2\pi c}{\hbar\epsilon_0}}\left(\frac{2}{R^3 d}\right)^{1/4}, \tag{3.2}$$

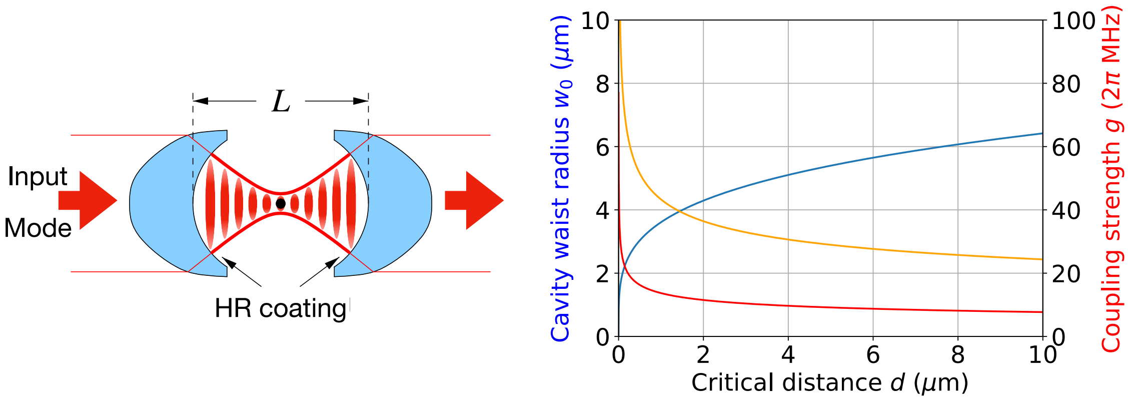

Figure 3.2: **Left:** The schematic of the NC cavity system. **Right:** The cavity waist radius w_0 (blue) and the atom–cavity coupling strength g for single atom (red) and for 10 atoms trapped (orange), as a function of the critical distance d.

where the dipole moment $\mu_{ge} = 2.99\, ea_0$ for the D_2 line of ^{87}Rb, with e being the electron charge and a_0 the Bohr's radius. The performance of the cavity is intricately linked to the critical distance, shaping the cavity length in accordance with its value. The evolution of both the cavity beam waist w_0 and the single atom–cavity coupling strength g, along with the 10 atom–cavity coupling strength $g_{N=10}$ where $g_N = \sqrt{N} g$ [51, 52], are shown in Figure 3.2. Emphasising our operational focus on the last stable resonance before the concentric regime, theoretical parameters (see Table 3.1) are computed with consideration given to the corresponding value of d. In the experimental context, viable values of d are discretised based on the cavity free-spectral-range (FSR) ν_{FSR}, ensuring stable resonances align with multiples of half-wavelength $\lambda/2$. Here, $\lambda/2$ acts as the upper bound for d, the exact value

Mirror reflectivity $\mathcal{R}$	99.5 %	Mirror radius R	5.5 mm
Finesse $\mathcal{F}$	627	Critical distance d	0.39 µm
Cavity waist w_0	2.8 µm	FSR ν_{FSR}	13.6 GHz
Cavity decay rate κ	$2\pi \times 10.9$ MHz	Atomic decay rate γ	$2\pi \times 3.03$ MHz
Coupling strength g	$2\pi \times 17.3$ MHz	Cooperativity C	4.5

Table 3.1: The cavity parameters, evaluated at the last stable point before concentricity, corresponding to a critical distance $d = 0.39$ µm, with a single atom trapped. The parameters corresponds to the ideal case, providing an upper bound for the performance of the system.

depending on the effective mirror radii R such that $d_{min} = 2R \bmod (\lambda/2)$. Under this assumption, the computed parameters with $d = \lambda/2$ provide an estimate for the cavity setup operated at the final stable resonance within the range $0 < d < \lambda/2$.

In our current system, operating at the final stable resonance through a cycling transition, the expected single atom cooperativity stands at approximately $C = 4.5$. This estimation is derived from $g = 2\pi \times 17.3\,\mathrm{MHz}$, $\kappa = 2\pi \times 10.9\,\mathrm{MHz}$, and $\gamma = 2\pi \times 3.03\,\mathrm{MHz}$ for the D_2 line of $^{87}\mathrm{Rb}$ [65]. It's crucial to note that the criteria for the strong coupling regime (see Section 2.1.3) are met: $g/\kappa = 1.6 \gg 1$ and $g/\gamma = 5.7 \gg 1$. Though the former ratio is above the desired threshold by a small margin, a simple improvement lies in enhancing the cavity finesse $\mathcal{F}$, at the cost of stricter stability requirements (see Section 3.1.2). The more significant ratio here is $g/\gamma > 1$, as its increase depends solely on an increase in g, only achievable through adjustments such as using smaller mirror radii R or shorter critical distances d for NC cavities. In addition, our achievable cooperativity of $C = 4.5$ is comparable to the cooperativity achieved in other cold atom cavity experiments using micro-cavities [32].

3.1.2 Noise limit factor

To effectively quantify the impact on the cavity performance due to the shift in cavity resonance, we introduce a noise limit factor ξ_{noise} which assesses the frequency fluctuation $\delta\omega_c$ due to mechanical noise, in the unit of the cavity linewidth $\delta\nu = \kappa/\pi$ (see Figure 3.3). This factor can be translated to the variation of cavity length δL through the following expression

$$\xi_{noise} = \frac{\delta\omega_c}{2\kappa} = \frac{\delta L}{\lambda/2}\,\mathcal{F}\ . \tag{3.3}$$

A noise limit factor $\xi_{noise} = 1$ indicates that the cavity resonance fluctuation is equal to its linewidth. Intuitively, as we look at the reflection or transmission of the NC cavity, both transverse and longitudinal misalignments will be reflected on the transmission spectrum of the cavity. As the cavity approaches the concentric regime, transverse noise increasingly dominates the transmission profile, shifting the cavity resonance. Consequently, this dominance is evident in the standard deviation of the cavity length δL as the cavity axis shifts following the misalignment direction.

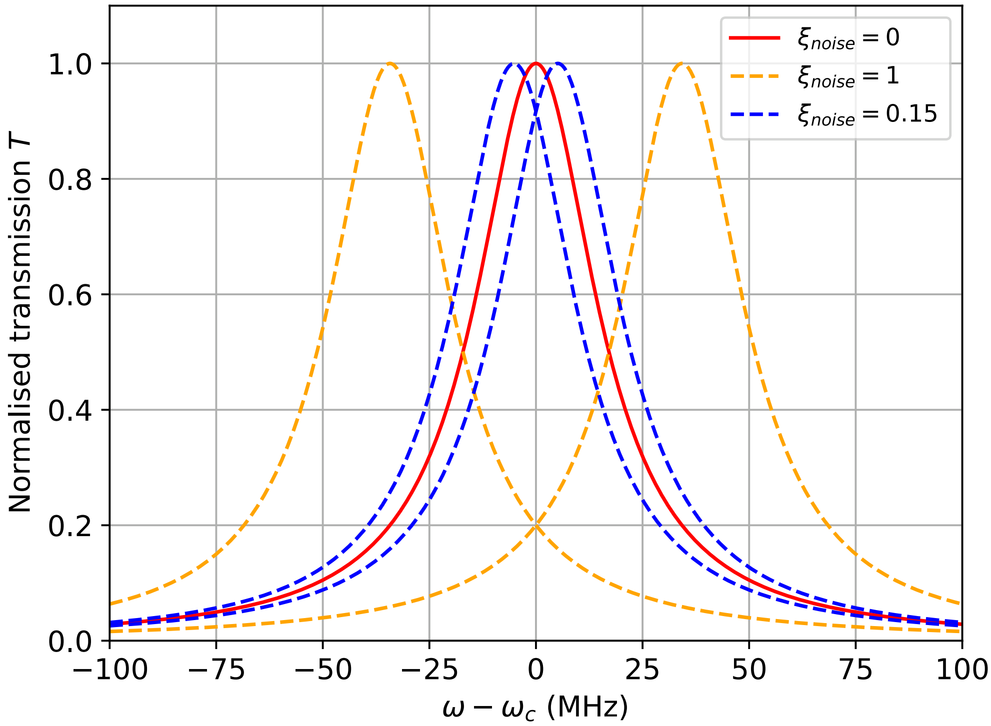

Figure 3.3: The correspondence between the noise limit factor ξ_{noise} and the shift in cavity resonance. Red: cavity transmission centered at ω_c. Orange: shifts for $\xi_{noise} = 1$. Blue: shifts for $\xi_{noise} = 0.15$.

Our objective is to maximise the interaction of our atom–cavity system. To achieve this, the cavity resonance, and thus the cavity length, must remain stable relative to the atomic linewidth being probed. For our system, this means the maximum fluctuation in cavity resonance, $\delta\omega_c$, should be equal to the atomic decay rate γ, with respect to the cavity linewidth. This requirement sets a noise limit factor of $\xi_{noise} \sim 0.15$, indicating that mechanical noise along the cavity axis contributes to the cavity linewidth by no more than 15%, as illustrated in Figure 3.1.2. Considering our nominal cavity finesse of $\mathcal{F} = 627$, this equates to a cavity length fluctuation of approximately $\delta L_{rms} \sim 0.9\,\text{Å}$. Note that a higher finesse would necessitate smaller fluctuations in cavity length to maintain the desired noise limit factor.

Revision	1a	1b	2a	2b	3
Actuator type	Piezoelectric stacks		Flexure stage		Piezoelectric stacks
Relative movement	Translation				Tip-tilt
Movement range	10 µm		50 µm × 50 µm × 24 µm		15 µm
Mounting of actuators	Epoxy		Screws		Tension
Post-baking misalignment (max)	> 5 µm		~ 5 µm		
UHV operation	Yes	No	Yes		
Operating finesses	138(2)	606(3)	275(9)	484(9)	323(8)
Mechanical noise (passive)	~ 2 Å		~ 10 Å	1.7(2) Å	0.36(2) Å
Mechanical noise (w/ a.n.c.)	-		~ 4 Å	1.6(2) Å	-
Noise limit factor	~ 0.07	~ 0.3		~ 0.2	~ 0.03
Experiment with atoms	Yes	No			Yes
Publication	[66]	[67]	[68]	-	[60]

Table 3.2: A summary of structure iterations. a.n.c.: active noise cancellation. The measurement of the mechanical noise is done with an integration time of 0.5 s (see Section 4.3.3).

3.2 Past configurations

To maintain the mirrors in position and create the cavity, a supporting structure is essential. This framework must fit within our glass cuvette, possess ample movement range for convenient misalignment adjustments, and exhibit minimal susceptibility to external noise. In meeting these criteria, various mechanical structures were previously examined, and an overview of their attributes is available in Table 3.2. The primary distinctions among the three cavity structures revolve around the actuators employed and the relative motions between the mirrors. This includes either translating one mirror mount with respect to a fixed mirror or employing tip-tilt adjustments across the overall structure.

In the initial iteration, previous group members [67] employed piezoelectric stack

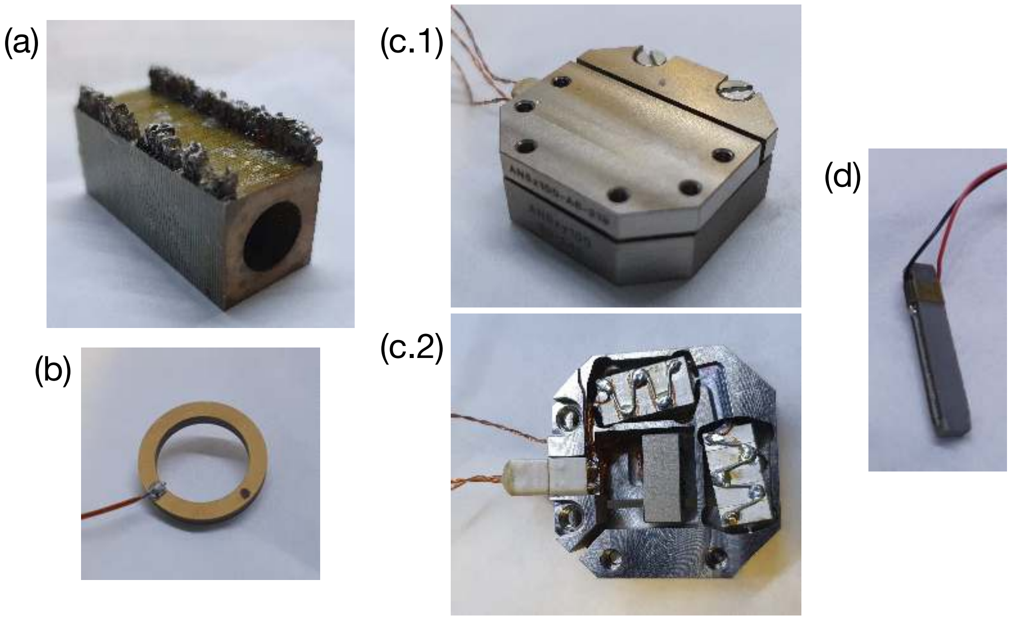

Figure 3.4: The actuators used in the different revisions: (a) revision 1 piezoelectric stack, (b) ring actuator, (c.1) revision 2 flexure actuator, (c.2) flexure mechanism, (d) revision 3 piezoelectric stack.

actuators (Physik Instrumente P-153.10H) comprising of 72 shear-piezoelectric layers glued together. Measuring 16 mm × 16 mm × 40 mm with a central cylindrical hole of 10 mm diameter for optical access (see Figure 3.4 (a) and Figure 3.5), these actuators provided a movement range of 10 µm in each direction. However, this range proved insufficient to compensate for misalignments occurring during the baking cycle required to reach UHV.

In the second iteration [59], a flexure-based translation stage (Attocube AN-Sxyz100) was utilised, exploiting a flexible joint to achieve a more extensive expansion of the piezoelectric movement (see Figure 3.4 (c.1) and (c.2) and Figure 3.6) [69]. Sized at 24 mm × 24 mm × 10 mm, this stage offers three-dimensional translation movement up to 50 µm × 50 µm × 24 µm.

Alongside the piezoelectric stacks and flexure stage, an additional ring-shaped actuator (Boston Piezo-Optics PZT-4 compressional crystal, see in Figure 3.4 (b)) was introduced to facilitate fast movement along the cavity axis with enhanced precision. The actuator, measuring 2 mm in thickness, provided a maximum travel range of 0.27 nm. It was glued to one of the cavity mirror mounts, and a spacer was employed to shield the high-voltage electrode.

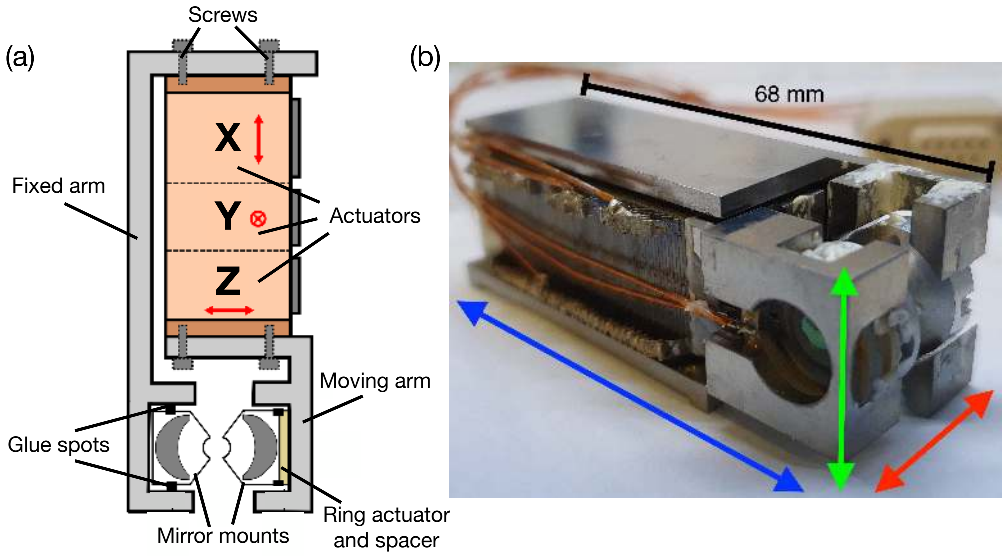

Figure 3.5: The revision 1, composed of one fixed arm and one movable arm attached to 3 piezoelectric stack actuators mounted together. (a) CAD drawing, (b) Assembled NC cavity.

However, the primary drawback of the second revision (see Figure 3.6) lies in the mechanical noise of the structure. In comparison to the first revision, which utilised actuator stacks, the susceptibility to external mechanical noise of the second revision is noticeably higher. We attribute this increase in noise to the intricate flexure mechanism, which, by creating a system of "stacked cantilevers", amplifies

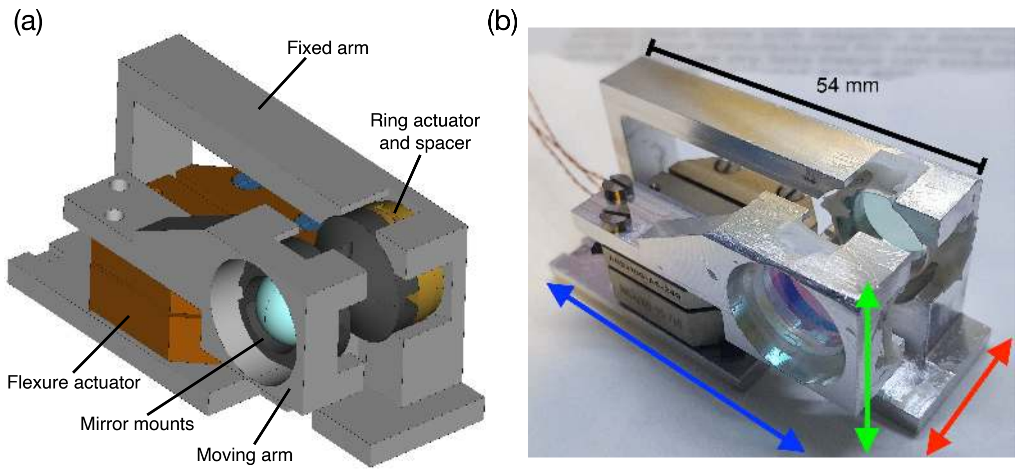

Figure 3.6: The revision 2a, composed of one fixed arm and one movable arm screwed down on the Attocube stage. (a) CAD drawing, (b) Assembled NC cavity.

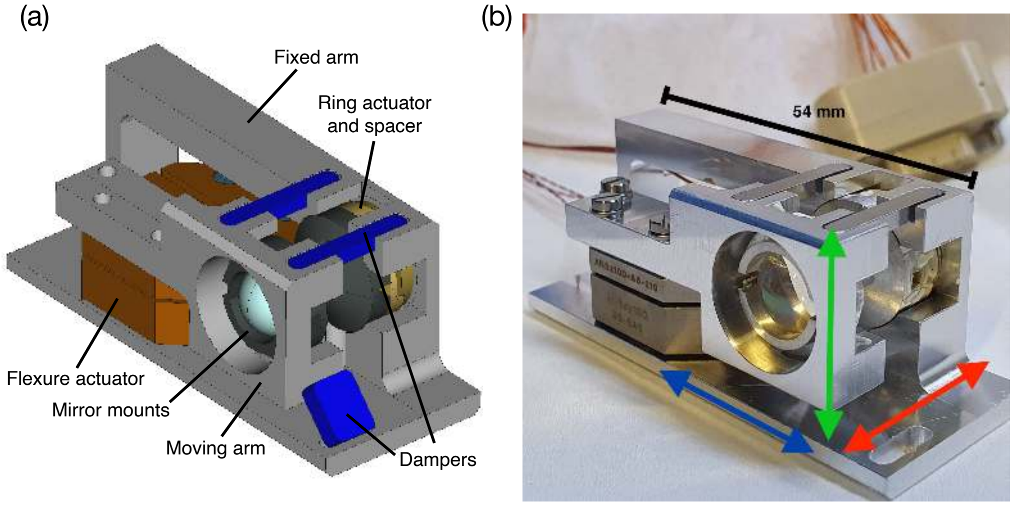

Figure 3.7: The revision 2b, composed of one fixed arm and one movable arm screwed down on the Attocube stage. Dampers are added to the structure, with two on the top and one on the side to restrict the canti-lever behavior of the movable arm. (a) CAD drawing, (b) Assembled NC cavity.

the mechanical noise within the structure. To address this issue and mitigate the noise, we introduce friction dampers to the cavity structure. These dampers, securely positioned in slots to prevent accidental dislodging, rely on friction generated by their weight alone to stay in place (see Figure 3.7). With this implementation, we successfully reduced the passive mechanical noise of the second revision by a factor of 5. Despite this noise reduction, the noise limit factor for the structure, $\xi_{noise} \sim 0.2$, still exceeds our target for atom-cavity experiments (see Section 3.1.2). In addition, the dampers couple the translation movement of the movable arm to the fixed arm through the top dampers connection, complicating the cavity alignment process, as the movement is no longer decoupled along the three Cartesian axes.

3.3 Revision 3 conception

To reduce the susceptibility to external mechanical noise, the new revision tackles two aspects of the previous revisions: the bulkiness of the structure and the use of a simpler actuator structure. The bulky design, featuring a protruding moving arm supported solely at one end, displays a cantilever structure. This design, combined with a flexure stage, is highly susceptible to external noise. While not being optimal,

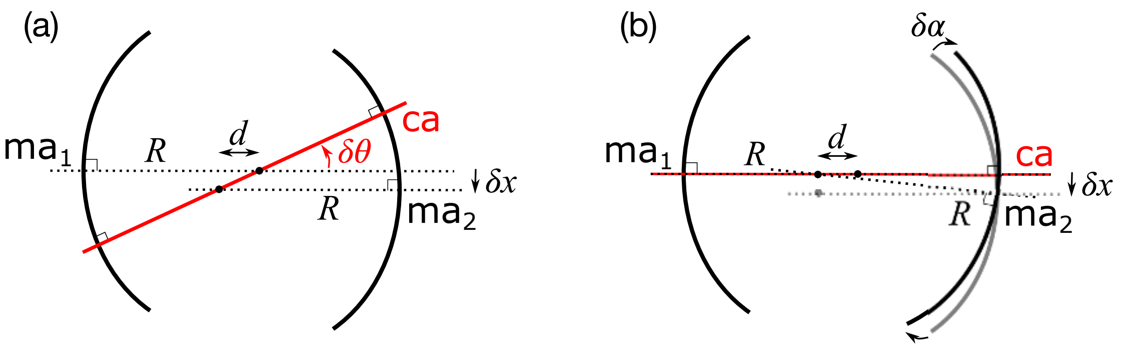

Figure 3.8: The equivalence of transverse and tip-tilt displacements in the NC regime. (a): Rotation of cavity axis (ca) due to transverse misalignment. In a NC cavity of critical distance d, a small transverse misalignment δx of the second mirror rotates the cavity axis by an angle $\delta\theta$. (b): Equivalence of transverse and angular misalignment. A small transverse misalignment δx can be corrected by rotating the mirror by a small angle $\delta\alpha$. ma: mirror axis.

the previous design choices were constrained by the available space in the vacuum system and the required movement ranges to correct for misalignment. With the availability of new piezoelectric stacks (PI PICMA P-882.51), displaying a larger movement range for a smaller size, we use the tip-tilt equivalence to translation in the NC regime (see Figure 3.8) to create a cage-like tensegrity structure [70]. The latter allows the adjustment of the necessary three degrees of freedom for cavity alignment, while maintaining a compact structure with a lot of optical access (see Figure 3.9).

The mirrors in their mounts are fixed to aluminium frames, separated by the piezoelectric actuators acting as the compression members of the structure, and helical springs (MISUMI AUT3-20) on the external sides of the cavity stage acting as the tension members and holding the whole structure together (see Figure 3.9). In addition, the structure is glued with epoxy (MasterBond EP21TCHT-1) on a stainless steel plate to avoid applying pressure onto the structure when handling it during installation in the vacuum chamber. Note that only one mirror frame is glued and resting onto the plate, to not constrain the tip-tilt movement of the structure. To minimise any deformation during the baking of the vacuum system to reach UHV, each manufactured frame and plate is stress relieved via heating and cleaned

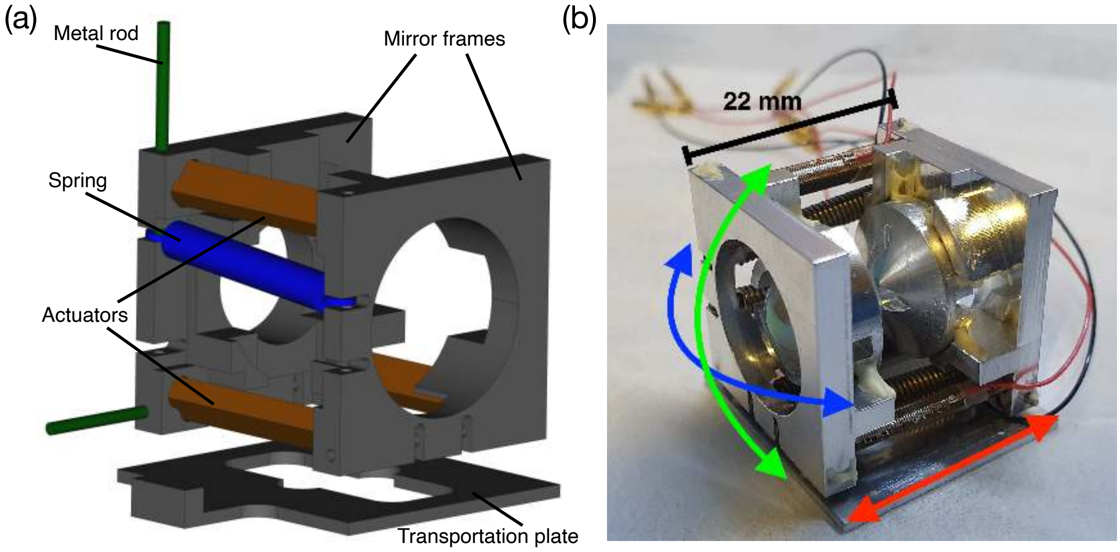

Figure 3.9: The revision 3, composed of two mirror frames linked together into a tensegrity structure through the piezoelectric actuators (compression members) and springs (tension members), and on a plate for handling. The metal rods serve as the contact points for the spring hooks. (a) CAD drawing, (b) Assembled NC cavity.

through an ultrasonic bath. The epoxy is also subjected to outgassing within a low vacuum chamber at 10^{-5} Torr before application due to air bubbles forming within the epoxy during the mixing of the resin and the hardener (see Figure 3.10). This step is taken to minimise any potential displacement caused by epoxy expansion or shrinkage during the subsequent baking phase required to achieve UHV conditions.

The piezoelectric actuators have a movement range of 15 μm, under an operating voltage of 0 – 100 V. They exhibit a good compromise between their size and their tunability to compensate for misalignment. As the expansion of a single piezoelectric actuator changes the cavity alignment in all three degrees of freedom, we introduce a decoupling operation to independently control the cavity length L, tip movement T_{tip}, and tilt movement T_{tilt} with respect to each actuator voltages

$$\begin{pmatrix} V_A \\ V_B \\ V_C \end{pmatrix} = G \begin{pmatrix} 1 & 1 & 1 \\ 1 & -1 & 1 \\ 1 & 1 & -1 \end{pmatrix} \begin{pmatrix} L \\ T_{tip} \\ T_{tilt} \end{pmatrix} , \tag{3.4}$$

where G is a constant representing the gain due to the high-voltage amplifier.

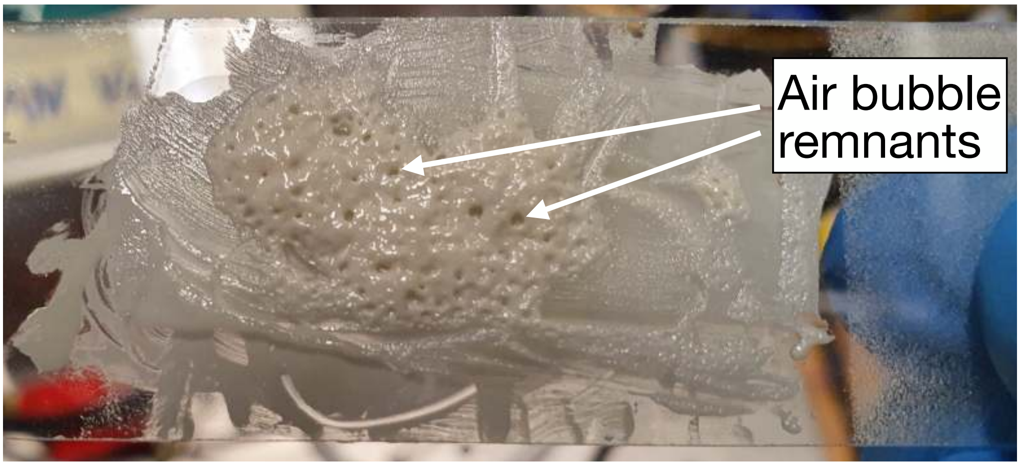

Figure 3.10: The holes in the epoxy mix after an outgassing cycle at 10^{-5} Torr. The air bubbles form during the stirring between the resin and the hardener components of the epoxy, and leave holes in the mix after being outgassed.

3.3.1 Cavity assembly

To assemble the NC cavity, an accurate method for positioning the mirrors is required. To achieve this, a reference axis is established by coupling light between two fiber couplers using four mirrors (see Figure 3.11). The cavity system, with the first mirror glued on using a low-outgassing epoxy (MasterBond EP21TCHT-1), is then fixed onto the right tip-tilt stage (Thorlabs KM200PM) attached to a 3-axis manual translation stage (Thorlabs PT3). The combination of the two stages allows the cavity mirror to be freely adjusted along the reference axis. The second mirror is held with a home-made tweezer. The tweezer is also fixed onto the same type of tip-tilt stage as the first mirror, along with a 3-axis piezoelectric translation stage with 100 µm moving range (Piezosystem Jena Tritor 101 CAP) for fine adjustment.

By maximising the coupling of the retro-reflected light from both cavity mirror convex surfaces back into the fibre couplers, each axis of the cavity mirror is aligned along the reference axis (see Figure 3.11). The second mirror is then slowly translated towards the first mirror to form a cavity mode. The cavity mode and the transmission spectrum of the cavity are observed with a CCD camera (Point Grey CM3-U3-13S2M-CS) and an amplified photodiode (Thorlabs PDA36A2). Any transverse misalignment is corrected using the 3-axis piezoelectric translation stage.

The critical distance d can be estimated from the frequency spacing of the

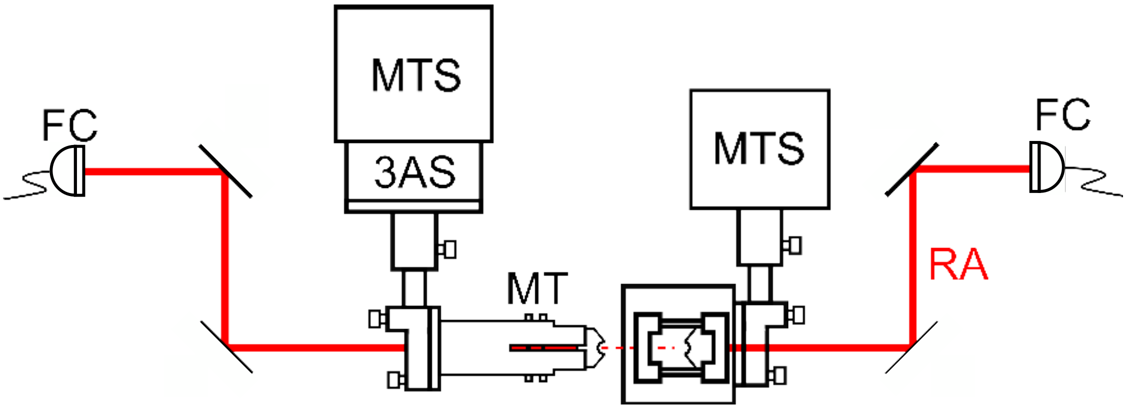

Figure 3.11: The alignment setup of the NC cavity. RA: reference axis, FC: fibre coupler, MT: mechanical tweezer, MTS: manual translation stage, 3AS: 3-axis actuator stage.

cavity transverse modes (see Section 4.2.1). The target critical distance is around $d \sim 7.8\,\mu\mathrm{m}$. This value is chosen as it is around half of the travel distance of the cavity's piezoelectric actuators, which will allow greater tip-tilt tuning as the cavity approaches concentricity.

Once the target critical distance is reached, mirrors are fixed to the frame with a small amount of epoxy, such that additional misalignment during the curing process is minimised. During the initial curing of the epoxy (2 hours), any misalignment is corrected using the 3-axis piezoelectric translation stage. When the epoxy is fully cured after 70 hours, the tweezer is released and removed. The assembled NC cavity is then carefully transferred from the alignment setup to the main vacuum chamber. Note that, due to space constraints within our vacuum chamber, no additional stabilisation stage can be added to the current system. However, this is not an issue as the passive stability of our system already meets the requirements established in Section 3.1.2 (see Section 4.3.3).

3.3.2 Stabilisation of innate transverse susceptibility to displacement

Using small movement range actuators limits the capability of the system to correct for transverse misalignment. However, large transverse displacements can occur in the cavity structure during several parts of the assembly process, such as the

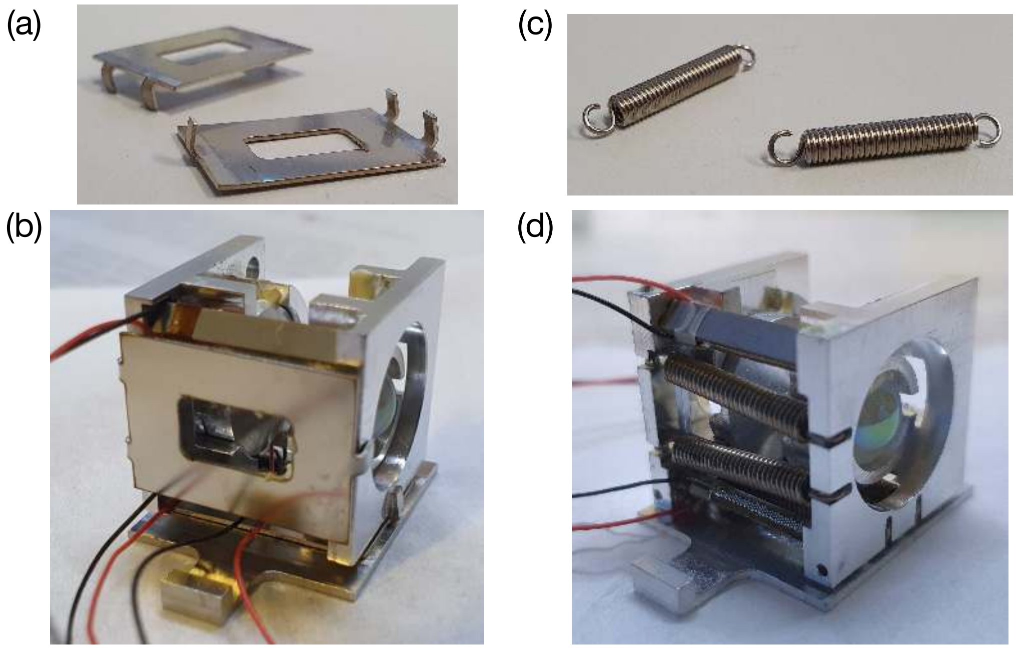

Figure 3.12: The mounted cavities with cavity mirrors, using the 3 point contact clamp (a and b), and the springs used in the final structure shown in Figure 3.9 (c and d).

epoxy curing and the baking of the vacuum chamber to reach UHV. To maximise the capability of the system to compensate for transverse misalignment, the sensitivity of the tensegrity cavity structure is minimised by adjusting its tension force. This force holds the entire structure together, and a well-defined and stronger tension force will better resist transverse displacement. It is then important to characterise and evaluate the performance of different tension members.

To implement the tension in the structure, two alternatives are tested. The first one uses a laser-cut metal sheet bent to a clip to act as a clamp on the cage. The design of the clamp is such that only 3 points are in contact with the structure, to make sure that the tension force is defined on the structure (see Figure 3.12). The hole in the middle of the clamp is to allow optical access for the MOT beams. Different clamp parameters are tested such as:

- the thickness of the sheet: ranging from 0.1 mm to 0.6 mm.
- the metal: stainless steel, bronze, and brass.
- the bending angle of the clamp: ranging from 90° to 120°.

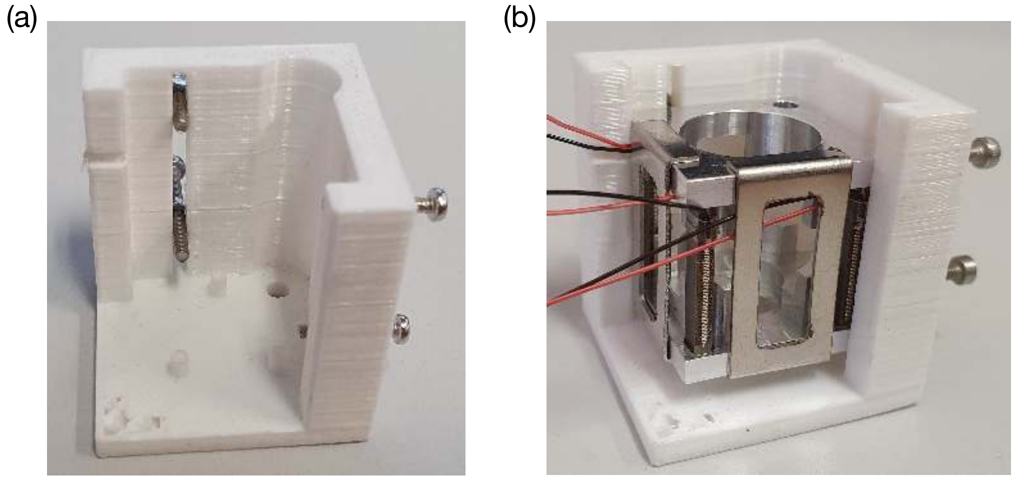

Figure 3.13: The 3D printed mounting stage to assemble the clamp cavity. The mirror frames are held in place using screws with nuts glued on the side.

- the number of contact points: 2, 3 and 4.

Additionally, each clamp is stress relieved after bending via heating in an oven to the corresponding temperature for each metal, and then cleaned with an ultrasonic bath. The clamps are then mounted on the cavity frames, with the actuators as pillars, using an external 3D printed stage (see Figure 3.13) to facilitate the assembly, by maintaining the frames and the actuators in place with respect to each other.

The second alternative used helical springs, where the contact points are defined by the hooks of the springs. The springs are hooked to the frames via a stainless steel rod (see Figure 3.9). To mount the spring cavity, the springs are first installed with the rods onto the mirror frames. Then one mirror frame is held in place using a vise, and the other one is clamped down on a 1D translation stage (Thorlabs MT1) to slot the actuators between the frames when the springs are elongated. The spring cavity is employed in the final system.

To evaluate the transverse displacement in the different directions with regards to individual excitation of each actuator, one mirror frame is fixed in place with a clamp, and the displacement of the second mirror frame is measured with a microscope (with a $\times 10$ magnifying objective imaged onto a fix CCD camera (Point Grey CM3-U3-13S2M-CS)). We then proceed to individually vary the length of each actuator across its entire moving range and monitor the shift of a reference

Structure configuration	Maximum transverse displacement observed
Clamp (Figure 3.12 (a),(b))	3.75 µm
Spring (Figure 3.12 (c),(d))	1.25 µm
Parallel base (Figure 3.14 (a))	7 µm
45° base (Figure 3.14 (b))	3.75 µm

Table 3.3: The transverse displacement for several structure configurations. The structure using the springs and the 45° base is exhibiting less susceptibility to transverse forces overall. The structure with the clamps also shows reduced susceptibility with a 45° base compared to a parallel one.

point of the movable mirror frame, usually the edge of the frame, on camera. The displacement in any direction is evaluated in pixels, where each pixel corresponds to a distance of 0.25 µm with the given objective. The evaluation is carried out for all three actuators, and the maximum transverse displacement from the cavity axis is recorded. The maximum displacement of each configuration is listed in Table 3.3. From the various combinations of tuning parameters assessed for the clamp, only the outcomes obtained with the best performing clamp configuration are shown, which corresponds to a 0.4 mm thick stainless steel clamp with 3 contact points and a bending of 100° (see Figure 3.12) (a) and (b)). The superiority of the helical springs over the clamps can be explained from a structural perspective. The clamps contact points, after laser cutting, are bent by hand at a specific angle with an accuracy of 1° and can be modified during the stress relieving step. As such, the tension between the different contact points is not as well-defined as for the helical springs, which exhibit a spring constant tolerance of ±10 %.

Additionally, as the actuator's base is rectangular (2 mm × 3 mm), an anisotropic bending behavior is observed, with greater deformation along one axis. Rotating the placement of the actuator's base on the frame (see Figure 3.14) has significant impact in reducing transverse displacement as shown in Table 3.3. Actuators with square bases have also been tested, but the size constraint on the mirror frames made them less suitable than the rectangular base actuators.

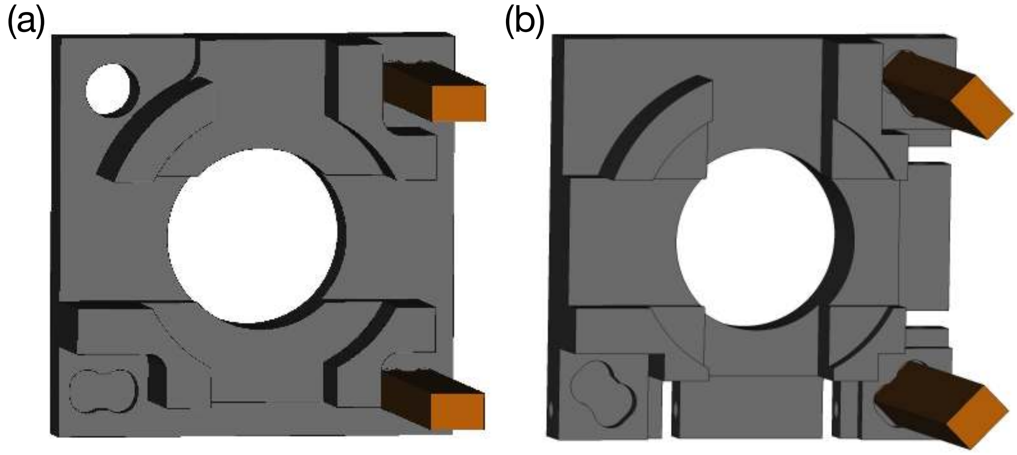

Figure 3.14: The different actuator base positions impacting the stability of the NC structure. (a) Actuator base parallel to the mirror frame. (b) Actuator base rotated by 45° from the mirror frame, exhibiting less anisotropic bending behavior. The dog-bone structure at the base of the actuators is to facilitate the mounting of the cavity and is not in contact with the actuators.

3.3.3 Preventing contamination of particles on cavity mirrors

During the operation of previous cavity systems with atoms inside the vacuum, we observed an increase in the cavity linewidth over time. This rise, determined using the revision 2b stage, was linked to the release of particles — specifically, Rb atoms or debris — onto the cavity mirrors during dispenser operation. We noted that a higher driving current exceeding 3 A, compared to our nominal 2.4 A for the magneto-optical trap (MOT), accelerated damage to the mirror coating (see Figure 3.15). This accelerated damage can be correlated with the dispenser temperature exceeding 400 °C for a current above 3 A, causing excitation of any particles on the dispenser.

The primary candidate responsible for this linewidth increase, and consequently a reduction in the cavity system's performance due to the correlation between linewidth and cavity losses, is Rb atoms. These atoms exhibit the highest particle density in the vacuum chamber during operation, as expected. Depending on Rb atoms' adhesion to surfaces, i.e., if it sticks to a surface on the first collision or not, they might bounce off the walls or mirror shields and end up directed toward the clear aperture of the mirrors. Research by Klempt et al. [71] has shown that UV

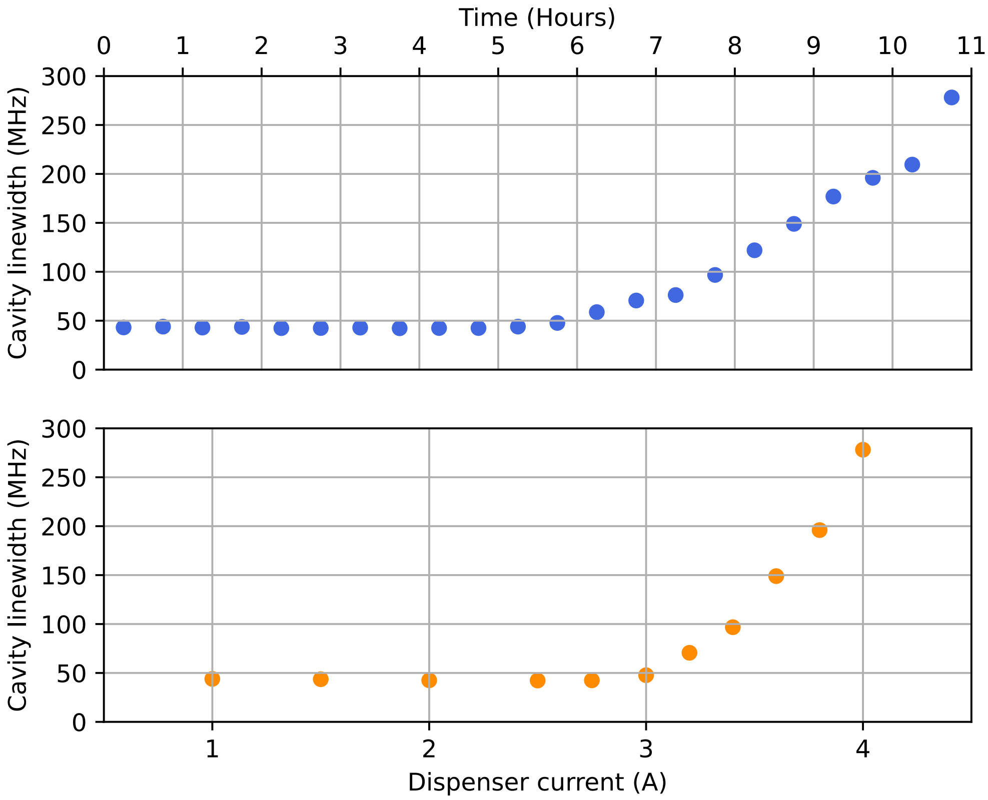

Figure 3.15: The NC cavity linewidth with respect to time (top) and dispenser current (bottom). The dispenser current is started at 1 A for one hour and subsequently increased every hour, by 0.5 A until 2.5 A and by 0.2 A from 2.5 A to 4 A. We observe a noticeable increase in the linewidth past a current of 3 A at the 6 hour mark.

light can be used to excite Rb atoms glued to surfaces, causing them to move away from mirrors depending on the shining angle. However, in our case, shining UV light on the mirrors after observing a linewidth increase did not impact the cavity linewidth. This suggests that the particles coating the mirror surfaces are not Rb atoms or, at least, are not sensitive to UV light excitation. One additional plausible explanation could be that the line of sight for UV light to the mirrors is blocked or challenging to access due to the mirror shields.

To investigate the nature of the released particles further, i.e., Rb or debris, we built a movable blocker using a linear feedthrough (MDC Precision High Temperature Linear Feedthrough 660039, see Figure 3.16) to obstruct any direct line of sight between the atom dispenser and the cavity by blocking a section of the vacuum tube. We then proceeded to place a cavity in vacuum and monitored its linewidth

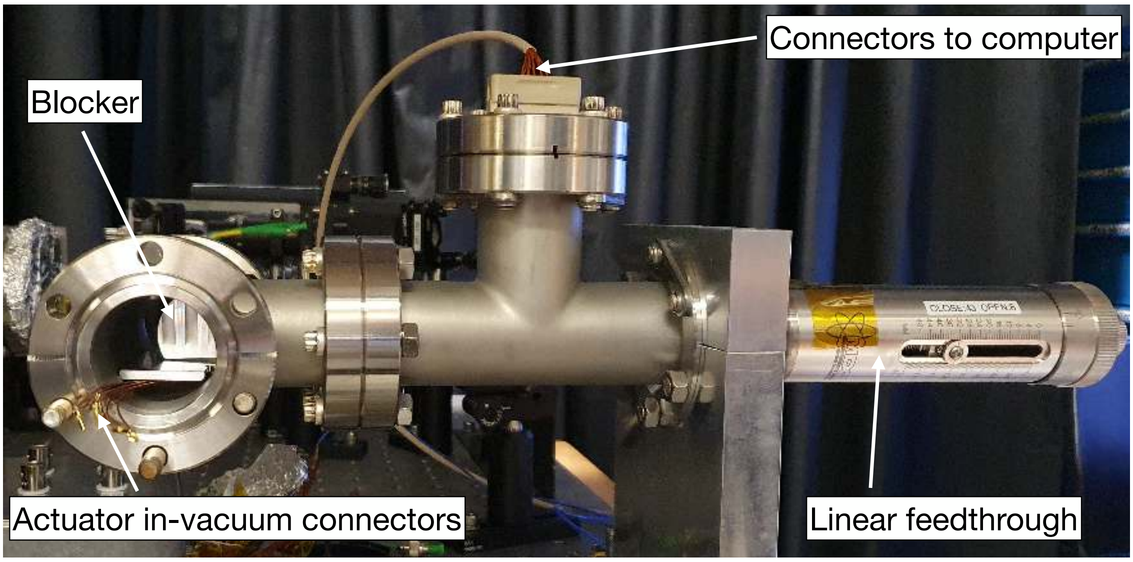

Figure 3.16: The blocker and the linear feedthrough. The blocker is machined out of aluminium to fit the inside of the vacuum chamber and obstruct the dispenser line of sight as much as possible. It is attached to the linear feedthrough via screws. When fully extended, the blocker obstructs 80% of the vacuum tube cross-section, as shown in the picture. A small gap below is kept for the actuators wires to connect to the computer outside vacuum.

with respect to the dispenser's current via the transmission spectrum of the cavity. The experiment was conducted with near-planar mirrors without shields to facilitate cavity formation, due to a lack of stability of the NC cavity stage, rendering the revision 3 stage not usable at the time. The results showed that the initial debris accumulated on the dispenser while preparing the vacuum system were responsible for the cavity linewidth increase, as using the designed blocker to block the line of sight prevented the deposition of debris onto the cavity mirrors, protecting the cavity linewidth (see Figure 3.17). Moreover, driving the dispenser at a high current and releasing a large quantity of Rb atoms into the vacuum chamber after clearing the debris did not impact the mirror coating, with or without the blocker.

Furthermore, since previous experiments were conducted with near-planar mirrors featuring coatings distinct from those on our NC mirrors, it is plausible that diverse adhesive interactions with Rubidium atoms occurred based on the coating. Subsequent tests with the revision 3 cavity stage and NC mirrors, at a later time, yielded similar results to those for the near-planar cavity (see Figure 3.17), concluding

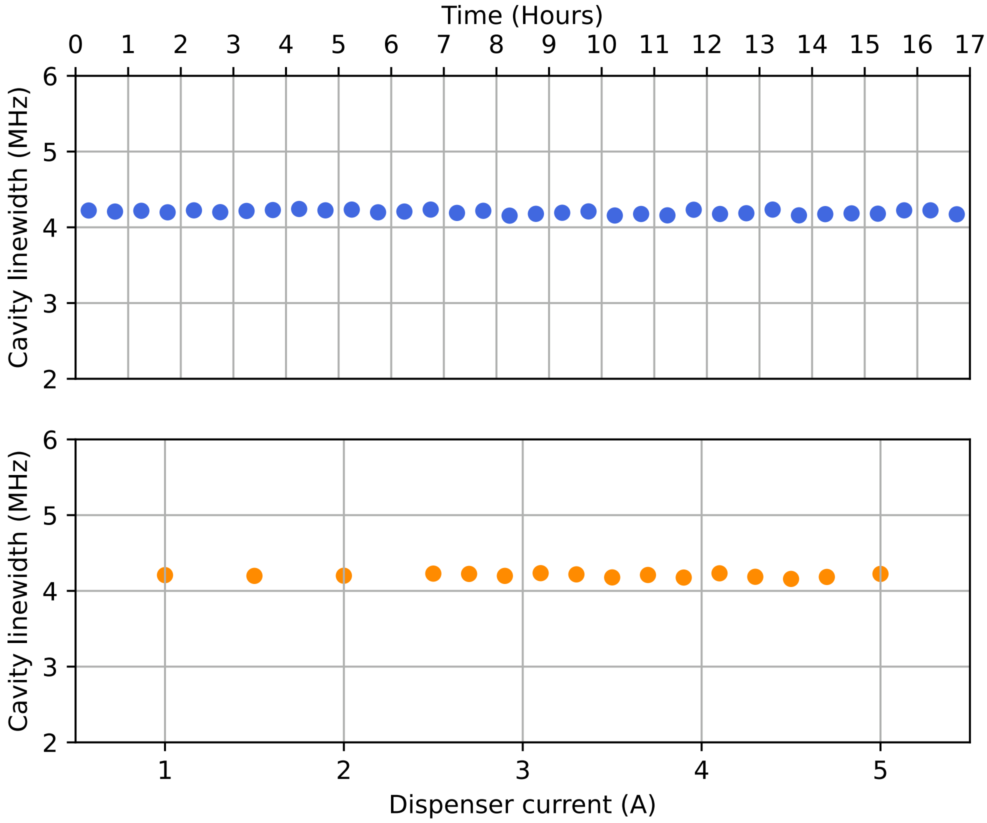

Figure 3.17: The near-planar cavity linewidth with respect to time. The dispenser current is started at 1 A for one hour and subsequently increased every hour, by 0.5 A until 2.5 A and by 0.2 A from 2.5 A to 5 A. The blocker is engaged for the first 16 hours and then removed. As observed, the linewidth did not increase with the blocker in position. Filling up the vacuum chamber with Rb atoms without the blocker did not impact the linewidth either.

that running the dispenser above 3 A did not impact the cavity linewidth.

Chapter 4

Instruments and measurement methods

This chapter provides an overview of the core experimental instruments and methodologies employed with our NC cavity system. It covers various aspects, including the standard laser systems employed, their locking mechanism utilising atomic spectroscopies, as well as the vacuum system used for atom trapping and the measurement methods for cavity parameters. Special attention is paid to the stabilisation protocols implemented, along with the characterisation of the stability performance of our NC cavity to ensure it aligns with the pre-established requirements. This characterisation has also been published in the Review of Scientific Instruments [60].

4.1 Core instruments

The cornerstone of our cavity setup lies in the laser system, serving as cooling and trapping tools for atoms, as pump and alignment beams, and as frequency references for generated photons. Therefore, it is crucial for them to operate with narrow linewidths compared to atomic transition linewidths. We utilise a custom-built external cavity diode laser (ECDL) known for its extensive frequency tunability over a wide frequency range and a relatively narrow linewidth. Employing spectroscopic techniques to probe atomic transitions allows us to stabilise the ECDL frequency. Another crucial tool is the vacuum system employed to trap atoms, as the trapping techniques utilised in this thesis demand an UHV of around 10^{-9} Torr for effective implementation.

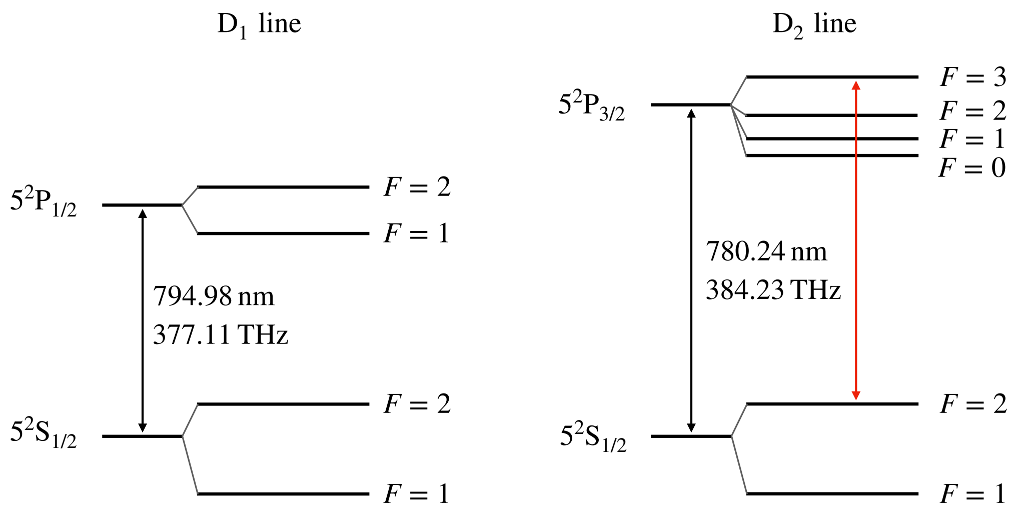

Figure 4.1: The energy diagram of ^{87}Rb [65], an alkali metal with hydrogen-like characteristics. The most relevant transition is the cycling transition from the state $|F = 2, m = \pm 2\rangle$ to the state $|F' = 3, m' = \pm 3\rangle$, as this is the transition to which our NC cavity is tuned for resonance.

4.1.1 External cavity diode laser

In our cavity experiment, we rely on three key wavelengths produced by enclosed temperature-stabilised semiconductor laser diodes: 780 nm (Sharp GH0781RA2C) and 795 nm (Thorlabs LD808-SA100) lasers which target the D_2 and D_1 transitions of ^{87}Rb respectively (see Figure 4.1), for cavity probing and establishing the MOT. Additionally, we employ an 810 nm (Thorlabs LD808-SA100) laser to provide far-off resonant light to the near-concentric cavity for single atom trapping (see Section 5.1.2). Aspheric lenses (Thorlabs C220TMD-B) collimate the laser diodes' output modes, directing them towards a diffraction grating (Thorlabs GH13-18V) to form the ECDLs, assembled in a Littrow configuration [72]. From the diffraction of the incoming light onto the grating, the portion of the light in the zeroth order is propagating towards the output of the ECDL, while the smaller amount of light diffracted in the first order is back-reflected to the laser diode, forming the external cavity (see Figure 4.2). By rotating the diffraction grating, the diffraction angle will vary which, in turn, tunes the resonant wavelength of the ECDL as well as its linewidth. Typically, with an external cavity length of around 3 cm and a diffraction efficiency of approximately 20 %, our ECDLs exhibit a linewidth of less than 1 MHz,

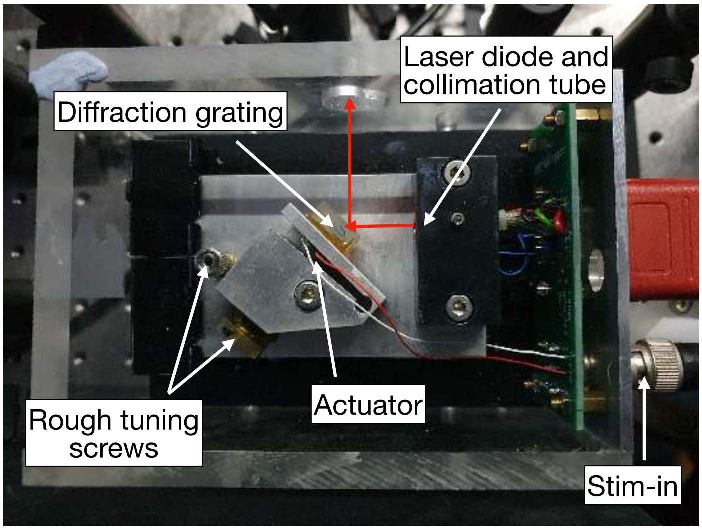

Figure 4.2: A picture of an ECDL (left) inside an acrylic box for temperature control. The laser path is drawn in red. The grating is set up to redirect the light from the diode's first-order diffraction back into the diode, creating the cavity. Size of the semiconductor laser diode (right), ruler in cm.

considerably narrower than the atomic or cavity linewidth.

Following this, the ECDL output enters an optical isolator (see Figure 4.3), utilising a Thorlabs IOT-5-780-VLP for the 780 nm and 795 nm lasers and two Thorlabs IO-3D-830-VLP for the 810 nm laser. This precaution is implemented to avoid any light to back-propagate and potentially affect the ECDL's operation or damage the diode. Subsequently, the laser beam is directed into a single-mode fiber (AFW Technologies FOP-78-x) to isolate the ECDL component from the atomic spectroscopy setup for adjustement purposes. Additionally, since only a Gaussian mode profile is supported within the fiber, this coupling process ensures that the ECDL output is cleaned from any non-Gaussian beam profiles.

While adjusting the diffraction angle through a screw on the grating mount contributes to the frequency tuning of the ECDL, the preferred methods for fine-tuning the ECDL output frequency involve regulating the enclosure temperature with a Peltier element and adjusting the laser current of the diode. These methods are less intrusive to the ECDL formation compared to adjusting the grating angle. Additionally, to investigate the frequency response in experimental systems like atomic or cavity spectroscopies, we introduce a periodic stimulation input (stim-in)

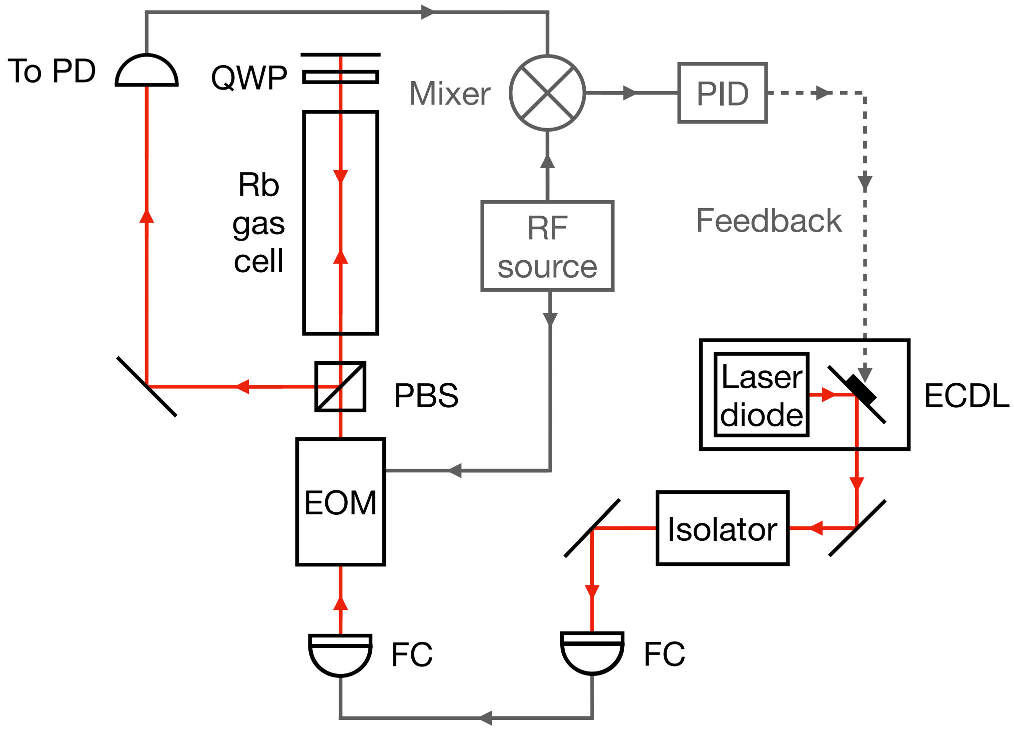

Figure 4.3: The atomic spectroscopy setup in FMS configuration. The ECDL is isolated from the spectroscopy setup to facilitate its individual adjustment. An electro-optic modulator (EOM) modulates the phase of the pump beam with a radio-frequency (RF) source operating at 20 MHz. The photodetector (PD) measure the modulated intensity of the probe and generates an error signal. This error signals is then processed through a proportional integral derivative control (PID) to adjust the ECDL actuator for frequency locking.

signal to the grating actuator via an actuator element attached to the grating mount. This signal scans the frequency around the laser resonance to generate the error signal required for atomic spectroscopy (see Section 4.1.2). It achieves this by perturbing the external cavity length, thereby shifting the laser frequency in relation to the stimulation input frequency and amplitude. In our ECDL systems, typical values for the stimulation input range from 0.1 V peak-to-peak to 1 V peak-to-peak for the amplitude and 5 Hz to 20 Hz for the frequency modulation.

4.1.2 Laser stabilisation via atomic spectroscopy

In addition to achieving a narrow linewidth, ensuring the stability of laser frequencies is crucial. For this purpose, we employ Doppler-free saturated absorption

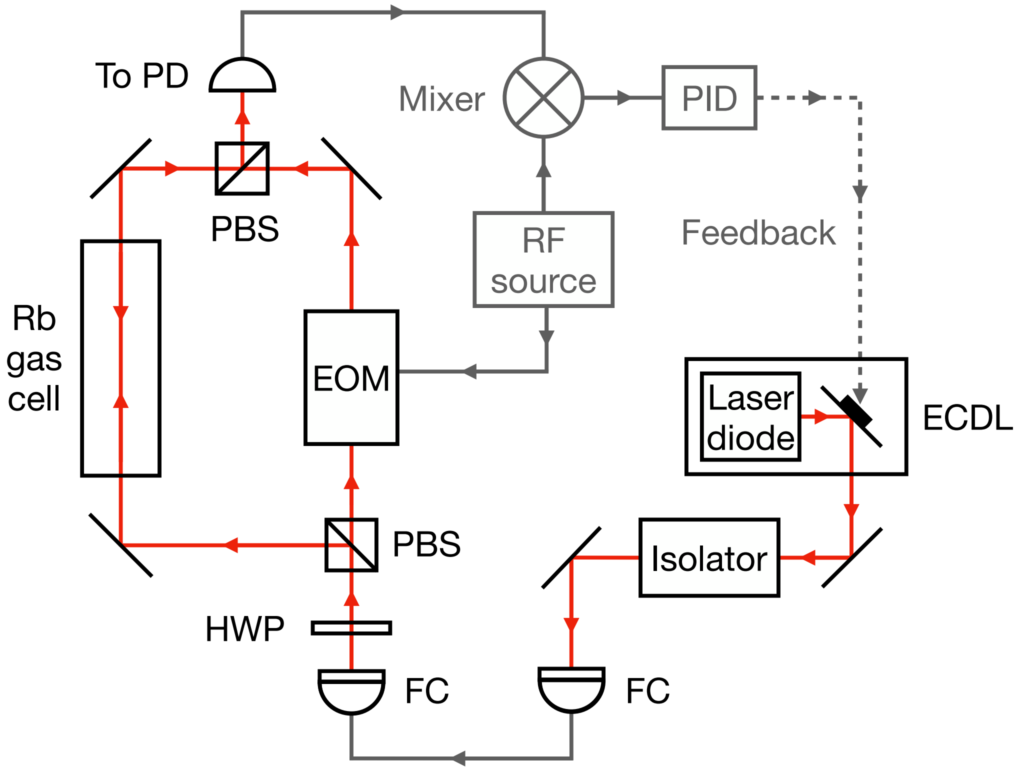

Figure 4.4: The atomic spectroscopy setup in MTS configuration. The ECDL is isolated from the spectroscopy setup to facilitate its individual adjustment. The ECDL output is divided into pump (horizontal polarisation) and probe (vertical polarisation) paths using a half-wave plate (HWP) and a polarising beam-splitter (PBS). An electro-optic modulator (EOM) modulates the phase of the pump beam with a radio-frequency (RF) source operating at 20 MHz. The photodetector (PD) measure the modulated intensity of the probe and generates an error signal. This error signals is then processed through a proportional integral derivative control (PID) to adjust the ECDL actuator for frequency locking.

spectroscopy [73] on atomic transition lines, utilising the Pound-Drever-Hall technique [74] on the error signal. The latter is obtained through the interaction of counter-propagating beams, a pump and a probe beam, passing through a Rubidium gas cell (Thorlabs GC19075-RB). The pump beam saturates the atomic transition, while the probe beam measures the changes in absorption and phase shift across the saturated atomic resonance.

There are two distinct cases for frequency modulating the beams, leading to two slightly different spectroscopy setups: frequency modulation spectroscopy [75] (FMS), and modulation transfer spectroscopy [76] (MTS). In FMS, the pump beam is

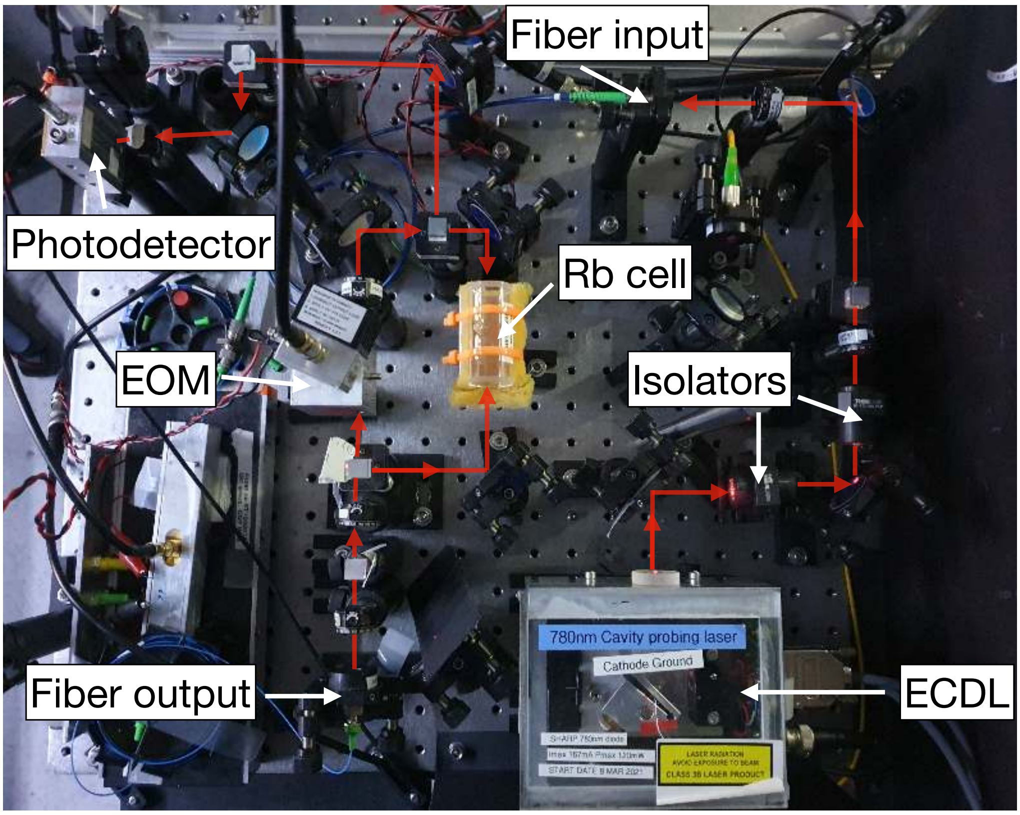

Figure 4.5: A picture of the MTS setup with its highlighted key components shown in Figure 4.4. The laser path is drawn in red.

frequency-modulated with an electro-optic modulator (EOM) driven at a resonance frequency of 20 MHz. The probe beam is obtained by reflecting the pump beam onto the same incoming path after passing through the Rb gas cell (see Figure 4.3). In MTS, the pump and probe beams follow separate paths, and the EOM is placed on the pump beam path (see Figure 4.4). The modulation of the pump beam is then transferred to the probe beam via four-wave mixing when close to the atomic resonance. This difference in modulation settings is reflected in the error signal collected by the photodiode. FMS displays a substantial background error signal, proportional to the laser intensity, due to modulation effects in off-resonant regions. MTS bypasses this background error signal thanks to the resonance condition necessary for the four-wave mixing process. However, only cycling atomic transitions can generate an error signal in this configuration.

From the generated DC error signal, we apply an analog proportional integral derivative (PID) controller to provide feedback to the grating actuator, thereby locking the frequency of the laser. The demodulation and PID lock are done using a home-built FM circuit board.

To further control the laser frequency, we employ acoustic-optical modulators (AOMs) to shift the laser frequency away from an atomic transition. The laser passing through the AOM experiences a frequency shift via diffraction through the sound waves in the AOM's crystal, by a multiple integer of the AOM driving frequency. While higher diffracted orders are available, the positive and negative first orders are of interest due to their efficiency, which can be maximised to reach approximately 85 % by adjusting the tilt angle of the AOM's crystal. The AOMs in our system feature centre frequencies of 80 MHz (Crystal Technology 3080-122) and 200 MHz (Crystal Technology 3200-124), providing a versatile range of frequency shifts, spanning from 70 MHz up to 230 MHz. For a broader tuning range, the AOMs can also operate in a double-pass configuration. Another advantage of AOMs is their ability to swiftly toggle their output on/off, with a rise/fall time of less than 100 ns, facilitating the effective implementation of experimental sequences (see Section 5.2.1).

4.1.3 Vacuum system

To trap a cold atomic ensemble, an UHV environment is necessary. Additionally, for optimal optical access to our cavity system, we utilise a glass cuvette (see Figure 4.6), externally coated with an anti-reflective coating that reduces reflectivity to $R < 1\%$ and prevents the etalon effect between the cuvette walls. The cuvette has dimensions of 100 mm × 25 mm × 25 mm. Connected through a DN35CF flange, it interfaces with a central cube housing the atom dispenser (SAES Rubidium AMD), powered by an external supply operating at 2.4 A. The blocker, detailed in Section 3.3.3, is positioned between the glass cuvette and the central cube. For UHV compatibility, the actuators' electrical wires are connected to the exterior using a UHV-compatible cable (MDC Precision Type-D 9 Pins) and an electrical feedthrough (MDC Precision Multipin Feedthrough Conflat Flange) located at the bottom of the central cube.

Additionally, the vacuum chamber incorporates an ion pump (Agilent VacIon Plus 20) to maintain the vacuum when reaching the desired pressure, an ionisation gauge

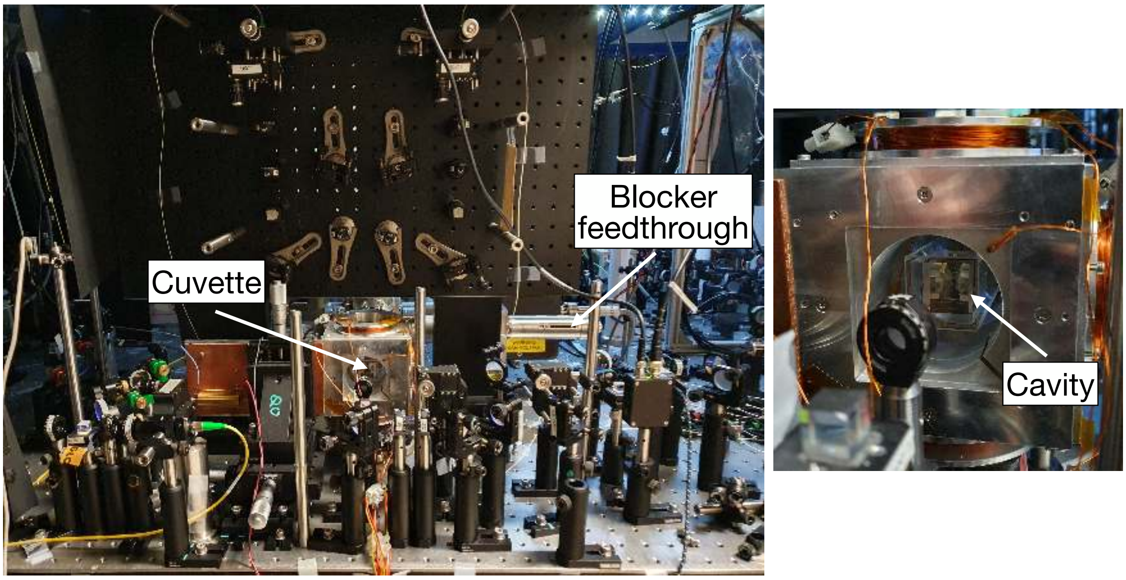

Figure 4.6: The front side of the vacuum system (left) with the magneto-optical trap and dipole trap optics, and magnetic coils. The close-up on the glass cuvette (right) shows the cavity stage inside the vacuum.

(Varian UHV-24) to measure the pressure in the chamber, a titanium sublimation pump (Agilent TSP Cartridge Filament Source), and a valve (MDC Precision All Metal Angle Valve 1.5") (see Figure 4.7). This valve connects to an external vacuum chamber for the intitial rough pumping, equipped with a turbomolecular pump (Pfeiffer Vacuum HiCube 80 Classic with rotary vane backup pump) and a vacuum gauge (Pfeiffer Vacuum PKR 251 with Pirani and cold cathode gauges).

To evaluate the pressure inside the chamber, we have three measurement tools at our disposal. The first is the Pirani gauge, connected to the external vacuum chamber via the turbomolecular pump. This gauge can measure pressures inside the chamber down to 10^{-7} Torr when the valve is open. However, since the turbomolecular pump cannot operate below 10^{-7} Torr, we cannot utilise this gauge during the operation of our UHV. The second tool is the ionisation gauge, which serves as the primary pressure gauge and measures down to 10^{-11} Torr. However, using the ionisation gauge adds extra mechanical noise to the vacuum chamber due to its operational vibrations. Consequently, it is not feasible to use this gauge concurrently with the operation of our cavity. To address this issue, we rely on the ion pump current,

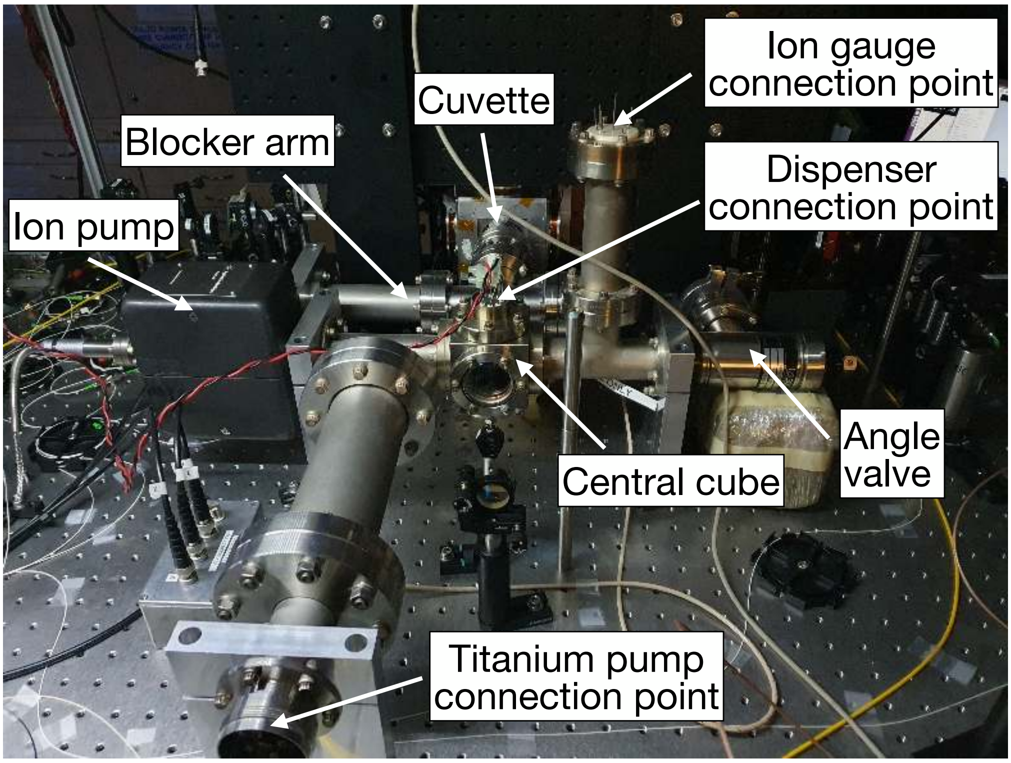

Figure 4.7: The back side of the vacuum system with its different components. All pumps and gauges are disconnected from the vacuum chamber, at the exception of the ion pump, to avoid additional mechanical noise from the respective devices.

which can be correlated with the vacuum pressure down to approximately 10^{-9} Torr, assuming a previously calibrated relationship with the ionisation gauge.

Protocol to reach UHV

Our desired target pressure to operate the cold atomic cloud is around 2×10^{-9} Torr, providing a trapping lifetime of around 1 s for a single atom. Initially, the chamber undergoes pumping with the turbomolecular pump, achieving a pressure of approximately 10^{-6} Torr within one day. Simultaneously, the titanium sublimation pump is outgassed during this process, by applying a 40 A current to each filament for 1 minute while maintaining a pressure below 10^{-3} Torr. Subsequently, the ion pump is activated to consistently pump down the main chamber, ensuring pressure maintenance and degassing of its filaments.

Upon reaching a vacuum chamber pressure of 10^{-6} Torr, we initiate the baking process for the entire vacuum system to speed up the outgassing process of volatile particles within the chamber, significantly reducing the vacuum pressure. The chamber is covered with heat tapes and layers of aluminum foils to ensure thermal isolation and achieve a uniform temperature distribution. Before starting the baking, we extend the blocker to prevent the line-of-sight between the cavity system and the Rubidium dispenser, as the latter will be heated up due to the baking and might release debris onto our system. The chamber's temperature is gradually increased, and the pressure is closely monitored to not exceed 5×10^{-6} Torr, ensuring the ion pump continues to operate and facilitate degassing. The target baking temperature is set to 120 °C, constrained by the maximum baking temperature of the sealant (Torr Seal) used in the system to glue the cuvette to the flange. The baking process concludes when the vacuum chamber pressure decreases at a slow rate, i.e., less than a 5 % reduction within 24 hours of baking. Following this, the chamber's temperature is gradually lowered to mitigate temperature differentials between the stainless steel main chamber and the glass cuvette, thereby reducing the risk of damage to the cuvette.

When the temperature throughout the vacuum chamber reaches approximately 80 °C, the valve isolating the main and external vacuum chambers is closed. We then allow the vacuum chamber to cool down to room temperature. Once this process is complete, and assuming there are no leaks or significant outgassing, the pressure within the system stabilises at a high value of 10^{-9},Torr. Subsequently, the titanium sublimation pump is activated for one minute with a current of 42,A to further reduce the pressure to around 2×10^{-9},Torr. However, as the vacuum pressure gradually increases over time, the titanium pump needs to be employed every few months to maintain optimal vacuum conditions.

4.2 Measurement methods for cavity parameters

An essential aspect of our experimental setup involves a comprehensive understanding of cavity properties. This knowledge is pivotal for predicting the cooperativity of the atom–cavity system and mitigating systematic errors in our experiments. This section delves into various techniques for characterising cavity parameters, including the free spectral range, critical distance, finesse, and cavity losses. Several of these parameters can be readily obtained by observing and fitting the cavity transmission and reflection spectra, following the methodology outlined by Hood et al. [55]. The following chapters adhere to the methodologies outlined in this section, ensuring consistency and reliability.

4.2.1 Probing the free spectral range and critical distance

The relationship between the free spectral range (FSR) ν_{FSR} and the cavity length L is given by the expression $L = c/2\nu_{FSR}$, where our approximate cavity length of 11 mm results in an FSR of $\nu_{FSR} \sim 13.6$ GHz. Conversely, an accurate measurement of the FSR would provide information about the cavity length and its distance from the concentric point, determined by the critical distance.

Two methods are available for FSR measurement. The first method involves phase-modulating a laser and coupling it to the cavity. The cavity transmission spectrum displays the carrier and the two sidebands with frequencies ν_{sb}. By modifying the modulation frequency, the two sidebands overlapp when the frequency spacing between the carrier and sideband approaches $\nu_{FSR}/2$. In order to measure our cavity length accurately, with an uncertainty below 10 nm, using this technique, we require a modulation frequency of about $\nu_{FSR}/2$ with an accuracy of 800 kHz. Additionally, the cavity's linewidth needs to be relatively narrow. However, the ideal linewidth of our NC system, at $\delta\nu = 21.8$ MHz, is too broad for this level of accuracy.

The second method relies on measuring the resonance frequency of the cavity's fundamental mode LG_{00} with a laser via a wavelength meter (HighFinesse WS7-60), which possesses an accuracy of 10 MHz. By tuning the laser frequency upward or downward and locating the next resonance frequency of the cavity fundamental mode while monitoring the cavity transmission, the FSR value can be determined. Repeating this process provides an estimated uncertainty ranging from 10^{-3} GHz to 10^{-2} GHz. While sufficient for obtaining the FSR value, this uncertainty level is not precise enough to accurately determine the cavity length. To accurately measure the cavity length, we make use of the transverse modes spacing described in Section 2.2.2, assessing the critical distance d.

In a well-aligned NC cavity where the input beam mode closely matches the cavity fundamental mode, the mode-matching to higher order modes is minimal.

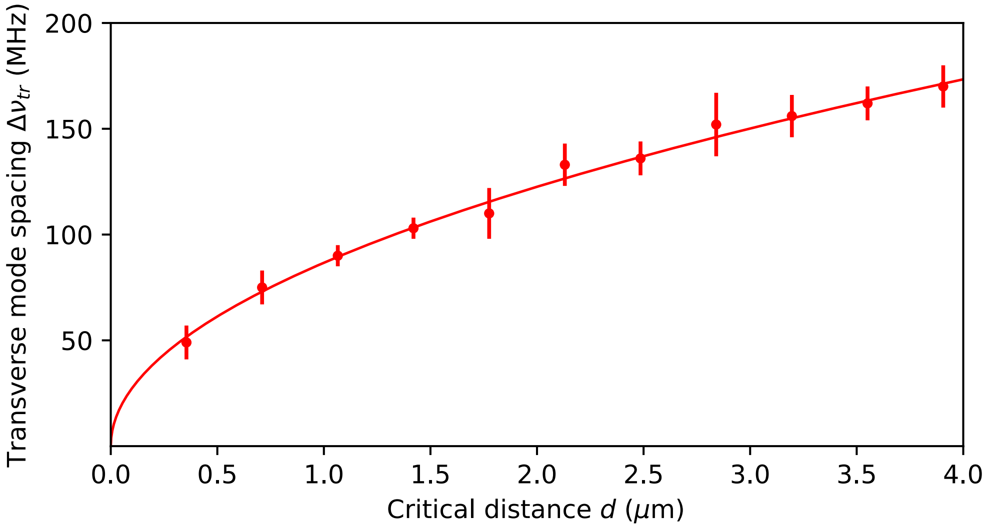

Figure 4.8: The variation of transverse mode spacing $\Delta\nu_{tr}$ for different critical distances d. The solid line is the theoretical fit. From the fit, the final stable critical distance is found to be at $d = 355.1$ nm. The standard deviation of the measurements is represented by the error bars.

However, by slightly misaligning the input beam with respect to the cavity mode, we introduce some coupling to higher order modes without altering the cavity length or the critical distance. The cavity transmission is monitored using a CCD camera and an amplified photodiode (Thorlabs PDA36A2) to distinguish the transverse modes. The transverse mode spacing $\Delta\nu_{tr}$ is evaluated at the maximum transmission of the fundamental mode and the first order mode. Extracting the frequency of the spacing involves using a reference. This frequency reference can be obtained through the spectroscopy error signal of an unlocked laser, where the spacing between two cycling transitions serves as the reference, or by modulating the probe laser with an EOM, with the sidebands serving as the reference. The measurement is repeated multiple times to account for uncertainty in $\Delta\nu_{tr}$.

Figure 4.8 displays the transverse mode frequency spacing $\Delta\nu_{FSR}$ for various critical distances d, while resonant with the 780 nm probe laser. To compare with theoretical predictions, Equation 2.33 is plotted against the data. The good agreement of the data points with the theoretical predictions endorses the use of transverse mode spacing to determine the critical distance. Additionally, the fitting yields a critical distance of $d = 355.1$ nm for the last stable resonance.

4.2.2 Probing the cavity spectrum and losses

Building on the approach outlined by Hood et al. [55], we express the transmission and reflection spectra of the cavity as ratios of transmitted and reflected powers with respect to the incoming power respectively, for a fix frequency

$$T = \frac{P_t}{\eta P_{in}} \tag{4.1}$$

and

$$R = \frac{P_r - (1-\eta)P_{in}}{\eta P_{in}}, \tag{4.2}$$

where P_t denotes the laser power transmitted through the cavity, P_r the laser power reflected by the cavity, P_{in} the input power, and η the spatial mode-matching factor. The mode-matching factor quantifies how much of the input light couples to the cavity fundamental mode. Assuming identical transmission and reflection coefficients for both cavity mirrors and reflectivity close to 100 %, we can express T and R in terms of the system losses, i.e., κ_{loss} due to scattering and absorption by the mirrors, and κ_{out} due to coupling to a propagating field mode (see Figure 2.2)

$$T = \frac{\kappa_{out}^2}{(\kappa_{out} + \kappa_{loss})^2} \tag{4.3}$$

and

$$R = \frac{\kappa_{loss}^2}{(\kappa_{out} + \kappa_{loss})^2}. \tag{4.4}$$

From there on, Equations 4.3 and 4.4 fully evaluate the total cavity decay rate $\kappa = \kappa_{out} + \kappa_{loss}$, which corresponds to twice the cavity linewidth (see Equation 2.14) of the system. By fitting the measured transmission or reflection spectra, we can assess the rates accordingly, granting access to mirror properties such as the cavity finesse $\mathcal{F}$.

For experimental acquisition of the cavity transmission and reflection spectra, an unlocked laser with a stimulation input signal is employed, inducing periodic and near-linear variations in laser frequency to record the transmitted cavity signal with an amplified photodiode (Thorlabs PDA36A2). Using a frequency reference obtained through atomic spectroscopy or EOM modulation frequency, we measure the the full width at half maximum (FWHM) of the transmission or reflection spectra fundamental mode, representing the cavity linewidth and, hence, the total decay rate of the system κ.

In order to extract each losses and the mode-matching factor from the cavity transmission and reflection, we introduce the effective cavity transmission

$$\alpha = \frac{P_t}{P_r - P_{in}} = \frac{\kappa_{out}^2}{\kappa_{loss}^2 - \kappa^2} = \frac{\kappa_{out}}{2\kappa_{loss} + \kappa_{out}}. \tag{4.5}$$

Note that α is solely defined by the cavity losses and is therefore an inherent property of the cavity mirrors, measured through the acquisition of the cavity transmission and reflection spectra. α is maximum for perfect mirrors with no scattering losses. Thus, each decay rate can be extracted from the measurement of α and is determined as

$$\kappa_{out} = \frac{2\kappa\alpha}{1+\alpha} \tag{4.6}$$

and

$$\kappa_{loss} = \frac{\kappa(1-\alpha)}{1+\alpha}. \tag{4.7}$$

Furthermore, by substituting Equation 4.6 and Equation 4.7 into Equation 4.1 we can evaluate the mode-matching factor of our system in function of α

$$\eta = \frac{\kappa(1+\alpha)}{2\alpha}\frac{P_t}{P_{in}}. \tag{4.8}$$

The experimental characterisation of these values was conducted in prior work in our group [58], corresponding to $\kappa_{out} \approx 0.958\,\kappa$ and $\kappa_{loss} \approx 0.04\,\kappa$ for Equation 4.6 and Equation 4.7, respectively.

4.3 Cavity stabilisation protocols

Maintaining resonance of our NC cavity fundamental mode LG_{00} with the targeted atomic transition requires stability in three degrees of freedom: longitudinal and transverse directions. Our focus is on optimising the coupling of incoming light to effectively mode-match into the cavity fundamental mode LG_{00}. In the experimental setup, misalignment fluctuations occur on two distinct timescales: long-term and short-term. Long-term variations, arising from gradual system changes like temperature fluctuations due to the cavity resting on the cuvette, unfold over minutes. These fluctuations along the cavity axis impact the cavity's resonance condition through alterations of the cavity length. To address this, we implement a lock system relative to a stable atomic transition. In the transverse direction, misalignment affects the mode-matching efficiency, influencing cavity transmission and fiber coupling. Employing a computer algorithm, we readjust the mirror displacement to enhance transmission and correct misalignment. Short-term fluctuations result from mechanical vibrations in the cavity setup, potentially requiring additional active strategies to minimise susceptibility to external mechanical noise. However, the passive performance of our NC cavity is already adequate for conducting atom–light experiments.

4.3.1 Longitudinal alignment stabilisation

The designated operational frequency for the cavity is the D_2 atomic transition of ^{87}Rb atoms at a wavelength of 780 nm. To avoid resonant scattering of trapped atoms in the cavity mode, we opt not to directly lock the NC cavity to a 780 nm laser. Instead, the NC cavity is locked at another resonant frequency, a multiple of the cavity FSR, specifically at 810 nm. To ensure stability transfer to the locking laser, a four-module chain incorporates intermediate locking modules (refer to Figure 4.9). At the core of this locking chain is the transfer cavity. Locked to a 780 nm resonant laser, the transfer cavity conveys the atomic stability to the 810 nm lock laser, which is locked to the transfer cavity. Moreover, the lock laser serves the purpose of the far-off-resonance trap (FORT) as detailed in Section 5.1.2.

Figure 4.9 illustrates the schematic of the transfer cavity chain, where the stability of the resonant laser is conveyed to the lock laser using the transfer cavity. The transfer cavity consists of two near-planar mirrors with a reflectivity of $\mathcal{R} = 99.94\,\%$ (ATFilms), resulting in a finesse of 6200. Separated by an Invar spacer and a piezoelectric tube, the cavity has a length of 1.17 cm, corresponding to a FSR of 12.8 GHz and a linewidth of 2.8 MHz. To minimise frequency fluctuations, the transfer cavity is enclosed within a compact vacuum chamber at a pressure of 5×10^{-6} mbar, and its temperature is regulated using heating tapes. This ensures that temperature fluctuations are reduced to approximately 100 mK, corresponding to a resonant frequency fluctuation of 42 MHz in the transfer cavity.

Further active stabilisation is achieved through the piezoelectric tube by employing the PDH technique to lock the transfer cavity length to the 780 nm resonant laser. For the locking of the 810 nm lock laser to the transfer cavity, the laser frequency is

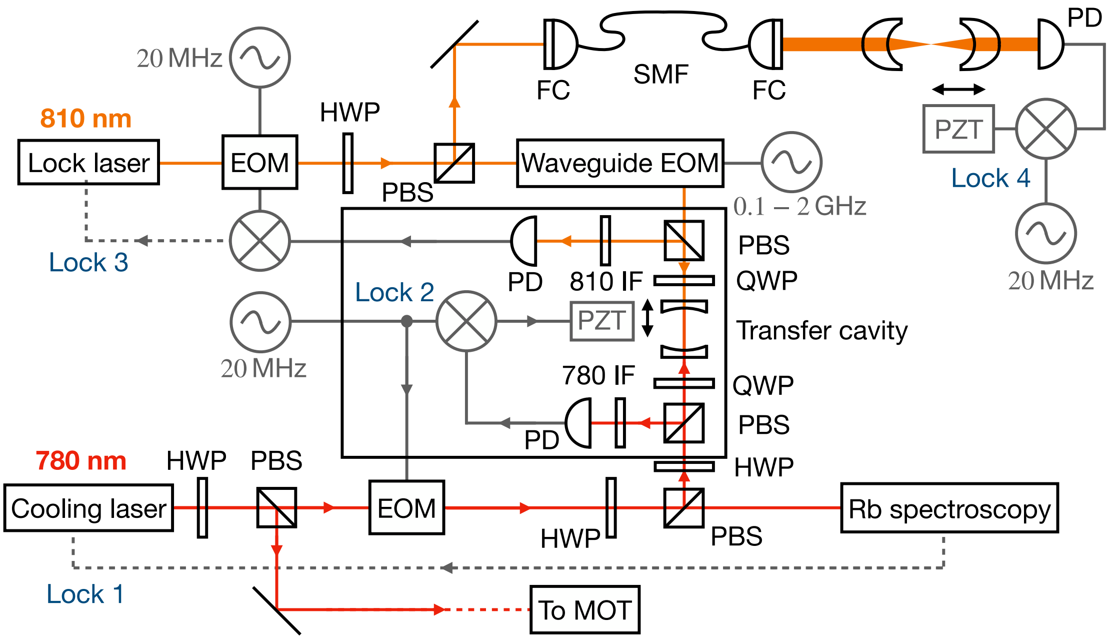

Figure 4.9: The setup schematic of the transfer cavity stabilisation chain. The procedure involves four consecutive locking modules: lock 1 to 4. Lock 1: 780 nm resonant laser locked to the ^{87}Rb D_2 transition using an atomic spectroscopy. Lock 2: length of the transfer cavity locked to the resonant laser through a piezoelectric actuator (PZT) and a reflection error signal. Lock 3: a waveguide EOM introduces frequency sidebands of 0.1 GHz to 2 GHz on the 810 nm lock laser, and one of the sidebands is then locked to the transfer cavity. Lock 4: NC cavity locked to the 810 nm lock laser, via controlling its piezoelectric actuators and a reflection error signal. Modifying the modulation frequency of the waveguide EOM allows for the fine-adjustment of the NC cavity resonance frequency. Both cavity locking methods employ the conventional PDH technique featuring 20 MHz phase modulations. Key components include the EOMs, PD (high-bandwidth photodetector), HWP (half-wave plate), QWP (quarter-wave plate), PBS (polarising beam splitter), SMF (single-mode fiber), FC (fiber coupler), and IF (interference filter).

modulated using a waveguide EOM (EOSpace 10 GHz Phase Modulator) to generate frequency sidebands ranging from approximately 0.1 GHz to 2 GHz. One of these sidebands is then locked to the transfer cavity, effectively transferring the long-term stability of the atomic resonance to the lock laser. The use of sidebands, rather than the carrier, allows for the tunability of the NC cavity resonance by simply adjusting the sidebands' frequency. Subsequently, the NC cavity is locked to the 810 nm lock laser through an error signal derived from the transmission of the lock laser through the NC cavity. This error signal is used to apply a PID control loop on the axial direction of the cavity stage, regulating the actuators lengths. It's worth noting that the NC cavity resonance can be tuned while maintaining its lock, as long as the modification of the sidebands' frequency is gradual and within a small range of approximately 2 MHz/s.

4.3.2 Transverse alignment stabilisation

Ensuring precise transverse alignment is crucial for a NC cavity due to the strongly focused modes, particularly at small critical distances. Small temperature fluctuations can lead to thermal expansion or contraction of the cavity stage, causing transverse misalignment. A straightforward solution involves enclosing the vacuum chamber and the optics in a temperature-stabilised environment. However, internal thermal sources, such as the Rubidium dispenser and quadrupole coils, can impact the cavity temperature, necessitating precise control of the temperature stabilisation process. An alternative approach is to actively compensate for any transverse displacement, using the cavity actuators, and continuously monitor the cavity transmission of the lock laser over time. Deriving an error signal for the transverse regime is challenging, making this two-dimensional lock algorithm a preferred option. The algorithm activates once the transmission drops below a set threshold and operates as follows. Assessing the cavity transmission over time relative to its initial value, the algorithm realigns the transverse profile through fine adjustments to the actuators length in all possible directions. It proceeds towards the steepest ascent in transmission until the original value is recovered. The scanning step size decreases as the cavity transmission increases, preventing unnecessary over-correction near the optimal alignment position. This algorithmic method is known as the gradient-search

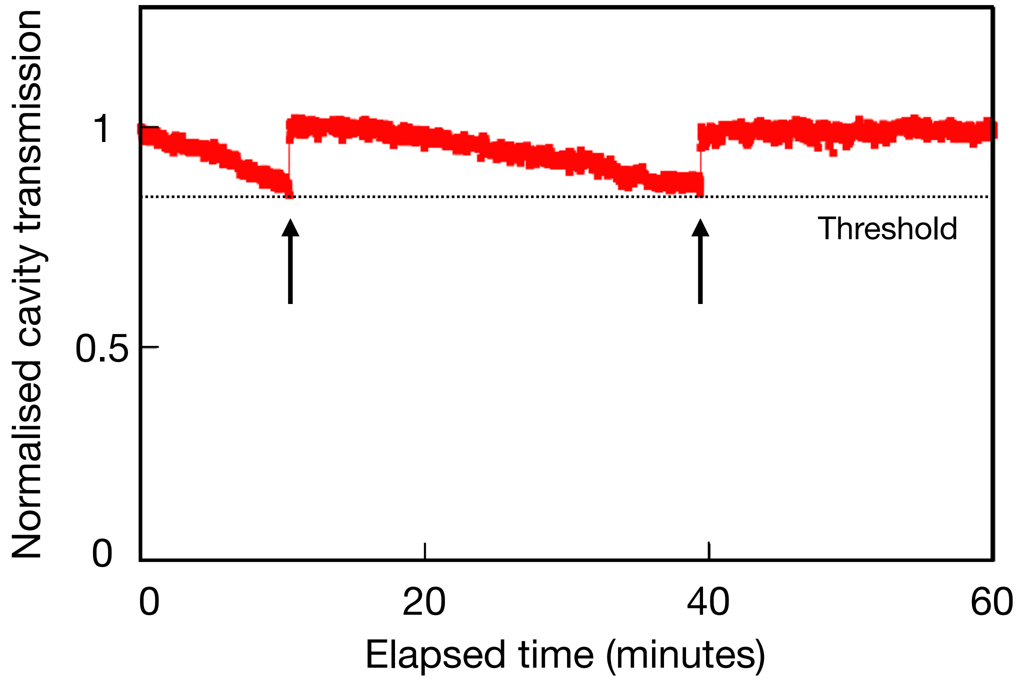

Figure 4.10: The long term transverse stability of the NC cavity. The slow drift in cavity transmission, mainly caused by temperature changes, is in the order of minutes. When the transmission drops below the threshold set at 0.8 (arrows) the stabilisation algorithm activates to recover the initial transmission value.

method and is widely covered in numerical methods literature [77].

Figure 4.10 illustrates a cavity transmission trace over time during the activation of the transverse stabilisation algorithm. Despite temperature drifts taking minutes, the stabilisation mechanism typically responds within seconds. The level of transverse stability is determined by the threshold, which can be adjusted for a higher duty cycle by setting it to a lower value, and vice versa.

4.3.3 Cavity stability measurement

To characterise the susceptibility of the mounted cavity to external noise, the cavity resonance shift $\delta\omega_C$ is measured with respect to a laser, either the 780 nm probe laser or the 810 nm lock laser, to which the cavity is loosely locked via the PDH technique through an integral controller with small gain, with an integral time of 0.5 s. The importance of a loose lock allows for fast cavity length changes at high frequencies to be measured, while ensuring that the error signal remains in the

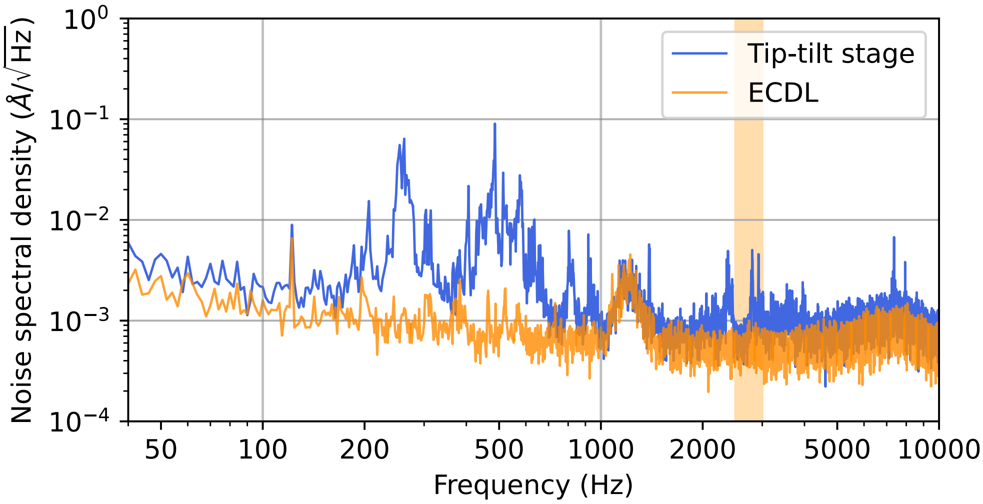

Figure 4.11: The noise spectral density of the cavity length over an integration time of 0.5 s at a critical distance $d = 1.06(5)$ µm. Total noise of revision 3 is 0.36(2) Å. 70 % of this total noise is contained in the spectral window between 200 Hz and 2500 Hz. The shaded region highlights the first resonance of the cavity as shown in Figure 4.13, which only accounts for< 1 % of the total mechanical noise. Tip-tilt stage: revision 3 of the cavity structure. ECDL: external cavity diode laser.

linear regime with respect to the length change δL, i.e., the mapping to frequency detuning stays injective. Therefore, any frequency detuning $\delta\omega_C$ between the cavity and the laser, caused by mechanical noise, remains uncorrected, enabling us to measure the mechanical noise δL by monitoring the error signal. The length change recorded over time results in a time trace $\delta L(t)$. The noise spectral density of the recorded trace is obtained by performing a discrete Fourier transform and is shown in Figure 4.11. The total root mean square (RMS) mechanical noise of the cavity system across the whole frequency spectrum is simply determined by integrating the noise power spectral density, or equivalently, by calculating the standard deviation of the time trace. In Figure 4.11, for revision 3, it amounts to $\delta L_{rms} = 0.36(2)$ Å, or a corresponding frequency uncertainty of $\delta\omega_C = 2\pi \times 1.28(5)$ MHz for the given cavity linewidth.

The recorded error signal combines both laser noise and cavity noise. To separate the two contributions, the laser noise is characterised independently via modulation transfer spectroscopy (see Section 4.1.2). The corresponding trace is shown in Figure 4.11 as well, with an integral total frequency uncertainty of

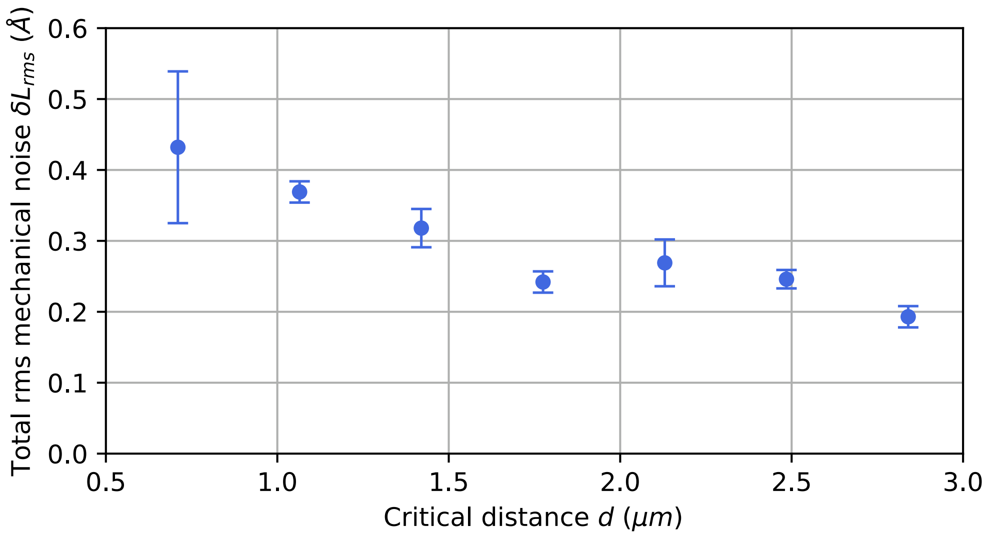

Figure 4.12: The total rms mechanical noise of the cavity length δL_{rms} over several critical distances d. The closer to the concentric point, the higher the noise becomes. The main noise contribution remains in the same spectral window between 200 Hz and 2500 Hz.

$\delta\omega_{Laser} = 2\pi \times 0.11(1)$ MHz.

More than 70 % of the total noise energy of the laser+cavity system is contained in a spectral window between 200 Hz and 2500 Hz, and dominated by cavity contributions. This noise contribution could be caused by the susceptibility of transverse vibration modes of the springs to external noise, ultimately coupling to the cavity length. Additionally, the shaded region on Figure 4.11, indicating the first mechanical resonance of the system and signifying higher sensitivity when excited at the frequency of 2750 Hz (see Figure 4.13), contributes to less than 1 % of the overall mechanical noise.

Note that, as we get closer to the concentric point, the measured cavity length displacement in the cavity structure goes up. This happens because the cavity is more sensitive to misalignment at short critical distances d, due to the highly focused cavity mode, leading to an amplification of the mechanical noise. Figure 4.12 shows how the noise evolves as we look at different critical distances.

To further increase the stability of the system, an active stabilisation scheme for the cavity can be considered if a feedback signal for the cavity length is available, e.g. through a PDH scheme described previously. For this, we measure the cavity

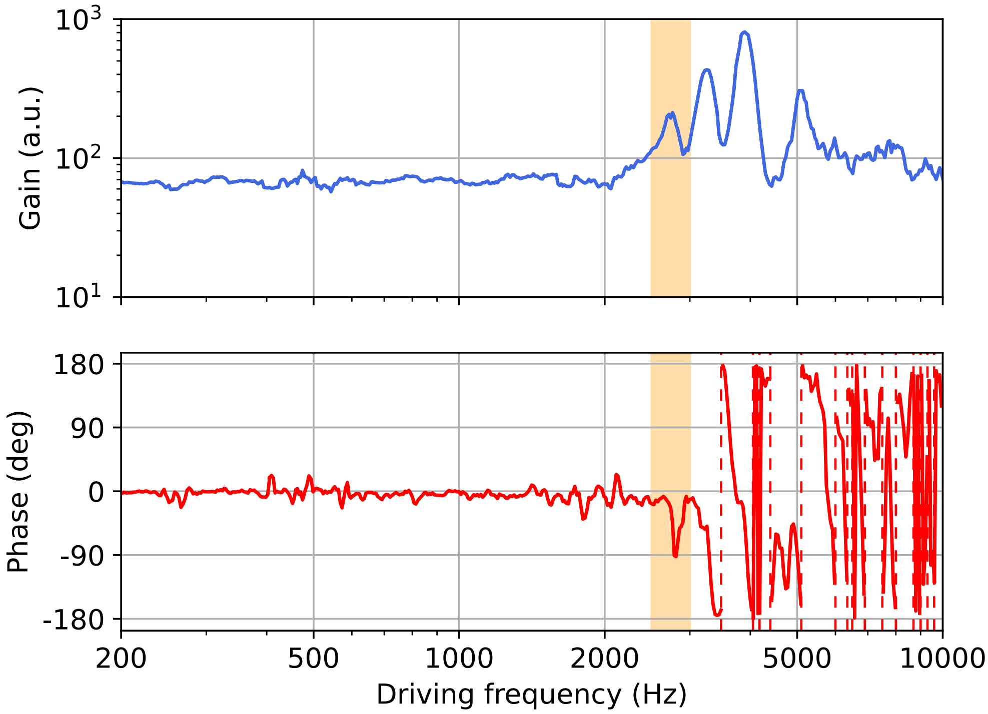

Figure 4.13: The cavity gain-phase response to the stimulus sent to the piezoelectric actuators. Shaded region highlights the first resonance of the cavity, centered at 2750 Hz. The gain up to 2 kHz remains linear, indicating a good behavior to implement a feedback loop.

resonance response to an actuator length change stimulus at different frequencies. A network analyser (Agilent E5061b) generates this stimulus, which is added to the actuator's voltage, and is picked up by the error signal from a PDH scheme in the same loose-lock configuration as above. The resulting Bode diagram of the system response is shown in Figure 4.13. A first resonance is observed around 2750 Hz, with a fairly flat phase response below this resonance. Establishing a phase margin of 60° as the limit of the control for an active stabilisation implementation, an active length control of the NC cavity system up to a control bandwidth of ≈ 2500 Hz is possible, removing the strong broad contribution from 200 Hz to 700 Hz representing 67 % of the total noise in the observed cavity noise spectrum.

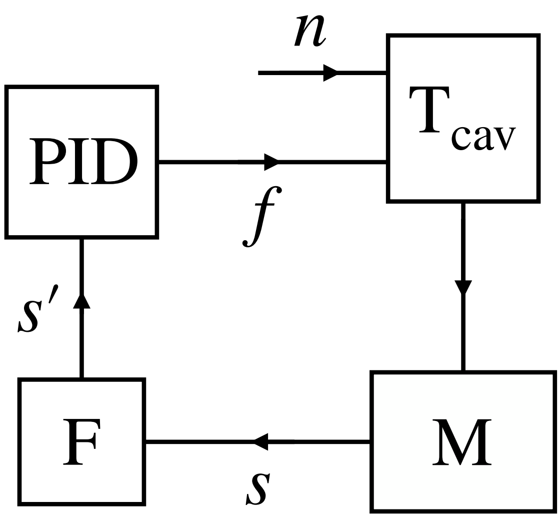

Figure 4.14: The block diagram illustrating the components contributing to the cavity response signal. The procedure incorporates a feedback loop employing an infinite impulse response digital filter (F) to regulate the phase of the feedback signal (s to s'), derived from the cavity error signal (M), leveraging the resonant gains of the cavity transfer function (T_{cav}). f represents the feedback from the PID control to the cavity actuators, ensuring stability of the cavity length with respect to the mechanical noise n.

4.3.4 Discussion on active stabilisation implementation

In revision 2, an active stabilisation process was introduced, with the goal of minimising noise in specific frequency regions as assessed in the noise spectral density. This involves employing a feedback loop with an infinite impulse response (IIR) digital filter to adjust the phase of the feedback signal to a range conducive to noise reduction, leveraging the resonant gains of the cavity stage. A large control bandwidth is advantageous in this approach, providing greater flexibility in fine-tuning the phase of the feedback signal. Here we offer a concise summary of the method employed in revision 2 for discussion purposes. For a more in-depth explanation, please refer to the previous work conducted in our group [59]. Figure 4.14 illustrates the schematic of the control sequence for the cavity response.

The IIR filter, employed for introducing a phase lead or lag, is represented by a simple transfer function $F(s) = N(s)/D(s)$, where $N(s)$ and $D(s)$ are polynomials with roots known as zeros (z) and poles (p), respectively. The IIR filter is implemented in an FPGA using a bilinear transform, i.e., mapping the continuous-time

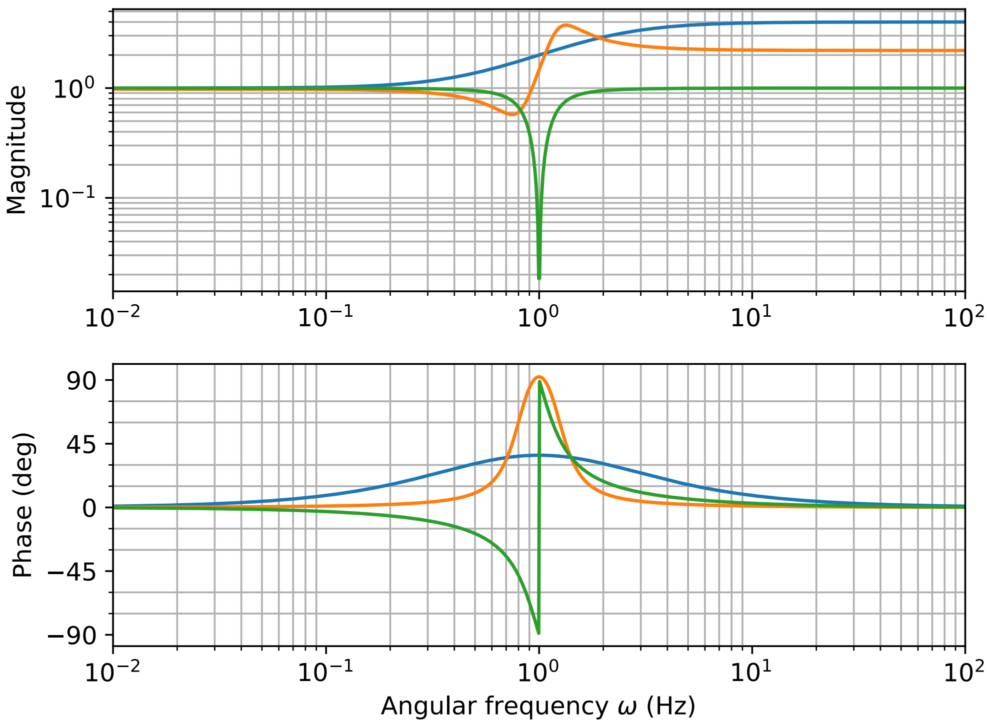

Figure 4.15: The standard gain-phase response of a phase lead transfer function $F(s)$ (blue: 1st order; orange: 2nd order) and a notch filter (green). The zero and pole of the 1st order transfer function are set to: $z = -0.5$ Hz and $p = -2$ Hz, respectively. For the 2nd order transfer function: $z = (i - 0.2)0.8$ Hz and $p = (i - 0.2)1.2$ Hz. As for the notch filter, its transfer function is defined by the notch frequency ω_n, the width of the rejection band $\Delta\omega_n = \omega_n/Q$, and the quality factor Q. The notch frequency and the quality factor are set to $\omega_n = 1$ Hz and $Q = 2$.

domain transfer function $F(s)$ to the discrete-time domain. Within the FPGA, the analog input signal is processed via an analog-to-digital converter (ADC) before going through the IIR filter. The latter is made of six cascaded digital biquad filters, with each biquad filter capable of handling up to second-order transfer functions. This configuration allows the IIR filter to accommodate the addition of six various transfer functions, including first and second orders, as well as notch filters designed to attenuate signals within a specific frequency range. The digital output is subsequently converted back to an analog signal using the ADC. Figure 4.15 displays the standard gain-phase response of these elementary transfer functions. The IIR filter demonstrates a latency of approximately 10 µs, resulting in an operating bandwidth of around 50 kHz. Opting for a digital filter over an analog one facilitates ease of

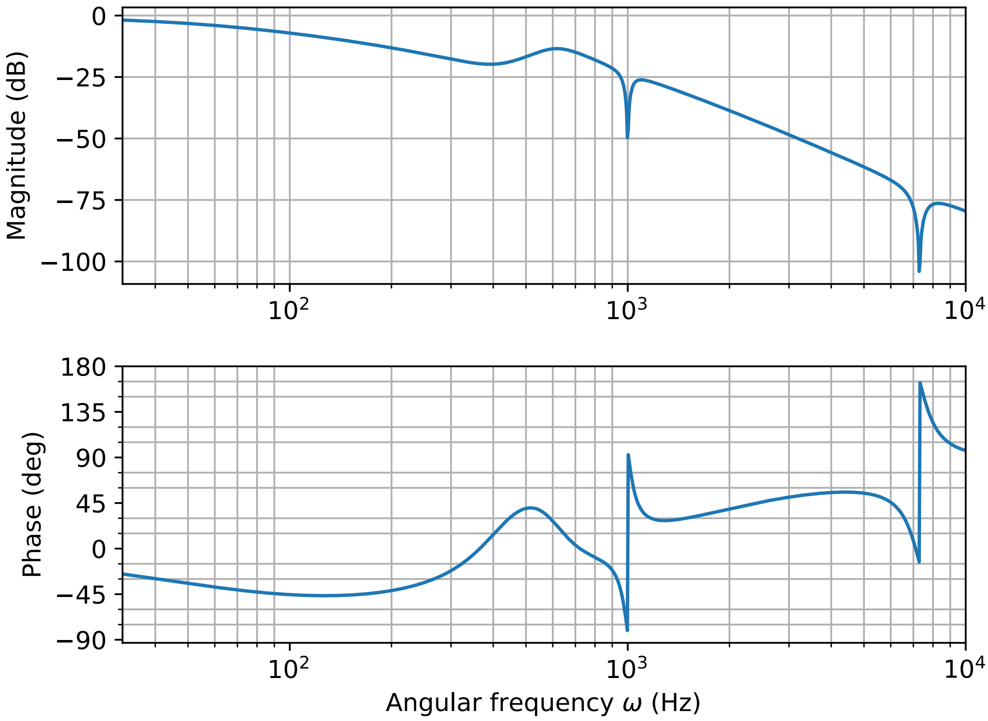

Figure 4.16: The gain-phase response of an applied IIR filter. This filter aims at reducing the strong noise contributions observed in the revision 2b noise spectral density, mainly located in the 300 Hz to 800 Hz region. Two additional contributions at the particular frequencies of 1000 Hz and 7200 Hz are dampened with notch filters. The choice of the optimal IIR filter implementation is empirical, with this specific filter providing the most effective noise reduction.

reprogrammability, enabling quick adjustments to target the frequency range of interest. This digital approach provides the flexibility to test and fine-tune different configurations efficiently.

An example of the active stabilisation process is given for revision 2b. The process first involves identifying the control bandwidth in the NC cavity system by examining its gain-phase response, and determining the noisy frequency regions through the noise spectral density analysis. Using this information, we design an initial IIR filter to introduce the necessary phase lead or lag, aiming to diminish the system's noise. The implemented IIR filter, comprising a mix of first and second-order transfer functions, facilitates attenuation across various frequency ranges. Figure 4.16 provides an example of an applied IIR filter. Once the IIR filter is integrated into the cavity feedback loop, we fine-tune its performance by gradually

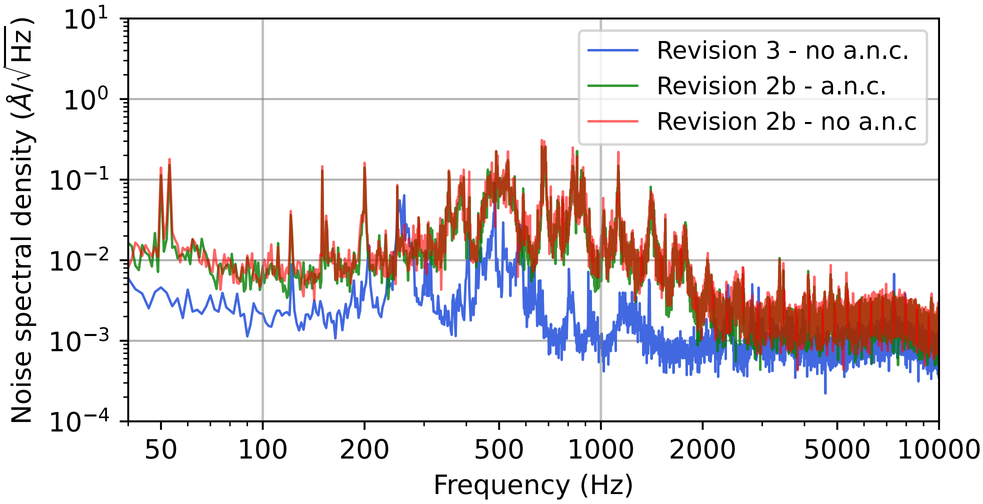

Figure 4.17: The noise spectral density comparison of revision 2b with active noise cancelling (a.n.c.), and revision 3 with only passive stabilisation (blue). The total noise of revision 2b without a.n.c. (red) is 1.7(2) Å, and 1.6(2) Å with a.n.c. (green). The total integrated noise obtained from revision 2b with a.n.c. only decreases by 5% compared to the system without active noise cancellation, which is not significant enough considering the additional implementation efforts required. The improved performance of revision 3, achieving nearly three times better results, can be attributed to the tensegrity structure of the stage, which avoids the cantilever behaviors observed in the flexural stage.

adjusting the proportional gain of the PID control for optimal noise reduction. Subsequently, we reassess the noise spectral density of the cavity to determine the overall noise level. Depending on the outcomes, where certain frequency regions may experience amplified noise, we may need to experiment with different IIR filters. The choice of the optimal IIR filter is empirical, with the specific filter in Figure 4.16 providing the most effective noise reduction. This iterative process offers a systematic approach to tailor noise reduction strategies for specific frequency regions.

For revision 2b, using the most effective IIR filter, as shown in Figure 4.16, the total integrated noise of the NC cavity system decreases by 5 % compared to the system without active noise cancellation (see Figure 4.17). While the active noise-canceling strategy effectively reduces the total noise in the system for revision 2b, the reduction is marginal. Moreover, the passive susceptibility to external noise of revision 3 already achieves satisfactory noise reduction for the current nominal finesse of our cavity system, with a mechanical noise about five times lower than revision 2b. The potential achievable finesse for revision 3, with its passive noise reduction, stands around 1600, which represents a fivefold increase from the current operational finesse of 323(8). Although implementing the active stabilisation process in revision 3 would increase the usable finesse, the inherent passive stability of revision 3 already provides a sufficient finesse for subsequent experiments. Moreover, the evident difference in total noise between revision 2b and 3 suggests that further investigations into the structural configuration of the NC cavity stage may yield more significant benefits compared to implementing the active stabilisation process.

Chapter 5

Atom–cavity interaction

This chapter presents the conventional approach for trapping atoms within the NC cavity using a magneto-optical trap (MOT), in conjunction with a far-off resonant trap (FORT) for single atom selection. The measurement sequence for the system is given, leading to the observation of the atom–cavity interaction through the modification of the cavity transmission by the atoms, referred to as the vacuum Rabi splitting. This splitting allows the extraction of atom–cavity interaction parameters for a set critical distance d. Lastly, the potential for implementing quantum logical gates using our cavity system is discussed.

5.1 Trapping atoms in a near-concentric cavity

To trap atoms in the cavity, we first prepare a cloud of Rubidium atoms to act as a reservoir, using a MOT. The purpose of the MOT is to lower the initial velocity of the atoms to facilitate loading in the FORT. By tuning the FORT potential, we can select how many atoms are loaded from the MOT to the FORT potential. The latter is located at the center of the cavity, where the electric field of the cavity mode is the strongest for better atom–cavity interaction. We present an implementation of such trap configuration for our cavity experiment. The lifetime of the atoms trapped is measured through atomic fluorescence, i.e., the scattering of the MOT lasers of the atoms. The longer the trapping time, the more measurement cycles can be carried out without reloading.

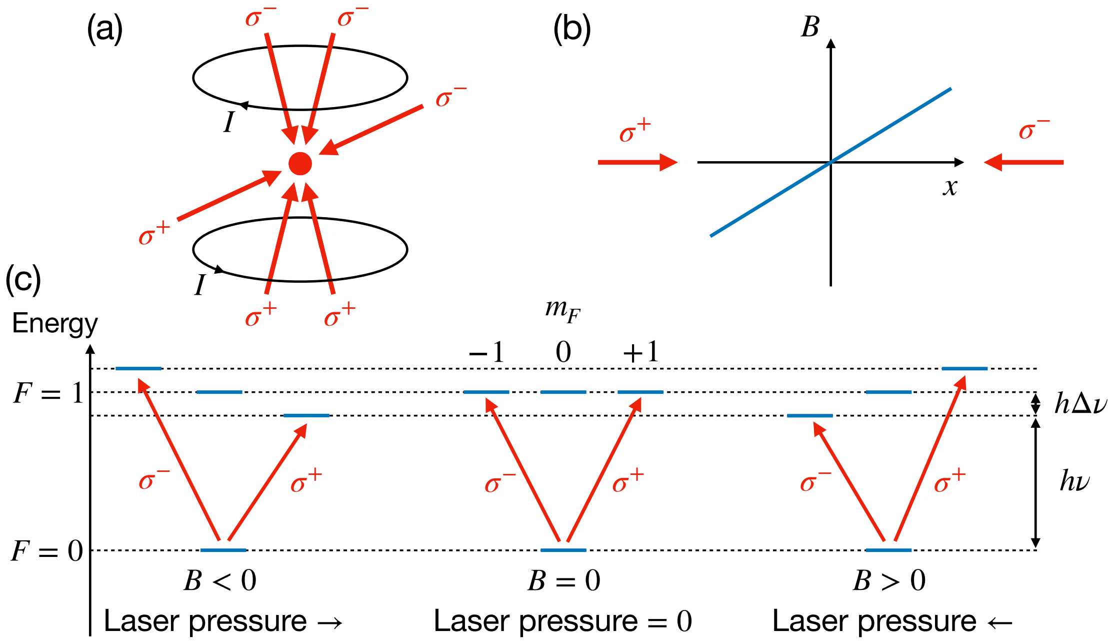

Figure 5.1: The schematic of the circularly polarised MOT beams configuration (a). The energy diagram (c) illustrates the Zeeman shift induced by the magnetic field B using a conceptual atom model with $F = 0 \rightarrow F = 1$ transition. The magnetic field gradient shifts the Zeeman sub-levels based on the atom position (b). The cooling beam, polarised to induce absorption and re-emission, exerts a force directing atoms toward the MOT center.

5.1.1 The magneto optical trap (MOT)

Working principle

The trapping of atoms in a MOT relies on two characteristics: a cooling component to reduce the velocity of the atoms, and a trapping component to localise atoms. The cooling component first consists of placing the atoms in an UHV (typically on the order of 10^{-9} Torr) to prevent collisions between the atoms and the background gases. To achieve this, the Doppler cooling technique [18] is employed, which consists of sending overlapping circularly polarised counter-propagating laser beams in three orthogonal directions. Due to the Doppler effect, moving atoms in the overlapping region preferentially absorb photons from the beam opposite to their motion. When an atom interacts with a photon by absorption or scattering, its momentum changes according to the law of momentum conservation. Since the

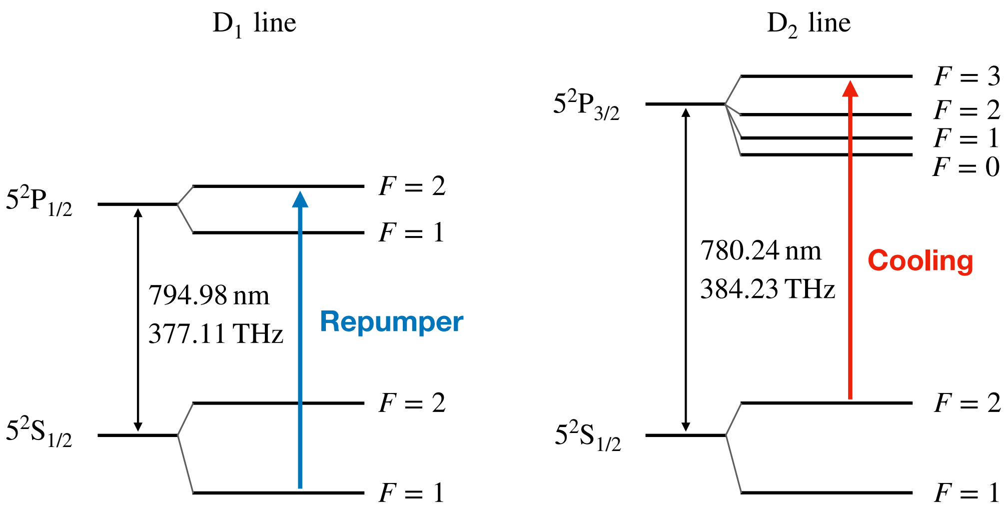

Figure 5.2: The energy diagram of ^{87}Rb with indication of the MOT lasers targeted transitions. From the cooling laser transition, the atoms can de-excite to the lower hyperfine level $F = 1$ of the ground state. The repumper helps to repopulate the hyperfine level $F = 2$ of the ground state by continuously exciting the atoms from the dark state $5^2S_{1/2}$ $F = 1$ to another excited state, which will then in turn de-excite to the wanted hyperfine level of the ground state necessary for the cooling transition.

scattering occurs randomly in all directions, the average momentum transferred to the atom through the emission process is zero. This leads to the atom slowing down in the opposite direction to its initial motion, creating an effective damping force proportional to the atoms' velocity. However, atoms will slowly diffuse over time and escape the lasers' beam waist. This is where the trapping component comes into play. The trapping region is delimited using a quadrupole magnetic field generated by two coils in anti-Helmoltz configuration, where the center region of the magnetic field lines exhibits zero magnetic field. When atoms deviate from the trap center, their atomic transition experience a Zeeman shift increasing with radial distance from the center (see Figure 5.1). By detuning the Doppler cooling beams to be resonant to the shifted atomic transition, it results in atoms being visible by the beams and then pushed back in the opposite direction, with the force proportional to their distance from the trap center. When de-exciting after interaction with the cooling beams, in our cycling atomic transitions, the atoms can go to a lower ground state than the initial one. To cope with this problem, the cooling beam is superposed with a repumper beam to push back the atoms to the correct initial

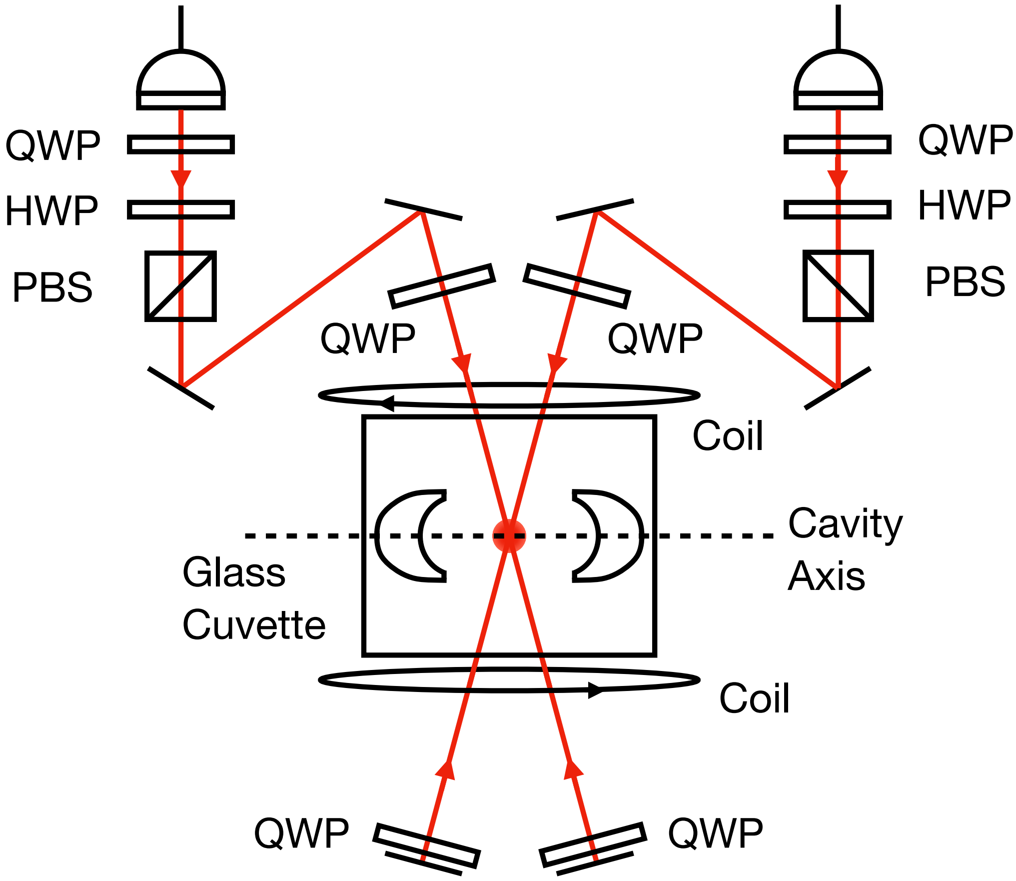

Figure 5.3: The schematic setup of the vertical optics of the MOT, the horizontal arm displays the same configuration of waveplates and back reflection with its path being perpendicular to the cavity axis and the vertical arms' plane. Each arm is retro-reflected with a quarter-wave plate (QWP) to change the polarisation sign on the retro-reflected paths. While the intersection angle of the vertical MOT arms is only about 15°, it is sufficient to achieve cooling inside the NC cavity. HWP: half-wave plate; PBS: polarising beam splitter.

ground state (see Figure 5.2).

MOT setup

As shown in Figure 5.2, the cooling process in our MOT relies on the closed cycling transition $5^2\mathrm{S}_{1/2}\ F = 2 \rightarrow 5^2\mathrm{P}_{3/2}\ F' = 3$, which corresponds to the D_2 line of ^{87}Rb. The cooling laser is red-detuned from that transition. Due to the possibility of decaying to the ground state $5^2\mathrm{S}_{1/2}\ F = 1$, which is a dark state for the cooling transition, the repumper laser is set to the D_1 line of ^{87}Rb, $5^2\mathrm{S}_{1/2}\ F = 1 \rightarrow 5^2\mathrm{P}_{1/2}\ F' = 2$, to repopulate the initial ground state $5^2\mathrm{S}_{1/2}\ F = 2$. The cooling laser is

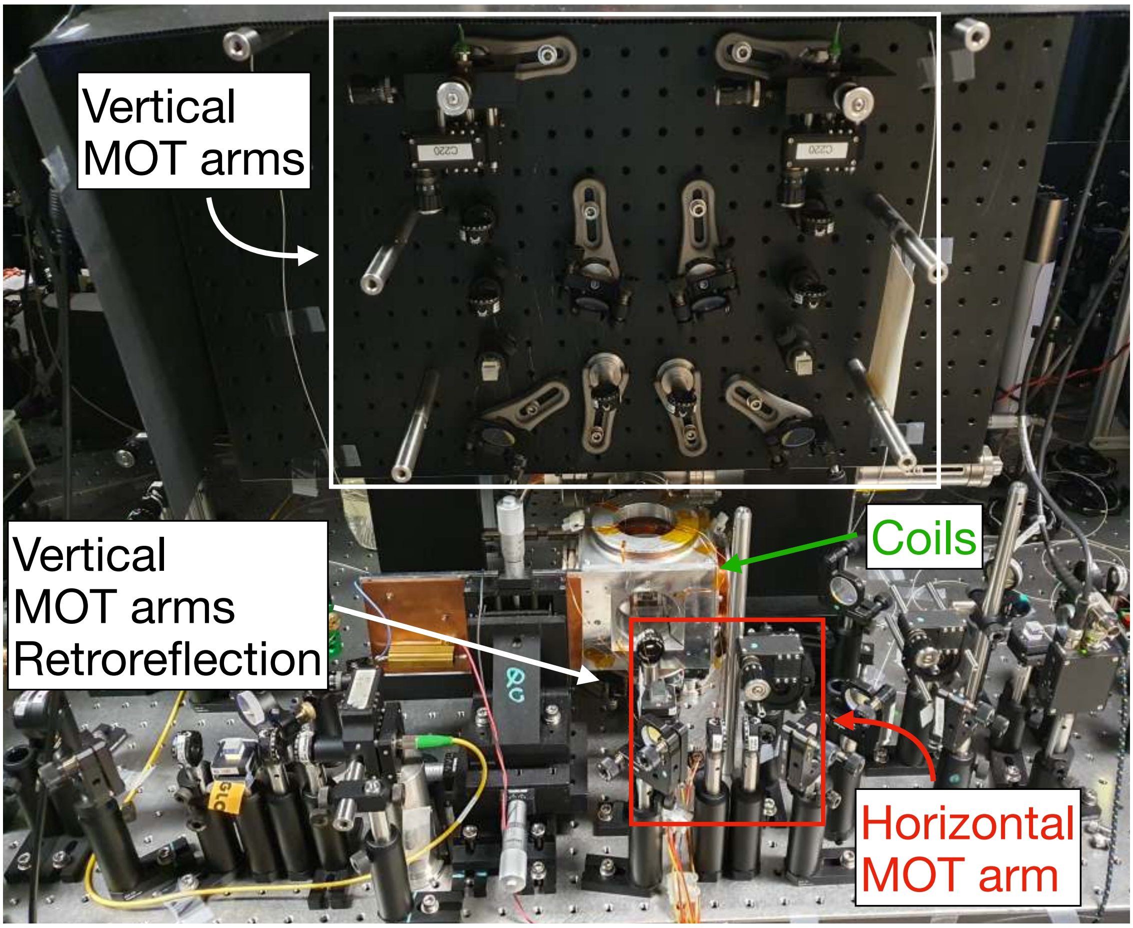

Figure 5.4: The optics forming the MOT arms with the coils centered around the glass cuvette. Each arm is retro-reflected using a mirror and a quarter wave-plate to invert the polarisation (hidden behind the vacuum system and under the coil mount). All the coils are mounted on a 3D translation stage to adjust the position of the zero point of the magnetic field.

locked to the D_2 line using a FM spectroscopy, and two single pass AOMs are used to red-detune the cooling beam by 10 MHz. The repumper laser is initially locked to the cross-over $5^2S_{1/2}$ $F = 1 \rightarrow 5^2P_{1/2}$ $F' = 1/2$, and its frequency is shifted up to be resonant with the $5^2S_{1/2}$ $F = 1 \rightarrow 5^2P_{1/2}$ $F' = 2$ transition using a double pass AOM. On top of shifting the frequencies, the AOMs also act as switches to turn on/off the respective laser beams during the measurement sequence. After the AOMs, both lasers are coupled to the same fiber.

To form the three arms necessary for the MOT, the combined lasers go through a fiber beamsplitter with a ratio 1:3, leading to one MOT arm being placed horizontally and two MOT arms being placed vertically with a tilt angle of about 15°. Each arm goes through quarter- and half- waveplates as well as a polarised beamsplitter to first clean the polarisation output of the fiber and create the circular polarisation $\sigma^{\pm}$. The polarisation of each arm is dependent on the gradient of the quadrupole magnetic field. Then, the arms are aligned through the cavity center, and the counter-propagating arms are obtained via back reflection with a mirror and go through a quarter-waveplate to flip the circular polarisation (see Figure 5.3). To eliminate the need for additional complex atom delivery setups and due to our system's high optical access, the MOT is positioned at the center of the NC cavity (see Figure 5.4). The nominal power in each arm is set to 100 μW for the cooling beam, and one third of the cooling power for the repumper beam.

The quadrupole magnetic field is generated by a pair of anti-Helmholtz coils, with a coil diameter of 6 cm and a coil spacing of 3 cm (see Figure 5.4). Each coil comprises of 160 turns of a AWG 22 copper wire, achieving large field gradients necessary for the MOT of about 20 G/cm along the coil axis and −10 G/cm in perpendicular directions from the zero magnetic field region located at the center of the coil setup. The coils are run with around 1 A current, generating heat of about 3.2 W. Note that a higher current or additional coil windings are necessary to scale up the vacuum system. In addition, coil windings scale quadratically with the coils diameter, hence the use of a small glass cuvette in our case to minimise the coils size. In scenarios involving scale-up, careful consideration of heat management becomes crucial. For instance, doubling the size of the coil setup and the wire diameter from our actual configuration would necessitate a current of 4 A, resulting in the dissipation of approximately 26 W of heat to maintain a comparable field gradient. For homogeneity in three directions, three coil pairs are strategically arranged in a close proximity Helmholtz configuration due to space considerations, ensuring a high degree of field uniformity near the atomic cloud (region size of approximately 0.29 mm). This configuration compensates for the external magnetic fields, such as from the Earth or the ion pump. To align the magnetic fields with the formation of the atomic cloud around the center of the cavity, we employ a 3-axis manual translation stage to adjust the position of the coil setup center, ensuring it coincides with the center of the overlapping MOT beams. Positioning the MOT cloud at the center of the NC cavity facilitates the loading of the atoms to the FORT, eliminating

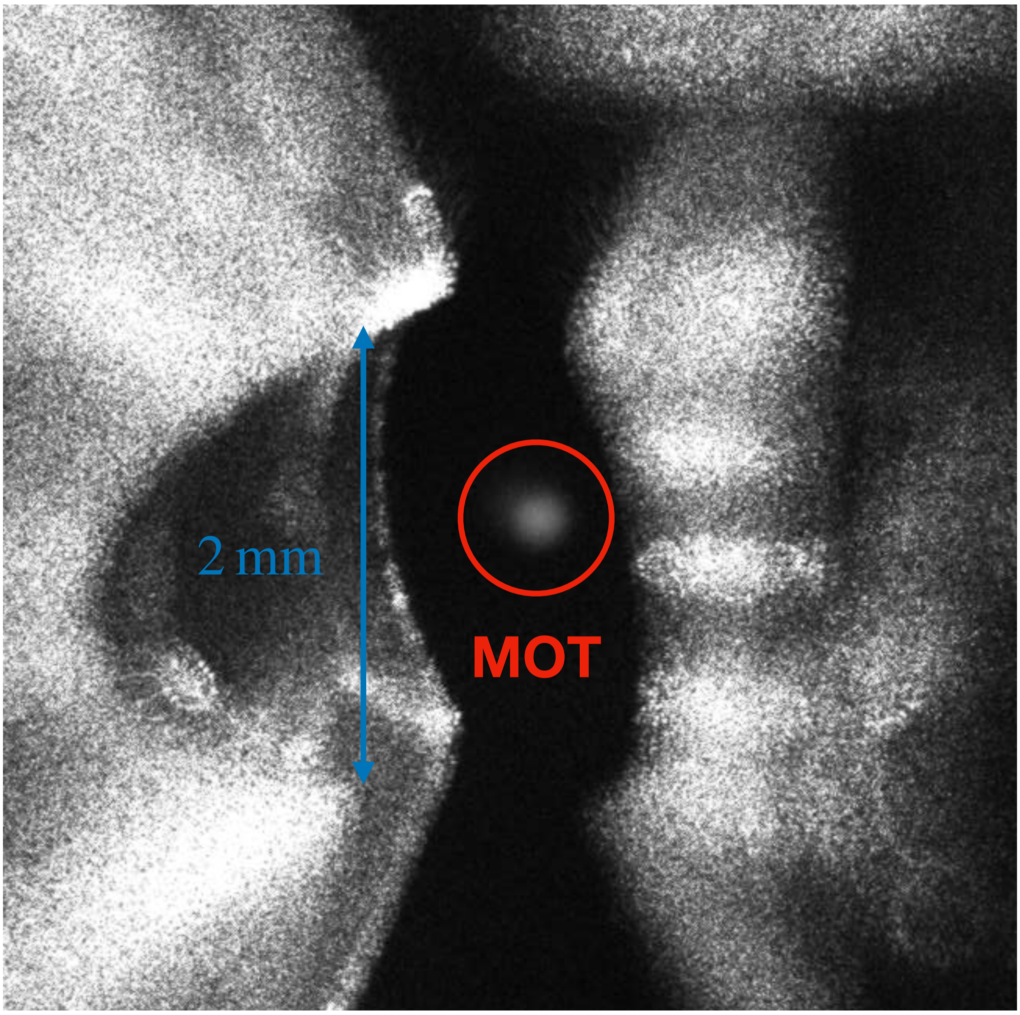

Figure 5.5: A picture of the Rb cloud generated by the MOT for a dispenser current of 2.4 A. The image is taken with a CCD camera, mounted with a biconvex ($f = 30$ mm, B coated) lens to adjust the focus and an iris to control the exposure. The diameter of the cloud is estimated to be 0.29 mm.

the addition of any complex setups for atom delivery to the cavity center.

Observing the formation of the atomic cloud is achieved using a CCD camera, capturing the light scattered by Rubidium atoms from the MOT beams in different directions (see Figure 5.5). To ensure that the feedback on the camera genuinely represents the atomic cloud and not scattering on other elements like mirror shields, we block the cooling beam or the repumper beam one at a time. Blocking the cooling beam will stop straighforwardly stop the cooling process of the MOT and the atoms will not be trapped. Blocking the repumper beam is also sufficient as it disperses the atomic cloud due to Rubidium atoms ending up in the dark state

$5^2S_{1/2}$ $F = 1$. In our system, the Rubidium atomic cloud can be visualised for a dispenser current exceeding 2.4 A, assuming the MOT arms are well aligned and crossing at the center of the magnetic field region. Aligning the MOT arms with the magnetic coils is crucial to observe the atomic cloud, as the number of atoms in the MOT scales with the overlap of the MOT beams to the fourth power [78]. The convenient alignment of MOT arms involves ramping up the dispenser current to observe laser beam fluorescence in the vacuum filled with Rubidium atoms. This provides visual feedback for straightforward alignment. However, achieving laser path visibility in our system would require running the dispenser at a current of over 4 A, posing possible risks to the cavity performance due to linewidth contamination by Rubidium atoms, as no tests were conducted with the NC cavity stage for a dispenser current above 4 A (see Section 3.3.3).

In situations where visually confirming the atomic cloud is challenging due to the overlap of the MOT beams, an alternative method is to load single atoms successfully into the FORT. Loading confirmation is achieved through atomic fluorescence signals at the cavity output, detected by a single-photon avalanche photodiode (APD). Using the atomic fluorescence signal for feedback on MOT performance, we align and optimise the MOT setup to maximise the atomic fluorescence signal, priorly ensuring that all elements of both MOT and FORT setups function correctly. This approach allows us to operate the system near our nominal dispenser current of 2.4 A without the need for high dispenser currents.

5.1.2 The far-off resonant trap (FORT)

Working principle

To trap a specific number of atoms inside our NC cavity, we employ a dipole trap with a frequency far-detuned from the targeted atomic transition. Dipole traps rely on the interaction between the intensity gradient of the laser beam and the atoms, inducing an electric dipole moment in the atoms that creates a potential energy confining them. The induced dipole moment is proportional to the varying electric field of the laser beam and the polarisability of the atoms, resulting in a force experienced by the atoms from the interaction with the laser beam. Basing ourselves on the detailed description of dipole traps given by Grimm et al. [62], the

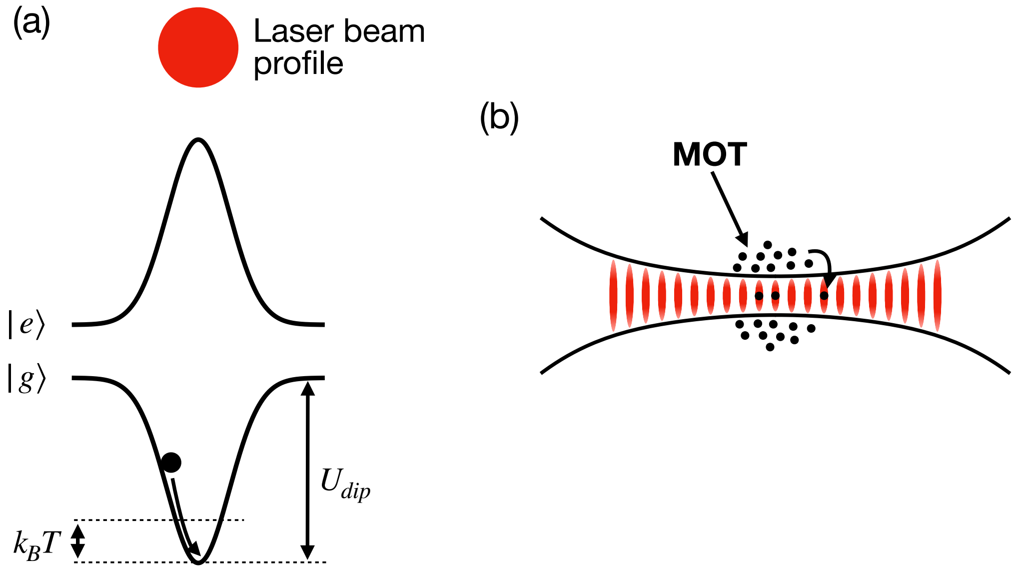

Figure 5.6: (a) The energy level profile of a red-detuned FORT laser. The ground and excited states are both shifted by the same amount of energy. The atom is trapped when its kinetic energy $k_B T$ is inferior to the trapping potential U_{dip}. (b) The FORT laser beam profile forming a standing wave inside the cavity, where atoms are loaded from the MOT to the anti-nodes of the FORT.

trap potential is given as

$$\begin{aligned} U_{dip}(\mathbf{r}) &= -\frac{1}{2}\langle \mathbf{dE} \rangle \\ &= -\frac{1}{2\epsilon_0 c}\mathrm{Re}(\alpha) I(\mathbf{r}), \end{aligned} \tag{5.1}$$

where the brackets reflect the time average of the oscillating electric field $\mathbf{E}$ with the dipole moment $\mathbf{d}$, the factor 1/2 denotes an induced dipole moment rather than a permanent one, and $I(\mathbf{r})$ the location-dependent intensity of the laser beam. α is the atomic polarisability expressed as

$$\alpha = 6\pi\epsilon_0 c^3 \frac{\Gamma/\omega_0^2}{\omega_0^2 - \omega^2 - i(\omega^3/\omega_0^2)\Gamma} \tag{5.2}$$

with $\Gamma = 2\gamma$ the population decay rate, and ω_0 the atomic resonance. While the interaction potential derives from the real part of the polarisability, the imaginary part illustrates the out-of-phase component of the dipole oscillation, represented by the scattering rate

$$\Gamma_{sc}(\mathbf{r}) = \frac{1}{\hbar\epsilon_0 c}\mathrm{Im}(\alpha) I(\mathbf{r}). \tag{5.3}$$

For practical interest, we assume the rotating wave approximation for a two-level system, leading to the trap potential

$$U_{dip}(\mathbf{r}) = \frac{3\pi c^2}{2\omega_0^3}\frac{\Gamma}{\Delta}I(\mathbf{r}), \tag{5.4}$$

where $\Delta = \omega - \omega_0$ the laser detuning from the atomic resonance. In addition, the absorption of the laser beam by the atoms results in scattering of the laser light expressed as

$$\Gamma_{sc}(\mathbf{r}) = \frac{3\pi c^2}{2\hbar\omega_0^3}\frac{\Gamma^2}{\Delta^2}I(\mathbf{r}). \tag{5.5}$$

Note that for scenarios with large detuning Δ, the dipole potential and scattering rate scale as $I(\mathbf{r})/\Delta$ and $I(\mathbf{r})/\Delta^2$ respectively, favorising the use of large detuning and high intensity to keep the scattering rate minimal. Red-detuned ($\Delta < 0$) and blue-detuned ($\Delta > 0$) traps are distinguished by the detuning sign, influencing the direction of the dipole force.

For efficient dipole trap characterisation, we express Equations 5.4 and 5.5 in terms of the cavity finesse $\mathcal{F}$ and transmitted power P_t. The trap depth of the dipole trap U_0 is obtained for $I(\mathbf{r}) = I_{max}$, where I_{max} is the maximum intensity stored in the cavity mode, expressed in terms of the stored power inside the cavity P_{inside}

$$I_{max} = \frac{4P_{inside}}{\pi w_0^2}, \tag{5.6}$$

where w_0 is the cavity waist, and the factor four accounts for the amplitude of the electric field at the anti-nodes of the cavity standing wave. From thereon, P_{inside} can be related to the transmitted power through the resonator P_t [56]

$$P_{inside} = \frac{\mathcal{F}}{\pi}P_t. \tag{5.7}$$

Substituting I_{max} into Equations 5.4 and 5.5 results in

$$U_0 = \frac{6c^2}{\pi\omega_0^3}\frac{\Gamma}{\Delta}\frac{\mathcal{F}}{w_0^2}P_t \tag{5.8}$$

and

$$\Gamma_{sc} = \frac{6c^2}{\pi\hbar\omega_0^3}\frac{\Gamma^2}{\Delta^2}\frac{\mathcal{F}}{w_0^2}P_t. \tag{5.9}$$

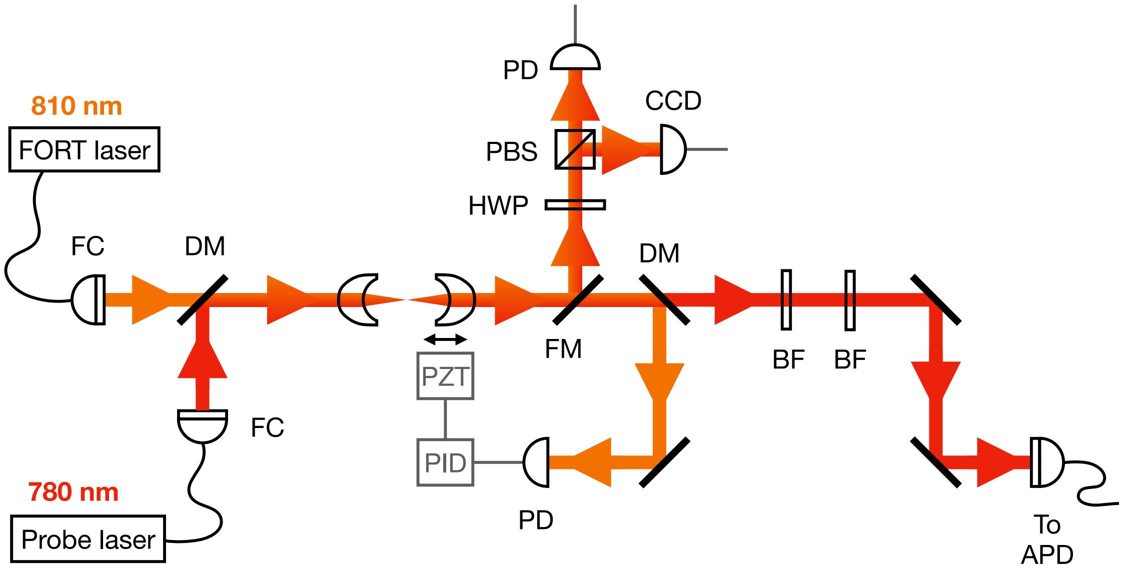

Figure 5.7: The schematic of the far-off resonant trap (FORT) setup. For pre-alignment, the probe laser is used, and the cavity feedback is observed through a CCD camera and a photo-diode (PD). The FORT laser, also acting as the locking laser, is then coupled to the same fundamental spatial mode of the cavity as the probe laser. Both laser are collimated and superposed/separated using dichroic mirrors (DM). Once the alignment is done, the flip mirror (FM) is put down and the cavity error signal is obtained through the FORT laser, locking the cavity to that laser. The probe laser output from the cavity passes through two bandpass filters (BF, Thorlabs NExA-B) centered at 780 nm before going to the single photon avalanche photodiode (APD) through a fiber. The probe laser path helps to visualise the cavity mode output to efficiently collect the light emitted by the atoms at the single photon level. When looking for the atomic fluorescence, the probe laser is turned off.

FORT setup

The FORT laser serves a dual purpose: it locks the cavity length (refer to Section 4.3.1) and traps atoms. Consequently, the FORT operates within a fundamental cavity mode, with a far-off resonant frequency from the targeted atomic transition, located at 810 nm. As the FORT beam establishes a standing wave inside the NC cavity, atoms can only be trapped at the local intensity maxima (anti-nodes) of this standing wave, where $I(\mathbf{r}) = I_{max}$ (see Figure 5.6). This results in trapping sites separated by a distance of $\lambda/2$ along the cavity axis, limited by the cavity mode waist in the transverse direction. With our small cavity mode waist of $w_0 = 2.8\,\mu\text{m}$ at

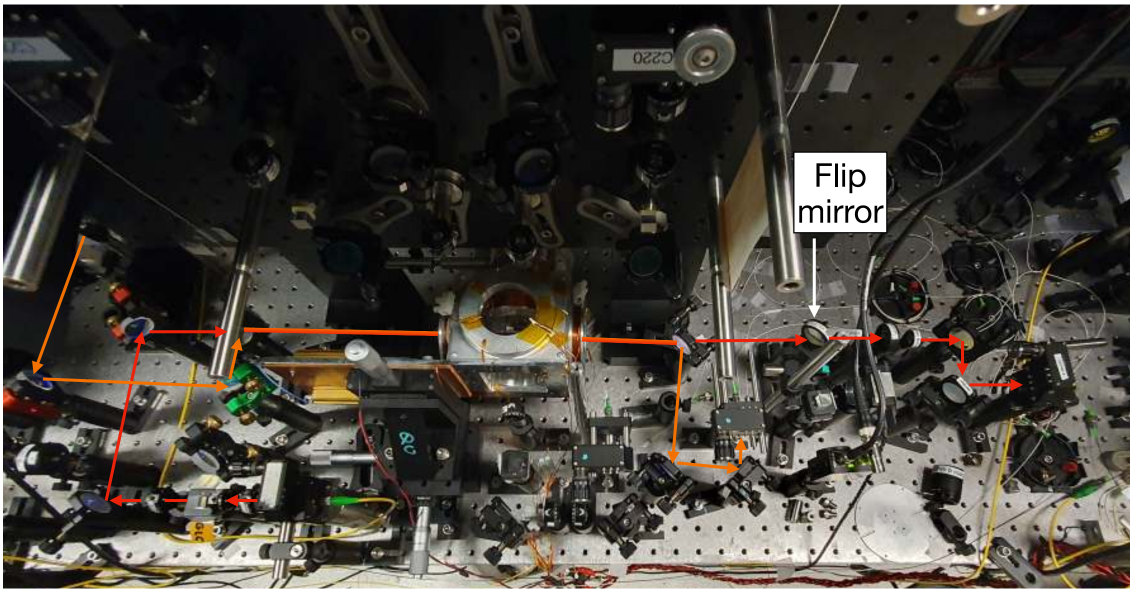

Figure 5.8: The optics of the FORT setup as per Figure 5.7. The red trajectory represents the probe laser's route, while the orange path illustrates the FORT laser's trajectory.

the last stable point before concentricity, we operate in the light-assisted collisional blockade regime [79], allowing our dipole trap to accommodate an average of 0.5 trapped atoms per site. An estimate of the number of sites is given by

$$n_{sites} \approx \left[\frac{4\pi w_0^2}{\lambda_{810}^2}\right], \tag{5.10}$$

where the the square brackets indicate the nearest integer function. For our cavity mode waist, this corresponds to about 150 trapping sites. The loading into these sites is probabilistic from the MOT reservoir, and each site can accommodate no atom or a single atom. As multiple atoms can be trapped at different sites simultaneously, the total number of atoms trapped can be identified from the atomic fluorescence signal (see Section 5.1.3).

To ensure the alignment of the cavity lock with the maximum transmission at the targeted atomic transition, the linearly polarised 810 nm FORT beam is combined through a dichroic mirror with the 780 nm probe beam resonant to the main atomic transition, used for pre-alignment of the cavity (see Figure 5.7 and 5.8). Subsequently, both lasers are aligned to the same cavity fundamental mode and, using the transfer cavity setup (see Section 4.3.1), the cavity length is locked such that both the probe and FORT beams possess the maximum transmission through the cavity. After the cavity transmission, both beams are decoupled using a dichroic mirror. At the FORT laser frequency of 810 nm, the finesse is measured to be $\mathcal{F} = 100$ for a cavity mode-matching efficiency of 22 %. Based on the cavity input of $P_{\text{in}} = 2.6\,\text{mW}$ and output power $P_{\text{out}} = 100\,\mu\text{W}$ of the FORT beam, the trap depth is estimated to be around 27 MHz and the scattering rate is around $11\,\text{s}^{-1}$.

Note that the dipole interaction induced by the FORT beam creates an AC Stark shift within the atoms energy levels. This shift modifies the atomic resonance by an amount proportional to the atom–cavity coupling strength g and the incoming power of the FORT beam, making the atoms nonresonant with the exact targeted D_2 line of ^{87}Rb. To palliate this problem, the cavity length is slightly adjusted to match the new atomic resonance. However, due to the use of the atomic fluorescence to detect atom loading in the FORT in our measurement sequence (see Section 5.2.1) and the strong coupling strength g exhibited by our system, the cavity length change between the resonant D_2 line and the modified atomic resonance by the AC Stark shift cannot be performed fast enough in an adiabatic way without losing the cavity lock. Therefore, we mainly rely on tuning the FORT beam power by decreasing it by a factor of 5 during the probing of the atoms, ensuring that the cavity error signal remains resolvable and the lock persists, while atom loading still occurs.

5.1.3 Detection of trapped atoms

The atom–cavity photon interaction is examined in the single-photon regime. When illuminated by the red detuned cooling MOT beams, atoms loaded in the FORT sites scatter photons into the cavity mode, proportionally to the coupling strength g. To detect these scattered photons, we employ a silicon APD (custom-built) with an efficiency of approximately 45-50 % at 780 nm. The signals from photo-events are captured by a timestamp unit (custom-built), which provides either a list of photo-event times or the photon counts associated to a specific time frame.

To initiate an experimental sequence, we observe the atomic fluorescence and use the photo-detection count as a trigger. An abrupt increase in the number of photo-detection counts indicates the loading of one or more atoms in the trap, while an abrupt decrease indicates the escape of the atoms from the trap (see

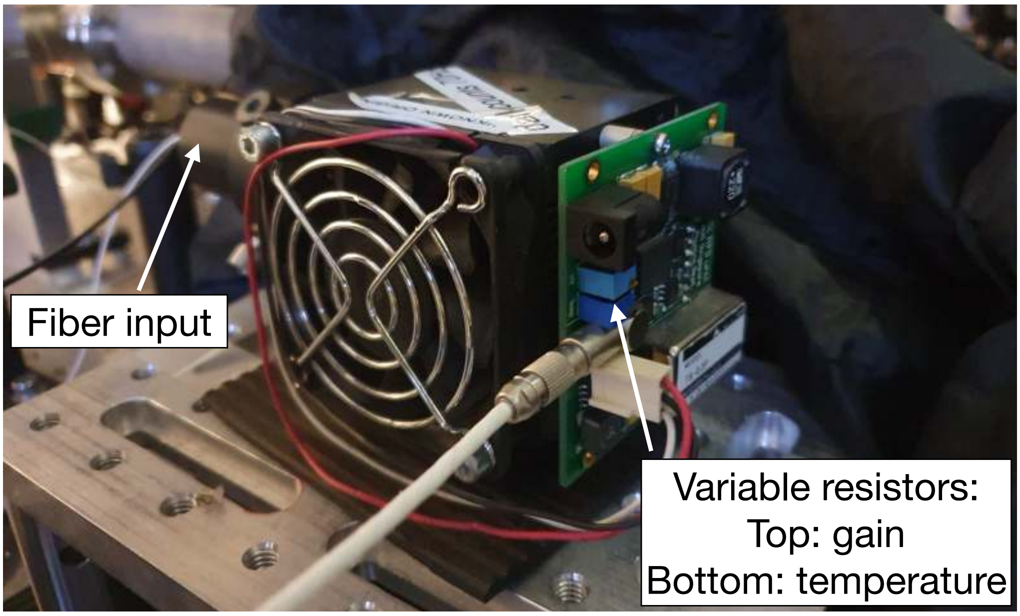

Figure 5.9: A homemade single photon avalanche photo-detector (APD), based on a silicon photodiode (Perkin Elmer C30902S). The APD is calibrated using a reference source. The gain and the temperature of the APD, both related to a voltage, can varied to minimise dark counts by adjusting the two variable resistors. When in use, the APD is covered by a blackout nylon fabric (Thorlabs BK5).

Figure 5.10). The background is mainly due to the scattering into the cavity mode of the MOT beams on the cavity mirrors' shields. The loading rate is influenced by the MOT parameters, namely its density, location, and temperature. The loading rate varies typically between 0.1 and 5 events per second. If the photodetection count rate surpasses a predefined threshold, indicating an atom loading event, the experimental sequence (see Figure 5.12) is executed through a digital pattern generator (custom-built). The predefined threshold is selected to clearly distinguish loading events from the background. It is set low enough to detect loadings with minimal fluorescence counts while maintaining clear differentiation from the background noise to maximise the number of events. The data gathered during the experimental sequence is subsequently grouped into bins of a specific size to generate the fluorescence signal traces, using C and Python programs. Once the traces are obtained, post-selection is performed to retain only those traces with the desired fluorescence level, corresponding to a specific number of atoms.

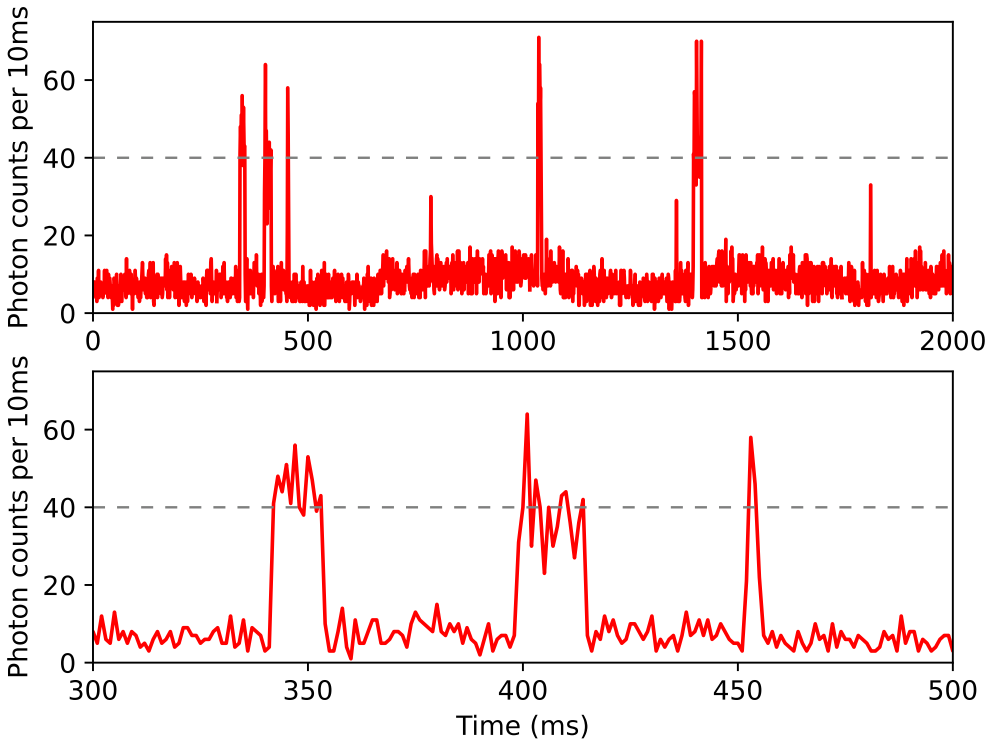

Figure 5.10: A standard atomic fluorescence signal trace organised in 10 ms bins. The bottom trace is a closer view from the previous plot. The dashed lines shows the atomic fluorescence threshold at which the measurement sequence is triggered, and corresponds to approximately 4 counts/ms. The bottom graph displays three events trapping a single atom each. A clear two atom trapping signal can be seen in the predecessor's work [58].

Post-selection criteria

As a drop in atomic fluorescence from one level to another signifies atomic de-excitation, and therefore atom loss, it is therefore possible to characterise the number of atoms trapped in the FORT by looking at the atomic fluorescence trace. Once the trigger threshold is surpassed, it indicates the trapping of one or more atoms inside the trap (see Figure 5.10). The count of fluorescence level jumps until reaching the background quantifies the number of atoms held in the FORT, one drop in fluorescence indicating an atom loss until the background level is reached. Therefore, it is possible to associate a number of atoms to each fluorescence levels. By post-selecting on a fluorescence level associated to a number of atoms trapped in the FORT, we can extract various statistics associated with a specific atom number, such as the atom lifetime and the coupling strength of the atom–cavity system later

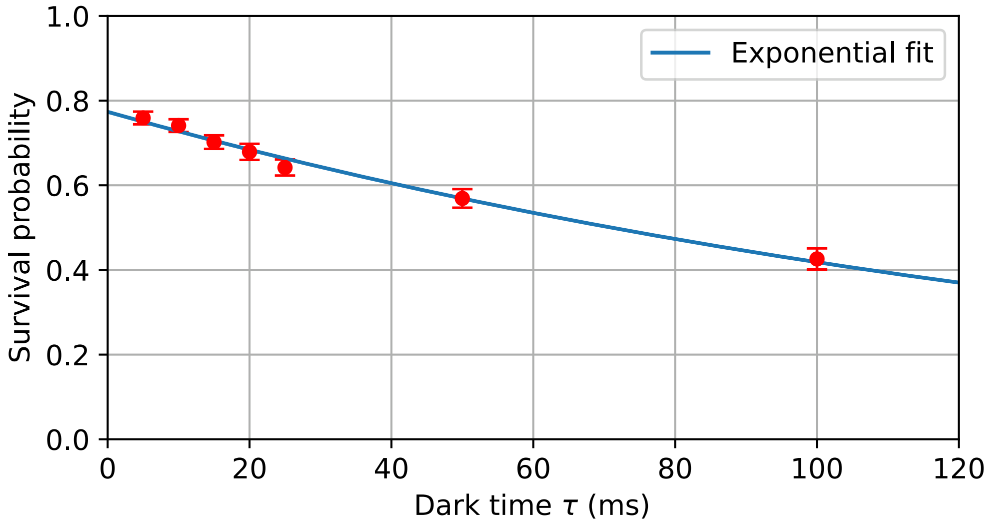

Figure 5.11: The lifetime of trapped atoms in the FORT while the MOT beams are switched off for a dark time τ. The atoms in the FORT exhibit an exponential decay in survival probabilities, characterised by a decay time of 162.7(5) ms and a y-intercept at 0.77(3) %. Binomial statistic is used to determined the error bars.

on (see Section 5.2.3).

Atom lifetime

Once the atoms are loaded in FORT, the MOT cooling and repumper lasers are switched off using the AOMs to disperse the MOT. We then wait for a dark time τ before turning the MOT cooling and repumper lasers back on to check the presence of atoms in the trap through atomic fluorescence. Figure 5.11 shows the survival probability for different dark times. By fitting the data to an exponential curve, we obtain an atomic decay time of 162.7(5) ms for single atoms trapped in the FORT. This short lifetime results from challenges in aligning the MOT beams, as visual feedback is only obtained when the MOT beams are well aligned with each other. Despite the faint formed MOT, the loading rate into the dipole trap is adequate for observing vacuum Rabi splitting, our primary objective. For future experiments including logic gates, lifetime optimisation will be conducted.

5.2 Observing the atom–cavity interaction

In the presence of one or more atoms trapped in the cavity, the cavity transmission $T_{ac}(\omega)$ and reflection $R_{ac}(\omega)$ spectra are modified due to the atom–cavity coupling strength g. The modified spectra, when probed by a weak coherent beam, are given by [26]

$$T_{ac}(\omega) = \left| \frac{\kappa_{out}(i\Delta_a + \gamma)}{(i\Delta_c + \kappa)(i\Delta_a + \gamma) + g^2} \right|^2, \tag{5.11}$$

and

$$R_{ac}(\omega) = \left| 1 - \frac{\kappa_{out}(i\Delta_a + \gamma)}{(i\Delta_c + \kappa)(i\Delta_a + \gamma) + g^2} \right|^2, \tag{5.12}$$

where $\Delta_c = \omega - \omega_c$ and $\Delta_a = \omega - \omega_a$ are the detunings with respect to the cavity and atomic frequencies, respectively. These two spectra assume perfect spatial mode-matching to the cavity, which is not the case in experimental settings. Adding the mode-matching efficiency η results in

$$T_{ac}^{exp}(\omega) = \eta T_{ac}(\omega), \tag{5.13}$$

and

$$R_{ac}^{exp}(\omega) = (1 - \eta) + \eta R_{ac}(\omega). \tag{5.14}$$

To probe this atom–cavity interaction and obtain its response signal, we need to send a weak coherent laser beam while the atoms are loaded in the FORT and the MOT beams are off to avoid additional scattering that would disperse the trapped atoms. To do so, a measurement sequence is established to acquire the data through the single-photon APD, under certain conditions.

The first prerequisite consists of aligning the NC cavity in its fundamental LG_{00} mode resonant to the targeted atomic transition, at a pre-selected critical distance d, and activating the longitudinal and transverse locks to stabilise the cavity length (see Section 4.3). Once the locks are established, the MOT lasers are turned on and observation of atom loading into the FORT is confirmed by looking at the atomic fluorescence. In addition, the appropriate triggering threshold is selected, depending on the atomic fluorescence level. In the case where the loading rate is not satisfactory, the MOT and FORT are re-optimised until the loading rate is sufficient. We then proceed with the measurement sequence.

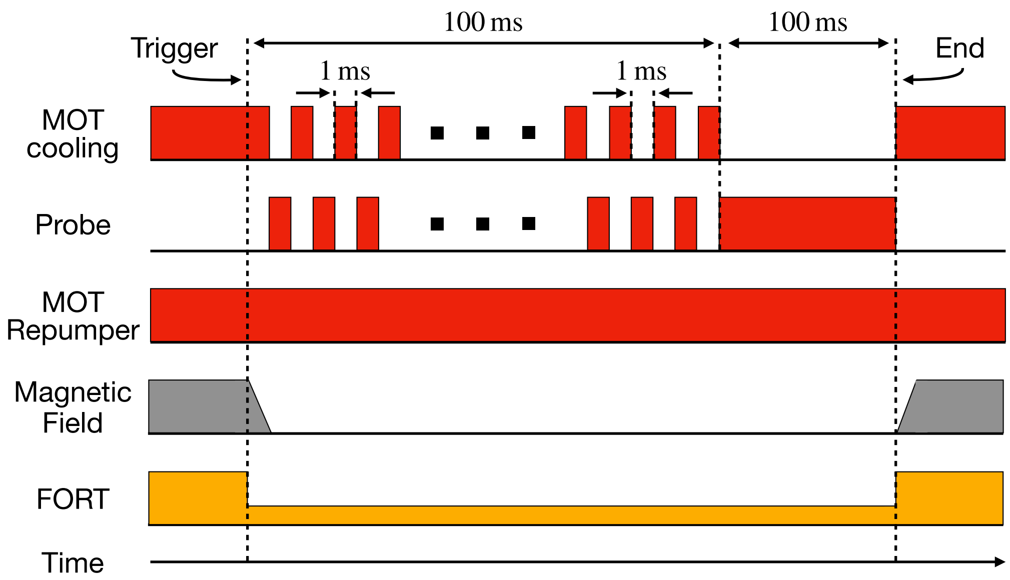

Figure 5.12: The schematic of the measurement sequence. The sequence starts when the monitored atomic fluorescence goes above the set threshold, indicating loading of one or more atoms in the FORT. Once triggered, the magnetic field is switched off. The MOT cooling laser and probe laser are then alternated 50 times over 100 ms, each being on for 1 ms at a time. The purpose of this oscillation is to probe the atomic fluorescence using the MOT cooling laser, as well as adding layers of repetitive cooling to prevent rapid heating of the atoms from the probing laser and hence run longer measurements. By the end of the first 100 ms, all atoms are expelled from the trap due to heating from the probe beam. After probing the atoms, the transmission of the empty cavity is further examined using the probing laser for an additional 100 ms. Since the MOT repumper laser operates at a frequency distinct from the targeted atomic transition, it remains active throughout the entire measurement. At the end of the complete 200 ms sequence, the probe laser is deactivated. The magnetic field and MOT cooling beams are reactivated to observe the atomic fluorescence once more and await a new triggering signal.

Note that if the NC cavity goes out of lock, the data acquisition is halted, the acquired data is discarded, and the system configuration is re-initiated from the LG_{00} mode alignment.

5.2.1 The measurement sequence

As the atom–cavity interaction can only be observed when the weak coherent probe beam is sent and the MOT beams are off, the measurement sequence aims to control the different lasers in use as well as the data acquisition. To easily control the turning on/off of the beams, all lasers involved go through AOMs, acting as

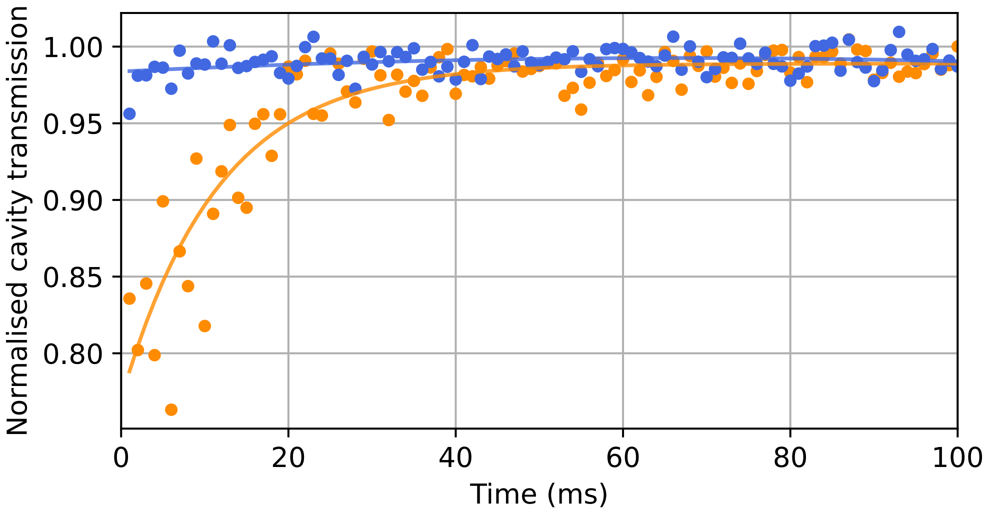

Figure 5.13: The average cavity transmission at the atomic and cavity resonances ($\omega = \omega_a = \omega_c$). The solid lines represent the fits of the data points. The blue line indicates the empty cavity transmission, while the orange line shows the expected modified transmission in the presence of atoms. Despite displaying the expected response when atoms are loaded in the cavity, the shift in cavity transmission depicted by the orange line is, in fact, due to the displacement induced by the springs response to the magnetic field switch.

switches. Additionally, a few neutral density filters (Thorlabs NE60 and NE40) are added to the probe laser path using flip mounts to conveniently adjust its laser power and create a weak coherent beam. We employ a computer-assisted script to centralise control over the various AOMs, photo-detectors, and essential devices. The measurement sequence, depicted in Figure 5.12, sends signals to these devices, and the recorded data, including photo-detection counts from the APD, is stored using a timestamp card. The data stored by the timestamp card records each count associated to a device channel and its arrival time. To extract this information, the data is processed, using C and Python scripts, into timebins and histogrammed to recover the photo-detection counts necessary for atomic fluorescence categorisation.

5.2.2 Resonant probing and impact of the magnetic field

Upon trapping one or more atoms within the cavity, aligning their resonant frequencies ω_a with ω_c, a portion of the weak coherent light directed to the cavity mode gets absorbed by the atom, inducing a modification in the cavity transmis-

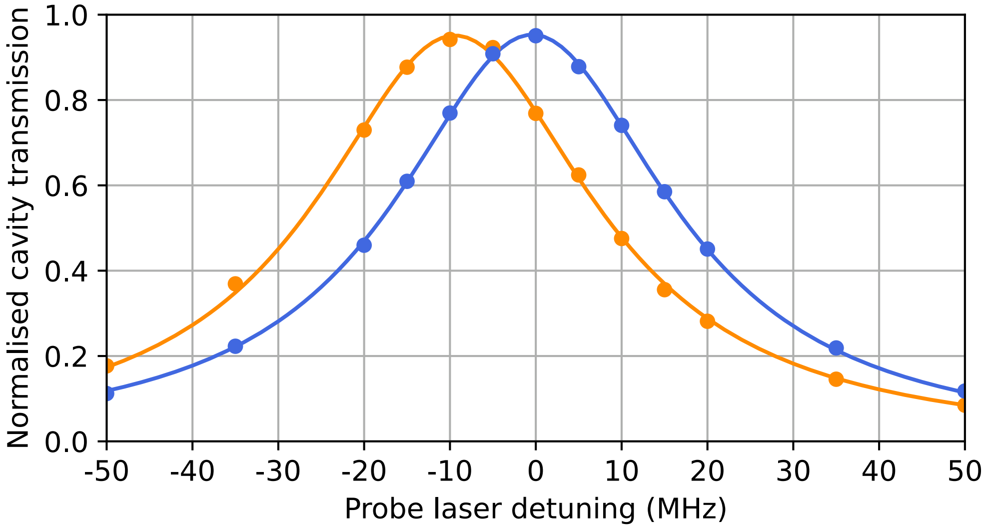

Figure 5.14: The induced shift in cavity transmission from the springs response to the magnetic field switch. The solid lines are fits to Lorentzian functions. The magnitude of the frequency shift of the cavity resonance is proportional to the speed at which the magnetic field is turned off.

sion. This alteration results in reduced photo-detection counts when probing the cavity transmission with an atom, compared to an empty cavity transmission. The maximum extinction occurs when $\Delta_{a,(c)} = \omega - \omega_{a,(c)} = 0$ and diminishes when the probe laser is detuned from the targeted atomic transition. Figure 5.13 illustrates this effect for $\Delta_{a,(c)} = 0$, based on measurements from several loading events.

However, in our case when combining the different extinction ratio with respect to the frequency detuning of the probe laser, we simply observe a shift in the cavity transmission (refer to Figure 5.14). This shift is attributed to the ferromagnetic properties of the springs used in the cavity structure (see Section 3.3). When toggling the magnetic field on and off during the measurement sequence, the springs get impacted due to their ferromagnetic nature and exhibit a slight structure misalignment, corrected by our locking mechanisms in the long term. The reason for the springs becoming ferromagnetic, despite being made of stainless steel SUS304 (known for being austenitic), comes from the manufacturing process of the springs. Austenitic stainless steel can undergo a deformation-induced transformation from a face-centered cubic crystal structure (austenitic) to a body-centered cubic crystal structure (martensitic) when subjected to plastic deformation [80, 81]. This

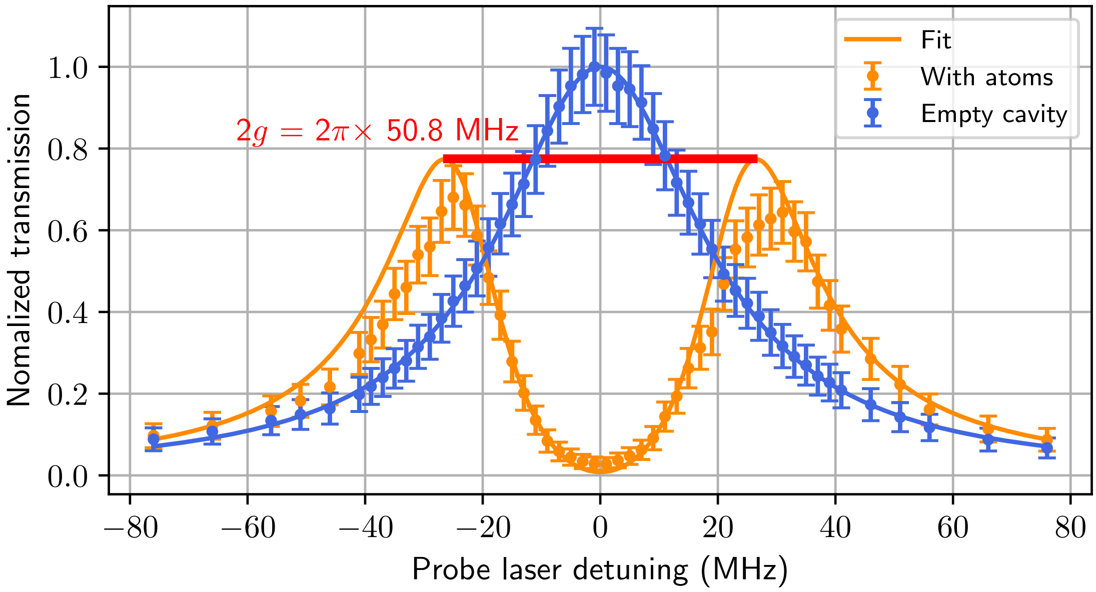

Figure 5.15: The cavity transmission spectrum with 10 atoms (orange) and without atoms (blue) trapped in the cavity at a critical distance $d = 1.42(5)\,\mu\mathrm{m}$. The respective fits are shown by the solid lines. The vacuum Rabi splitting is characterised by the presence of atoms in the cavity, which display a split with respect to the atomic resonance, each peak being separated from the atomic resonance by the coupling strength of $g_{10} = 2\pi \times 25.4(4)\,\mathrm{MHz}$.

microstructural transformation results in a high rate of strain hardening on the macroscale, rendering the material ferromagnetic.

An easy solution to avoid the cavity shift problem is to keep the magnetic field on at all times. While this does not pose an issue for probing the atom–cavity interaction, it becomes problematic when attempting state preparation of the atoms with Zeeman sublevels, requiring the addition of a magnetic field (see Section 5.2.4).

5.2.3 Vacuum Rabi splitting

Conducting the measurement sequence without the magnetic field artefact and aligning the cavity at a critical distance of $d = 1.42(5)\,\mu\mathrm{m}$, followed by post-selection on a fluorescence level associated to 10 atoms (see Section 5.1.3), yields the transmission spectra depicted in Figure 5.15. The choice of the critical distance $d = 1.42(5)\,\mu\mathrm{m}$ is arbitrary and solely relied on the ease of overlapping of the lock

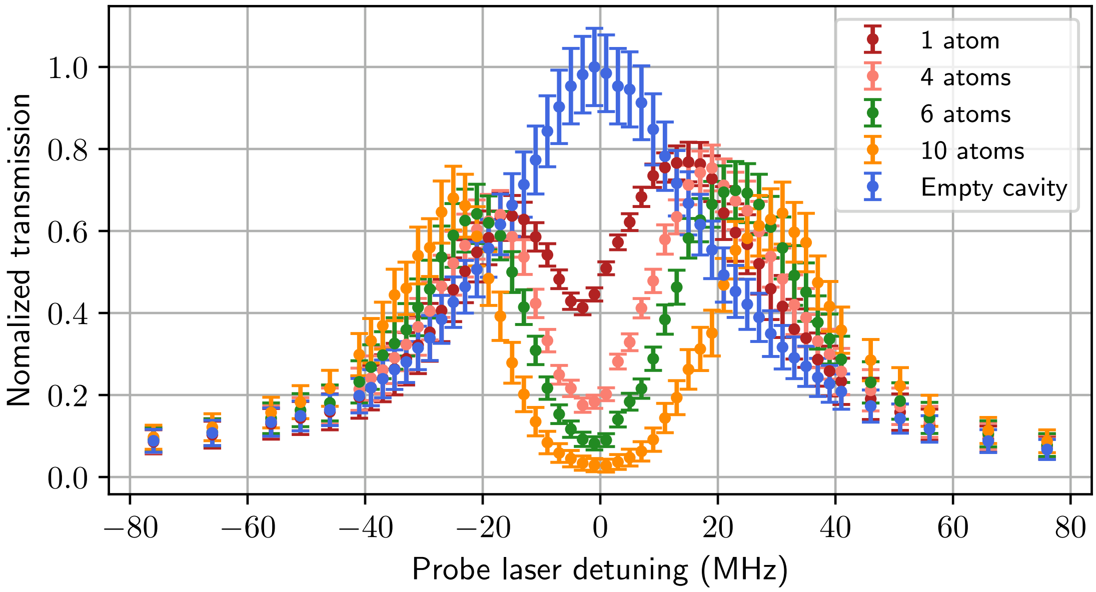

Figure 5.16: The vacuum Rabi splitting for various post selected atom numbers at a critical distance $d = 1.42(5)\,\mu\text{m}$. Additionally, the slight disagreement between the fit and the data is due to inhomogeneous broadening of the atomic transition frequency.

laser transmission with the probe laser transmission through the cavity on the day of the measurements. This distance corresponds to one FSR away from the critical distance $d = 1.06(5)\,\mu\text{m}$, where the noise measurements took place. Moreover, as this measurement primarily illustrates the system's operation within the strong coupling regime (see Section 2.1.3) rather than directly demonstrating quantum logic gates computation, a shift by one FSR away from concentricity in the critical distance only further highlights the system's capability to operate in the strong coupling regime and showcase high cooperativity. This is because the larger the critical distance, the smaller the atom–cavity coupling strength g will be (see Figure 3.2).

Each data point in Figure 5.15 corresponds to around 100 atom events. The transmission spectrum with trapped atoms is fitted to Equation 5.11, while the empty cavity spectrum is fitted to a Lorentzian profile. The fitting of the cavity transmission spectrum reveals an atom–cavity coupling strength of $g_{10} = 2\pi \times 25.4(4)\,\text{MHz}$ and a cavity linewidth $2\kappa = 2\pi \times 42(2)\,\text{MHz}$, resulting in a cooperativity of $C = 5.1(5)$ for our atomic decay rate $\gamma = 2\pi \times 3.03\,\text{MHz}$. Note that since $g > \kappa$, the atom–cavity

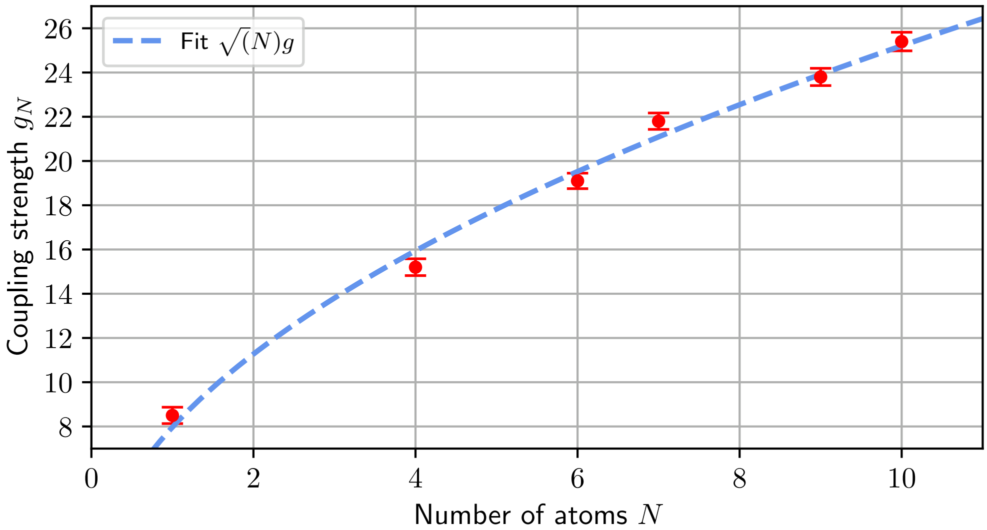

Figure 5.17: The coupling strength g_N from the several vacuum Rabi splitting observed for different atom numbers. The data is fitted to $\sqrt{N}g$, where the fitted value of $g = 2\pi \times 8.0(1)$ MHz.

system is indeed in the strong coupling regime (see Section 2.1.3).

The vacuum Rabi splitting is obtained for various atom numbers confined within the cavity, as shown in Figure 5.16. Analysing the measured coupling strength g_N allows for the extraction of the single atom coupling strength g through the relation $g = g_N/\sqrt{N}$. The fitted values of g_N are presented in Figure 5.17, yielding a determined value of $g = 2\pi \times 8.0(1)$ MHz. The fitted g value is expectedly lower than the theoretical $g_{th} = 2\pi \times 12.5$ MHz due to the inherent random spin polarisation of the prepared atoms and the use of linearly polarised light for probing. The anticipated maximum coupling strength for a single atom at a critical distance $d = 1.42(5)$ µm is $g_{max} = g_{th}/\sqrt{2} = 2\pi \times 8.8$ MHz, accounting for Clebsch-Gordan coefficient averaging. The 10 % reduction from this maximum value can be explained by the fact that some trapping sites in the FORT standing wave might not perfectly coincide with the probe beam standing wave. While this point can be calculated, the absence of visual feedback for our MOT complicates the estimation, as the loading probability of atoms into the dipole beam depends on the location and radius of the MOT relative to the nodes of the dipole beam.

In addition, upon assessment, the cavity linewidth emerges as the most influential parameter to increase cooperativity. However, the measured linewidth surpasses the theoretical prediction by more than a factor of two, suggesting a plausible contamination of the initial coating. This could stem from mirror handling during the assembly of the NC cavity system or possible contamination during vacuum use, as discussed in Section 3.3.3.

5.2.4 Discussion on the characterisation of the atom–cavity induced phase shift and a controlled phase gate

To further characterise the quantum information processing capability of our atom–cavity system, a fundamental component is the controlled phase gate [82, 83, 84]. The key idea behind the controlled phase gate is to leverage the interaction between our quantum system (in our case Rubidium atoms) and the NC cavity to induce a controlled phase shift on the outgoing photons. In an optical cavity setting, the phase shift is manifested when the system is operated in the strong coupling regime and the atom is uncoupled to the cavity mode. Photons can then enter the cavity and experience a π phase shift in the ideal case. However, if the atom is coupled to the cavity mode, photons are reflected without any phase shift due to vacuum Rabi splitting. When multiple atoms are trapped within a cavity, we can extend the approach of the Tavis-Cummings model [51], N atoms trapped within a cavity are treated as a 'superatom'. This extension is applicable to a phase gate, provided that the saturation condition for N trapped atoms is met. This condition ensures the observation of vacuum Rabi splitting, resulting in an induced phase shift in the system.

Following the framework outlined by Reiserer et al. [83], the induced phase shift is commonly controlled via the coherent state of the atom, serving as the control qubit in the system, which can either be resonant $|\uparrow^a\rangle$ or non-resonant $|\downarrow^a\rangle$ with the cavity mode. The other qubit is typically encoded in the polarisation of the photon, such that $|\uparrow^p\rangle$ represents the right circular polarisation and $|\downarrow^p\rangle$ the left circular polarisation of the light. By controlling the state of the atom to be resonant to the cavity or in a dark state and selecting a polarisation dependent atomic transition, the phase shift becomes conditional on the quantum state of the interacting system. For a right circularly polarised transition, where the left circularly polarised transition

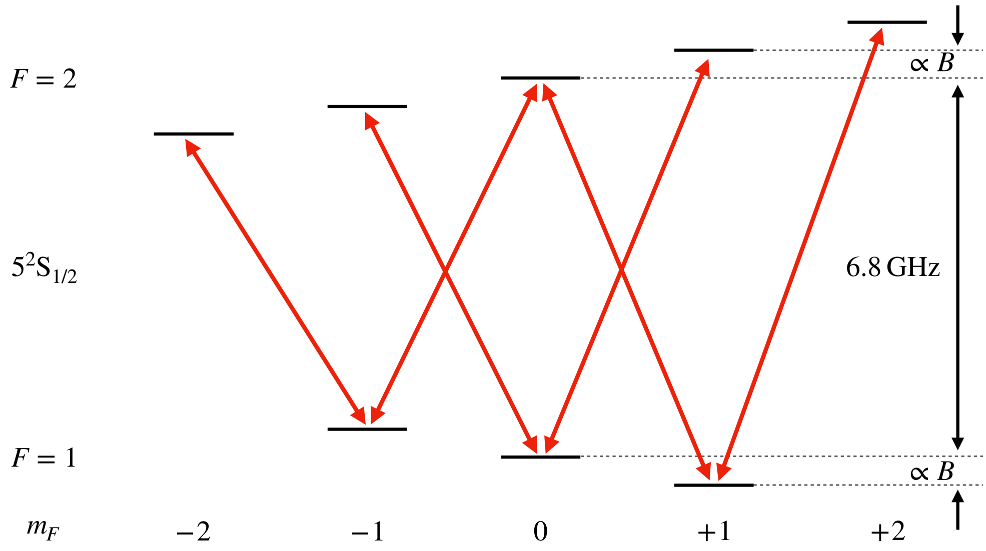

Figure 5.18: The energy diagram of ^{87}Rb showcasing the ground states generated through Zeeman splitting. The red lines indicates the driveable microwave transitions between these states. The sublevels frequency difference lies in the radio frequency range, with additional detuning depending on the magnitude of the magnetic field.

is forbidden, the truth table of the system is as follows

$$\begin{aligned} |\uparrow^a\uparrow^p\rangle &\rightarrow |\uparrow^a\uparrow^p\rangle, \\ |\uparrow^a\downarrow^p\rangle &\rightarrow -|\uparrow^a\downarrow^p\rangle, \\ |\downarrow^a\uparrow^p\rangle &\rightarrow -|\downarrow^a\uparrow^p\rangle, \\ |\downarrow^a\downarrow^p\rangle &\rightarrow -|\downarrow^a\downarrow^p\rangle. \end{aligned} \tag{5.15}$$

In the instance of a left circularly polarised atomic transition allowed, the state $|\uparrow^a\downarrow^p\rangle$ would remain unaltered. The quantification of such controlled phase shift is important to understand the efficiency, coherence, and fidelity of the quantum operations within our system.

To achieve control over a coherent state with ^{87}Rb, a commonly employed strategy involves utilising two Zeeman sublevels of the atomic ground state hyperfine levels $5S_{1/2}\ F = 1$ and $5S_{1/2}\ F = 2$, with one resonating with the cavity $|\uparrow^a\rangle$ and the other acting as a dark state $|\downarrow^a\rangle$ [85, 83]. Initially, the hyperfine levels $5S_{1/2}\ F = 1$ and $5S_{1/2}\ F = 2$ are chosen through optical pumping techniques [65, 86]. Optical pumping involves selectively populating a particular hyperfine level using polarised laser light to align the atoms to the desired state. The selected

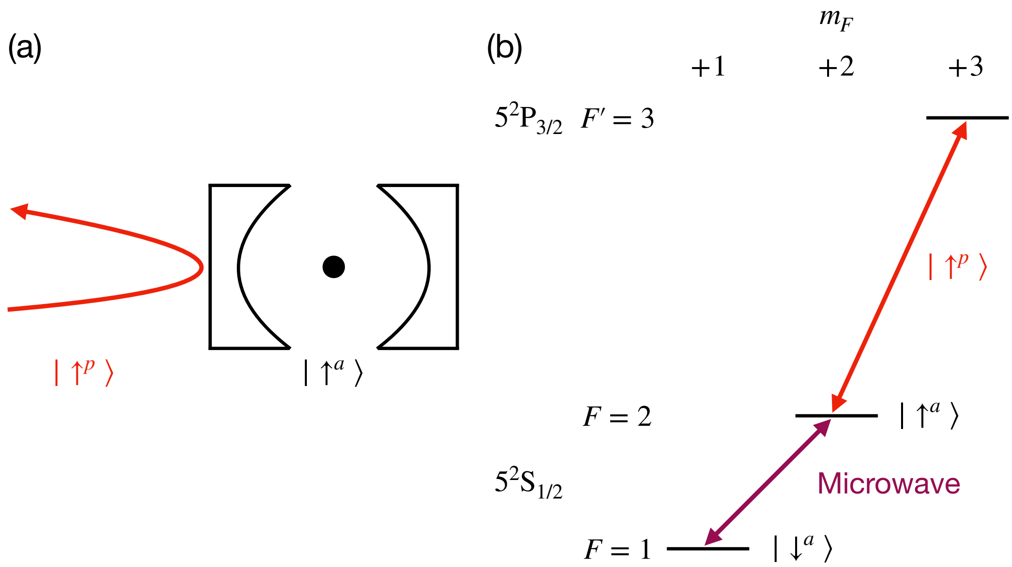

Figure 5.19: The schematic of specific driven Zeeman sublevels for a control phase gate mechanism. (a) When the atom is coupled to the cavity mode in the state $|\uparrow^a\rangle$, the incoming polarised light $|\uparrow^p\rangle$ is reflected of the cavity, not experiencing any phase shift. (b) Energy diagram of the atomic states in use for an allowed right circularly polarised light. To use a left circularly polarised light as the allowed transition, the necessary m_F levels need to be changed to their negative counterparts.

hyperfine levels are then subjected to Zeeman splitting under the influence of an added magnetic field. In the case of our system, the additional magnetic field would be implemented by modifying the current in the two compensation coils along the cavity axis. This splitting results in multiple Zeeman sublevels within each hyperfine state (see Figure 5.18). Once the Zeeman sublevels are established, the next step involves creating superposition between two specific Zeeman sublevels within the selected hyperfine state. This is achieved by introducing radio frequency (RF) fields. The frequency of the RF field is tuned precisely to match the energy difference between the chosen sublevels, enabling coherent transitions. Consequently, the atomic state can be efficiently controlled to be either coupled or uncoupled to the cavity and the incoming polarised photon (see Figure 5.19). The incoming polarised photon is made resonant with an atomic transition that only couples to either right or left circular polarised light. In doing so, it ensure that only one atom–photon state remains unchanged, while the others experience a phase shift.

However, due to the sensitivity of our cavity structure to changes in the magnetic

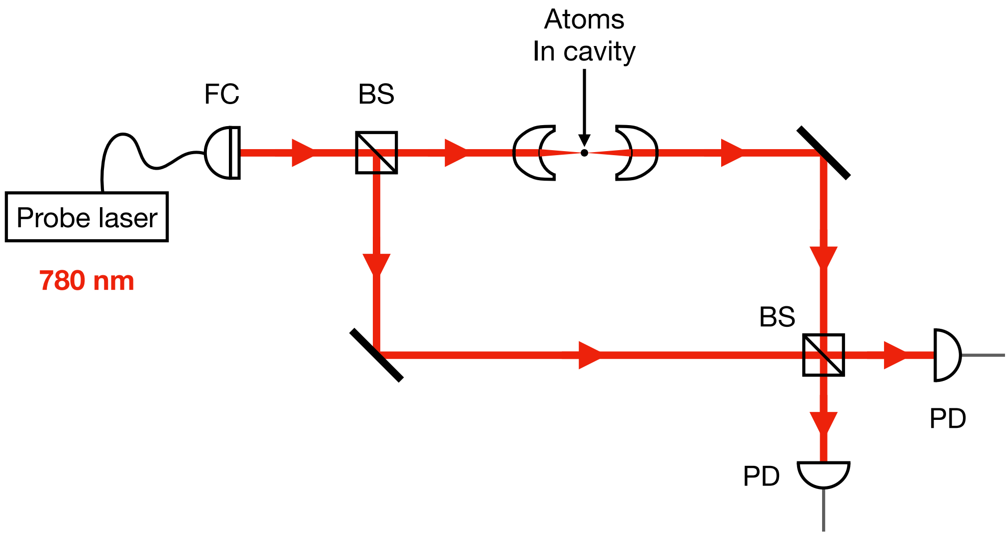

Figure 5.20: The schematic of a Mach-Zehnder interferometer with the atom–cavity system in one of the arms. In the presence of atoms in the cavity, the phase along the arm would be modified, resulting in an interference pattern at the second beam splitter. Characterisation of the fringes will indicate the amount of phase shift.

field, implementing coherent states utilising Zeeman sublevels is not feasible in the current design. An alternative solution would involve reconstructing the cavity with non-ferromagnetic springs. Nevertheless, this option presents significant time challenges, necessitating a complete restart at each stage:

1. Crafting new frames for the cavity mirrors, cleaning them, and assembling the entire NC cavity, considering the curing time of the various parts discussed in this thesis.

2. Reopening the vacuum system to place the NC cavity and then re-baking the system for several weeks to achieve UHV, all while ensuring precise alignment of the cavity.

3. Upon completing the vacuum step, reinstalling all optics, including the MOT, FORT, probe, and data collection components. This process involves searching for the MOT signal or atom loading events, which can extend over several additional weeks.

An alternative strategy to evaluate the induced phase shift involves using of a Mach-Zehnder interferometer [87] in conjunction with the atom–cavity system (see Figure 5.20). In one arm of the Mach-Zehnder interferometer, the atom–cavity interaction is employed to induce the phase shift. State preparation is achieved solely through optical pumping techniques, eliminating the necessity for Zeeman splitting. This technique selectively populates specific hyperfine states within the Rubidium atoms, such as $5S_{1/2}$ $F = 2$ serving as the resonant state and $5S_{1/2}$ $F = 1$ as the dark state. The induced phase shift profile of the atom–cavity system is then obtained from the interferometer's interference pattern for different probe beam frequencies. Simply probing the atom–cavity system alone would not produce any interference pattern due to the vacuum Rabi splitting, highlighting the need to scan the probe beam frequency to obtain the phase profile. This integrated approach, combining an interferometer and state preparation without Zeeman splitting, establishes a versatile platform for characterising the induced phase shift in our magnetically sensitive system, while waiting for another non-magnetic cavity stage to be built for the implementation of a controlled phase gate. Note that other interferometer configurations, such as the Michelson configuration, would also be viable.

Chapter 6

Conclusion

A NC cavity presents appealing properties to study and engineer atom–light interaction. An advantage is the optical access between its mirrors, simplifying the integration of lasers for atom manipulation. The small mode volume inherent to its design enables competitive performance with other high finesse resonators, like micro-cavities, while only requiring low finesse to operate. As the cavity length nears concentricity, the mode volume decreases, enhancing the atom–light coupling strength. However, the main drawback of the NC system lies in its heightened susceptibility to misalignment, both longitudinally and transversely, as the mode volume decreases.

In this thesis, we presented a NC cavity designed to address the fundamental challenge of stabilisation along the spatial three degrees of freedom. Employing a compact cage-like tensegrity mirror support structure, the NC cavity utilises piezoelectric actuators as compression elements and springs as tension elements. This arrangement enables correction for longitudinal and transverse misalignment through tip-tilt motion of the two mirror positions. With a cavity length of approximately 11 mm, the structure demonstrates a residual cavity length variation of $\delta L_{C,rms} = 0.36(2)\,\text{Å}$ at a critical distance $d = 1.06(5)\,\mu\text{m}$ from the concentric regime. While implementing an active cavity length stabilisation would further mitigate susceptibility to external noise, the current level is sufficient to achieve the strong coupling regime with trapped Rubidium atoms. This study has been published in the Review of Scientific Instruments [60].

Through multiple iterations and thorough testing of the tensegrity structure configuration, we have gained a comprehensive understanding of the cavity structure, leading to a well-defined assembly protocol. This proficiency allows us to construct a NC cavity and place it into a vacuum of 10^{-7} Torr before undergoing baking to reach UHV within four days. Moreover, the tensegrity structure exhibits an enhanced performance in terms of susceptibility to external noise, resulting in a tenfold reduction compared to earlier revisions of the NC cavity. Leveraging this passive stability, we can exploit our low cavity finesse to attain atom–cavity coupling in the strong coupling regime.

The characteristic signature of atom–cavity interaction, namely the vacuum Rabi splitting, has been observed for different numbers of Rubidium atoms trapped within the NC cavity. Subsequently, we extract the coupling strength of the system from this splitting, yielding a value of $g_{10} = 2\pi \times 25.4(4)$ MHz for 10 atoms trapped at a critical distance of $d = 1.42(5)$ µm. From the coupling strength g_N and cavity losses κ, we obtain a cooperativity of $C = 5.1(5)$, satisfying the conditions $g_{10}/\kappa > 1$ and $g_{10}/\gamma > 1$, indicating that the atom–cavity system is in the strong coupling regime. Notably, the coupling strength g_N varies with the critical distance and the number of trapped atoms in the cavity. While a single atom interaction illustrates the minimum atom number for realising atom–cavity coupling, exploring experiments with higher atom numbers would offer increased cooperativity and allow the study of interactions with multiple trapped atoms.

Following the vacuum Rabi splitting, which serves as the initial step towards the realisation of quantum logic gates, a crucial parameter to investigate is the induced phase shift by the atom–cavity system on an incoming photon. Consequently, the subsequent objective with the system is to implement a controlled phase gate for characterising this phase shift. Several approaches can be considered. One approach involves driving coherent Zeeman sublevels in the Rubidium atomic spectrum. However, this method requires a varying magnetic field during the measurement sequence, which is not feasible with the current cavity structure as its tension members exhibit a ferromagnetic response. Although a straightforward solution is to replace the ferromagnetic components, the lead time for obtaining these parts may introduce some delays. Alternatively, a more direct option is to utilise an interferometer, where the atom–cavity system modifies the phase in one of the arms, and the phase shift is deduced from the interference fringes.

The NC cavity geometry is a promising platform, offering a viable alternative to high finesse cavity configurations for cavity-QED experiments. The optical access to the center of the cavity mode, facilitated by the NC geometry, is valuable for tasks such as atomic state preparation and atom probing in quantum information processing schemes. An interesting avenue to explore involves constructing atomic arrays within the cavity, allowing for the study of collective atom behavior in the cavity mode. Furthermore, exploiting the degeneracy of modes in the NC regime opens up possibilities to target different atoms trapped at distinct positions with various Laguerre-Gaussian modes, enabling the encoding of diverse information in these modes. Additionally, the passive stability of our cavity paves the way for enhancing the resonator's finesse while keeping the cavity stable in relation to its linewidth, such that the system can operate effectively up to the concentric regime. The increase in finesse offers access to stronger atom–light interactions at short critical distances, providing a valuable avenue for further exploration of the close NC regime and implementation of quantum logic gates in this regime.

Bibliography

[1] A. A. Michelson, "The relative motion of the earth and of the luminiferous ether", *American Journal of Science*, vol. s3-22, no. 128, pp. 120–129, Aug. 1, 1881.

[2] A. A. Michelson and E. W. Morley, "On the relative motion of the earth and the luminiferous ether", *American Journal of Science*, vol. s3-34, no. 203, pp. 333–345, Nov. 1, 1887.

[3] H. R. Brown, "The origins of length contraction: I. The FitzGerald–Lorentz deformation hypothesis", *American Journal of Physics*, vol. 69, no. 10, pp. 1044–1054, Oct. 2001, ISSN: 0002-9505. eprint: `https://pubs.aip.org/aapt/ajp/article-pdf/69/10/1044/7528950/1044\_1\_online.pdf`. [Online]. Available: `https://doi.org/10.1119/1.1379733`.

[4] A. Einstein, "Zur elektrodynamik bewegter körper", *Annalen der Physik*, vol. 322, no. 10, pp. 891–921, 1905. eprint: `https://onlinelibrary.wiley.com/doi/pdf/10.1002/andp.19053221004`. [Online]. Available: `https://onlinelibrary.wiley.com/doi/abs/10.1002/andp.19053221004`.

[5] A. Einstein, "Die grundlage der allgemeinen relativitätstheorie", *Annalen der Physik*, vol. 354, no. 7, pp. 769–822, 1916. eprint: `https://onlinelibrary.wiley.com/doi/pdf/10.1002/andp.19163540702`. [Online]. Available: `https://onlinelibrary.wiley.com/doi/abs/10.1002/andp.19163540702`.

[6] J. J. T. M. F.R.S., "Xl. cathode rays", *The London, Edinburgh, and Dublin Philosophical Magazine and Journal of Science*, vol. 44, no. 269, pp. 293–316, 1897. eprint: `https://doi.org/10.1080/14786449708621070`. [Online]. Available: `https://doi.org/10.1080/14786449708621070`.

[7] P. E. R. F.R.S., "Lxxix. the scattering of alpha and beta particles by matter and the structure of the atom", *The London, Edinburgh, and Dublin Philosophical Magazine and Journal of Science*, vol. 21, no. 125, pp. 669–688, 1911. eprint:

https://doi.org/10.1080/14786440508637080. [Online]. Available: https://doi.org/10.1080/14786440508637080.

[8] N. B. D. phil., "I. on the constitution of atoms and molecules", *The London, Edinburgh, and Dublin Philosophical Magazine and Journal of Science*, vol. 26, no. 151, pp. 1–25, 1913. eprint: https://doi.org/10.1080/14786441308634955. [Online]. Available: https://doi.org/10.1080/14786441308634955.

[9] W. Wien, "Xxx. on the division of energy in the emission-spectrum of a black body", *The London, Edinburgh, and Dublin Philosophical Magazine and Journal of Science*, vol. 43, no. 262, pp. 214–220, 1897. eprint: https://doi.org/10.1080/14786449708620983. [Online]. Available: https://doi.org/10.1080/14786449708620983.

[10] L. R. F.R.S., "Liii. remarks upon the law of complete radiation", *The London, Edinburgh, and Dublin Philosophical Magazine and Journal of Science*, vol. 49, no. 301, pp. 539–540, 1900. eprint: https://doi.org/10.1080/14786440009463878. [Online]. Available: https://doi.org/10.1080/14786440009463878.

[11] A. Einstein, "Über einen die erzeugung und verwandlung des lichtes betreffenden heuristischen gesichtspunkt", *Annalen der Physik*, vol. 322, no. 6, pp. 132–148, 1905. eprint: https://onlinelibrary.wiley.com/doi/pdf/10.1002/andp.19053220607. [Online]. Available: https://onlinelibrary.wiley.com/doi/abs/10.1002/andp.19053220607.

[12] M. Planck, "Ueber das gesetz der energieverteilung im normalspectrum", *Annalen der Physik*, vol. 309, no. 3, pp. 553–563, 1901. eprint: https://onlinelibrary.wiley.com/doi/pdf/10.1002/andp.19013090310. [Online]. Available: https://onlinelibrary.wiley.com/doi/abs/10.1002/andp.19013090310.

[13] L. DE BROGLIE, "Waves and quanta", *Nature*, vol. 112, no. 2815, pp. 540–540, Oct. 1923, ISSN: 1476-4687. [Online]. Available: https://doi.org/10.1038/112540a0.

[14] E. Schrödinger, "An undulatory theory of the mechanics of atoms and molecules", *Phys. Rev.*, vol. 28, pp. 1049–1070, 6 Dec. 1926. [Online]. Available: https://link.aps.org/doi/10.1103/PhysRev.28.1049.

[15] W. Heisenberg, "Über quantentheoretische umdeutung kinematischer und mechanischer beziehungen." *Zeitschrift für Physik*, vol. 33, no. 1, pp. 879–893, Dec. 1925, ISSN: 0044-3328. [Online]. Available: https://doi.org/10.1007/BF01328377.

[16] P. A. M. Dirac and R. H. Fowler, "A theory of electrons and protons", *Proceedings of the Royal Society of London. Series A, Containing Papers of a Mathematical and Physical Character*, vol. 126, no. 801, pp. 360–365, 1930. eprint: https://royalsocietypublishing.org/doi/pdf/10.1098/rspa.1930.0013. [Online]. Available: https://royalsocietypublishing.org/doi/abs/10.1098/rspa.1930.0013.

[17] J. v. Neumann, "Physical applications of the ergodic hypothesis", *Proceedings of the National Academy of Sciences*, vol. 18, no. 3, pp. 263–266, 1932. eprint: https://www.pnas.org/doi/pdf/10.1073/pnas.18.3.263. [Online]. Available: https://www.pnas.org/doi/abs/10.1073/pnas.18.3.263.

[18] T. Hänsch and A. Schawlow, "Cooling of gases by laser radiation", *Optics Communications*, vol. 13, no. 1, pp. 68–69, 1975, ISSN: 0030-4018. [Online]. Available: https://www.sciencedirect.com/science/article/pii/0030401875901595.

[19] W. D. Phillips and H. Metcalf, "Laser deceleration of an atomic beam", *Phys. Rev. Lett.*, vol. 48, pp. 596–599, 9 Mar. 1982. [Online]. Available: https://link.aps.org/doi/10.1103/PhysRevLett.48.596.

[20] S. Chu, L. Hollberg, J. E. Bjorkholm, A. Cable, and A. Ashkin, "Three-dimensional viscous confinement and cooling of atoms by resonance radiation pressure", *Phys. Rev. Lett.*, vol. 55, pp. 48–51, 1 Jul. 1985. [Online]. Available: https://link.aps.org/doi/10.1103/PhysRevLett.55.48.

[21] E. L. Raab, M. Prentiss, A. Cable, S. Chu, and D. E. Pritchard, "Trapping of neutral sodium atoms with radiation pressure", *Phys. Rev. Lett.*, vol. 59,

pp. 2631–2634, 23 Dec. 1987. [Online]. Available: https://link.aps.org/doi/10.1103/PhysRevLett.59.2631.

[22] S. S. Schweber, "QED and the Men Who Made It: Dyson, Feynman, Schwinger, and Tomonaga", Princeton University Press, 1994, vol. 104, ISBN: 9780691036854. [Online]. Available: http://www.jstor.org/stable/j.ctv10crg18 (visited on 09/15/2023).

[23] E. Jaynes and F. Cummings, "Comparison of quantum and semiclassical radiation theories with application to the beam maser", *Proceedings of the IEEE*, vol. 51, no. 1, pp. 89–109, 1963.

[24] S. Haroche, "Nobel lecture: Controlling photons in a box and exploring the quantum to classical boundary", *Rev. Mod. Phys.*, vol. 85, pp. 1083–1102, 3 Jul. 2013. [Online]. Available: https://link.aps.org/doi/10.1103/RevModPhys.85.1083.

[25] J. Ye, D. W. Vernooy, and H. J. Kimble, "Trapping of single atoms in cavity qed", *Phys. Rev. Lett.*, vol. 83, pp. 4987–4990, 24 Dec. 1999. [Online]. Available: https://link.aps.org/doi/10.1103/PhysRevLett.83.4987.

[26] A. Reiserer and G. Rempe, "Cavity-based quantum networks with single atoms and optical photons", *Rev. Mod. Phys.*, vol. 87, pp. 1379–1418, 4 Dec. 2015. [Online]. Available: https://link.aps.org/doi/10.1103/RevModPhys.87.1379.

[27] M. Sumetsky, "Optical bottle microresonators", *Progress in Quantum Electronics*, vol. 64, pp. 1–30, 2019, ISSN: 0079-6727. [Online]. Available: https://www.sciencedirect.com/science/article/pii/S0079672719300072.

[28] Y.-n. Zhang, Y. Zhao, and R.-q. Lv, "A review for optical sensors based on photonic crystal cavities", *Sensors and Actuators A: Physical*, vol. 233, pp. 374–389, 2015, ISSN: 0924-4247. [Online]. Available: https://www.sciencedirect.com/science/article/pii/S0924424715300790.

[29] C. J. Villas-Boas, K. N. Tolazzi, B. Wang, C. Ianzano, and G. Rempe, "Continuous generation of quantum light from a single ground-state atom in an optical cavity", *Phys. Rev. Lett.*, vol. 124, p. 093 603, 9 Mar. 2020. [Online]. Available: https://link.aps.org/doi/10.1103/PhysRevLett.124.093603.

[30] Z. Yan, J. Ho, Y.-H. Lu, S. J. Masson, A. Asenjo-Garcia, and D. M. Stamper-Kurn, "Super-radiant and sub-radiant cavity scattering by atom arrays", 2023. arXiv: 2307.13321 [quant-ph].

[31] M. Baghdad, P.-A. Bourdel, S. Schwartz, F. Ferri, J. Reichel, and R. Long, "Spectral engineering of cavity-protected polaritons in an atomic ensemble", *Nature Physics*, vol. 19, no. 8, pp. 1104–1109, Aug. 2023, ISSN: 1745-2481. [Online]. Available: https://doi.org/10.1038/s41567-023-02035-1.

[32] S. Welte, B. Hacker, S. Daiss, S. Ritter, and G. Rempe, "Photon-mediated quantum gate between two neutral atoms in an optical cavity", *Phys. Rev. X*, vol. 8, p. 011 018, 1 Feb. 2018. [Online]. Available: https://link.aps.org/doi/10.1103/PhysRevX.8.011018.

[33] A. Blais, A. L. Grimsmo, S. M. Girvin, and A. Wallraff, "Circuit quantum electrodynamics", *Rev. Mod. Phys.*, vol. 93, p. 025 005, 2 May 2021. [Online]. Available: https://link.aps.org/doi/10.1103/RevModPhys.93.025005.

[34] J. P. Covey, H. Weinfurter, and H. Bernien, "Quantum networks with neutral atom processing nodes", *npj Quantum Information*, vol. 9, no. 1, p. 90, Sep. 2023, ISSN: 2056-6387. [Online]. Available: https://doi.org/10.1038/s41534-023-00759-9.

[35] L. J. Stephenson, D. P. Nadlinger, B. C. Nichol, S. An, P. Drmota, T. G. Ballance, K. Thirumalai, J. F. Goodwin, D. M. Lucas, and C. J. Ballance, "High-rate, high-fidelity entanglement of qubits across an elementary quantum network", *Phys. Rev. Lett.*, vol. 124, p. 110 501, 11 Mar. 2020. [Online]. Available: https://link.aps.org/doi/10.1103/PhysRevLett.124.110501.

[36] H. J. Kimble, "The quantum internet", *Nature*, vol. 453, no. 7198, pp. 1023–1030, Jun. 2008. [Online]. Available: https://doi.org/10.1038/nature07127.

[37] A. Reiserer, "Colloquium: Cavity-enhanced quantum network nodes", *Rev. Mod. Phys.*, vol. 94, p. 041 003, 4 Dec. 2022. [Online]. Available: https://link.aps.org/doi/10.1103/RevModPhys.94.041003.

[38] E. Jaynes and F. Cummings, "Comparison of quantum and semiclassical radiation theories with application to the beam maser", *Proceedings of the IEEE*, vol. 51, no. 1, pp. 89–109, 1963.

[39] K. DURAK, "A Diffraction Limited Fabry-Pérot Cavity with a Strongly Focused Mode", Ph.D. dissertation, CQT, National University of Singapore, 2014.

[40] Y. Zhu, D. J. Gauthier, S. E. Morin, Q. Wu, H. J. Carmichael, and T. W. Mossberg, "Vacuum rabi splitting as a feature of linear-dispersion theory: Analysis and experimental observations", *Phys. Rev. Lett.*, vol. 64, pp. 2499–2502, 21 May 1990. [Online]. Available: `https://link.aps.org/doi/10.1103/PhysRevLett.64.2499`.

[41] K. M. Birnbaum, A. Boca, R. Miller, A. D. Boozer, T. E. Northup, and H. J. Kimble, "Photon blockade in an optical cavity with one trapped atom", *Nature*, vol. 436, no. 7047, pp. 87–90, Jul. 2005, ISSN: 1476-4687. [Online]. Available: `https://doi.org/10.1038/nature03804`.

[42] R. Loudon, "The quantum theory of light", OUP Oxford, 2000.

[43] H. J. Carmichael, "Statistical Methods in Quantum Optics 1: Master Equations and Fokker-Planck Equations", Springer Berlin, Heidelberg, 1998.

[44] Z. Moktadir, E. Koukharenka, M. Kraft, D. M. Bagnall, H. Powell, M. Jones, and E. A. Hinds, "Etching techniques for realizing optical micro-cavity atom traps on silicon", *Journal of Micromechanics and Microengineering*, vol. 14, no. 9, S82, Aug. 2004. [Online]. Available: `https://dx.doi.org/10.1088/0960-1317/14/9/014`.

[45] Y.-H. Lien, G. Barontini, M. Scheucher, M. Mergenthaler, J. Goldwin, and E. A. Hinds, "Observing coherence effects in an overdamped quantum system", *Nature Communications*, vol. 7, no. 1, p. 13 933, Dec. 2016, ISSN: 2041-1723. [Online]. Available: `https://doi.org/10.1038/ncomms13933`.

[46] E. M. Purcell, "Spontaneous Emission Probabilities at Radio Frequencies", *Physical Review*, vol. 69, p. 681, 1946. [Online]. Available: `http://link.aps.org/doi/10.1103/PhysRev.69.674.2`.

[47] D. Kleppner, "Inhibited spontaneous emission", *Phys. Rev. Lett.*, vol. 47, pp. 233–236, 4 Jul. 1981. [Online]. Available: `https://link.aps.org/doi/10.1103/PhysRevLett.47.233`.

[48] S. Haroche and J.-M. Raimond, “Exploring the Quantum: Atoms, Cavities, and Photons”, OUP Oxford, 2013.

[49] H. J. Kimble, “Strong interactions of single atoms and photons in cavity qed”, *Physica Scripta*, vol. 1998, no. T76, p. 127, Jan. 1998. [Online]. Available: `https://dx.doi.org/10.1238/Physica.Topical.076a00127`.

[50] A. Kuhn, M. Hennrich, and G. Rempe, “Deterministic single-photon source for distributed quantum networking”, *Phys. Rev. Lett.*, vol. 89, p. 067 901, 6 Jul. 2002. [Online]. Available: `https://link.aps.org/doi/10.1103/PhysRevLett.89.067901`.

[51] M. Tavis and F. W. Cummings, “Exact solution for an N-molecule—radiation-field hamiltonian”, *Phys. Rev.*, vol. 170, pp. 379–384, 2 Jun. 1968. [Online]. Available: `https://link.aps.org/doi/10.1103/PhysRev.170.379`.

[52] H. Tanji-Suzuki, I. D. Leroux, M. H. Schleier-Smith, M. Cetina, A. T. Grier, J. Simon, and V. Vuletić, “Chapter 4 - interaction between atomic ensembles and optical resonators: Classical description”, in *Advances in Atomic, Molecular, and Optical Physics*, ser. Advances In Atomic, Molecular, and Optical Physics, E. Arimondo, P. Berman, and C. Lin, Eds., vol. 60, Academic Press, 2011, pp. 201–237. [Online]. Available: `https://www.sciencedirect.com/science/article/pii/B9780123855084000048`.

[53] A. E. Siegman, “Lasers”, University Science Books, 1986.

[54] S. J. van Enk and H. J. Kimble, “Single atom in free space as a quantum aperture”, *Phys. Rev. A*, vol. 61, p. 051 802, 5 Mar. 2000. [Online]. Available: `https://link.aps.org/doi/10.1103/PhysRevA.61.051802`.

[55] C. J. Hood, H. J. Kimble, and J. Ye, “Characterization of high-finesse mirrors: Loss, phase shifts, and mode structure in an optical cavity”, *Phys. Rev. A*, vol. 64, p. 033 804, 3 Aug. 2001. [Online]. Available: `https://link.aps.org/doi/10.1103/PhysRevA.64.033804`.

[56] B. E. A. Saleh and M. C. Teich, “Fundamentals of Photonics”, eng, 3rd ed. Newark: John Wiley & Sons, Incorporated Newark, 2019, ISBN: 9781118770092; 1118770099; 9781119506928; 1119506921; 9781118770061; 1118770064.

[57] H. Laabs and A. Friberg, "Nonparaxial eigenmodes of stable resonators", *IEEE Journal of Quantum Electronics*, vol. 35, no. 2, pp. 198–207, 1999.

[58] C. H. NGUYEN, "Single Atoms Coupled to a Near-Concentric Cavity", Ph.D. dissertation, CQT, National University of Singapore, 2018.

[59] A. N. UTAMA, "Near-Concentric Optical Resonator for Coherent Atom-Photon Interaction", Ph.D. dissertation, CQT, National University of Singapore, 2021.

[60] F. Adam, W. X. Chiew, A. N. Utama, and C. Kurtsiefer, "Low noise near-concentric optical cavity design", *Review of Scientific Instruments*, vol. 95, no. 4, p. 043 102, Apr. 2024, ISSN: 0034-6748. eprint: `https://pubs.aip.org/aip/rsi/article-pdf/doi/10.1063/5.0191123/19878604/043102\_1\_5.0191123.pdf`. [Online]. Available: `https://doi.org/10.1063/5.0191123`.

[61] C. D. Wallace, T. P. Dinneen, K. Y. N. Tan, A. Kumarakrishnan, P. L. Gould, and J. Javanainen, "Measurements of temperature and spring constant in a magneto-optical trap", *J. Opt. Soc. Am. B*, vol. 11, no. 5, pp. 703–711, May 1994. [Online]. Available: `https://opg.optica.org/josab/abstract.cfm?URI=josab-11-5-703`.

[62] R. Grimm, M. Weidemüller, and Y. B. Ovchinnikov, "Optical dipole traps for neutral atoms", in ser. Advances In Atomic, Molecular, and Optical Physics, B. Bederson and H. Walther, Eds., vol. 42, Academic Press, 2000, pp. 95–170. [Online]. Available: `https://www.sciencedirect.com/science/article/pii/S1049250X0860186X`.

[63] I. Sahl, "On burning mirrors and lenses",, 984.

[64] R. Rashed, "A pioneer in anaclastics: Ibn sahl on burning mirrors and lenses", *Isis*, vol. 81, no. 3, pp. 464–491, 1990, ISSN: 00211753, 15456994. [Online]. Available: `http://www.jstor.org/stable/233423` (visited on 10/20/2023).

[65] D. A. Steck, "Rubidium 87 d line data",, 2001.

[66] C. H. Nguyen, A. N. Utama, N. Lewty, K. Durak, G. Maslennikov, S. Straupe, M. Steiner, and C. Kurtsiefer, "Single atoms coupled to a near-concentric cavity", *Phys. Rev. A*, vol. 96, p. 031 802, 3 Sep. 2017. [Online]. Available: `https://link.aps.org/doi/10.1103/PhysRevA.96.031802`.

[67] C. H. Nguyen, A. N. Utama, N. Lewty, and C. Kurtsiefer, “Operating a near-concentric cavity at the last stable resonance”, *Phys. Rev. A*, vol. 98, p. 063 833, 6 Dec. 2018. [Online]. Available: `https://link.aps.org/doi/10.1103/PhysRevA.98.063833`.

[68] A. N. Utama, C. H. Chow, C. H. Nguyen, and C. Kurtsiefer, “Coupling light to higher order transverse modes of a near-concentric optical cavity”, *Opt. Express*, vol. 29, no. 6, pp. 8130–8141, Mar. 2021. [Online]. Available: `https://opg.optica.org/oe/abstract.cfm?URI=oe-29-6-8130`.

[69] Y. K. Yong, S. O. R. Moheimani, B. J. Kenton, and K. K. Leang, “Invited Review Article: High-speed flexure-guided nanopositioning: Mechanical design and control issues”, *Review of Scientific Instruments*, vol. 83, no. 12, p. 121 101, Dec. 2012, ISSN: 0034-6748. eprint: `https://pubs.aip.org/aip/rsi/article-pdf/doi/10.1063/1.4765048/15765535/121101\_1\_online.pdf`. [Online]. Available: `https://doi.org/10.1063/1.4765048`.

[70] R. Skelton, R. Adhikari, J.-P. Pinaud, W. Chan, and J. Helton, “An introduction to the mechanics of tensegrity structures”, in *Proceedings of the 40th IEEE Conference on Decision and Control (Cat. No.01CH37228)*, vol. 5, 2001, 4254–4259 vol.5.

[71] C. Klempt, T. van Zoest, T. Henninger, O. Topic, E. Rasel, W. Ertmer, and J. Arlt, “Ultraviolet light-induced atom desorption for large rubidium and potassium magneto-optical traps”, *Phys. Rev. A*, vol. 73, p. 013 410, 1 Jan. 2006. [Online]. Available: `https://link.aps.org/doi/10.1103/PhysRevA.73.013410`.

[72] A. S. Arnold, J. S. Wilson, and M. G. Boshier, “A simple extended-cavity diode laser”, *Review of Scientific Instruments*, vol. 69, no. 3, pp. 1236–1239, Mar. 1998, ISSN: 0034-6748. eprint: `https://pubs.aip.org/aip/rsi/article-pdf/69/3/1236/11171804/1236\_1\_online.pdf`. [Online]. Available: `https://doi.org/10.1063/1.1148756`.

[73] J. L. Hall, L. Hollberg, T. Baer, and H. G. Robinson, “Optical heterodyne saturation spectroscopy”, *Applied Physics Letters*, vol. 39, no. 9, pp. 680–682, Nov. 1981, ISSN: 0003-6951. eprint: `https://pubs.aip.org/aip/apl/`

article-pdf/39/9/680/7747736/680_1_online.pdf. [Online]. Available: https://doi.org/10.1063/1.92867.

[74] R. W. P. Drever, J. L. Hall, F. V. Kowalski, J. Hough, G. M. Ford, A. J. Munley, and H. Ward, "Laser phase and frequency stabilization using an optical resonator", *Applied Physics B*, vol. 31, no. 2, pp. 97–105, Jun. 1983, ISSN: 1432-0649. [Online]. Available: https://doi.org/10.1007/BF00702605.

[75] G. C. Bjorklund, "Frequency-modulation spectroscopy: A new method for measuring weak absorptions and dispersions", *Opt. Lett.*, vol. 5, no. 1, pp. 15–17, Jan. 1980. [Online]. Available: https://opg.optica.org/ol/abstract.cfm?URI=ol-5-1-15.

[76] D. J. McCarron, S. A. King, and S. L. Cornish, "Modulation transfer spectroscopy in atomic rubidium", *Measurement Science and Technology*, vol. 19, no. 10, p. 105 601, Aug. 2008. [Online]. Available: https://dx.doi.org/10.1088/0957-0233/19/10/105601.

[77] X.-S. Yang and S. Koziel, "Introduction to optimization and gradient-based methods", in *Simulation-Driven Design Optimization and Modeling for Microwave Engineering*, pp. 1–18. eprint: https://www.worldscientific.com/doi/pdf/10.1142/9781848169173_0001. [Online]. Available: https://www.worldscientific.com/doi/abs/10.1142/9781848169173_0001.

[78] G. L. Gattobigio, T. Pohl, G. Labeyrie, and R. Kaiser, "Scaling laws for large magneto-optical traps", *Physica Scripta*, vol. 81, no. 2, p. 025 301, Feb. 2010. [Online]. Available: https://dx.doi.org/10.1088/0031-8949/81/02/025301.

[79] N. Schlosser, G. Reymond, and P. Grangier, "Collisional blockade in microscopic optical dipole traps", *Phys. Rev. Lett.*, vol. 89, p. 023 005, 2 Jun. 2002. [Online]. Available: https://link.aps.org/doi/10.1103/PhysRevLett.89.023005.

[80] T. Angel, "Formation of martensite in austenitic stainless steels effects of deformation, temperature, and composition", *J. Iron and Steel Inst.*, vol. 177, pp. 165–174, 1954.

[81] R. Stringfellow, D. Parks, and G. Olson, "A constitutive model for transformation plasticity accompanying strain-induced martensitic transformations in metastable austenitic steels", *Acta Metallurgica et Materialia*, vol. 40, no. 7, pp. 1703–1716, 1992, ISSN: 0956-7151. [Online]. Available: `https://www.sciencedirect.com/science/article/pii/095671519290114T`.

[82] K. Kieling, J. L. O'Brien, and J. Eisert, "On photonic controlled phase gates", *New Journal of Physics*, vol. 12, no. 1, p. 013 003, Jan. 2010. [Online]. Available: `https://dx.doi.org/10.1088/1367-2630/12/1/013003`.

[83] A. Reiserer, N. Kalb, G. Rempe, and S. Ritter, "A quantum gate between a flying optical photon and a single trapped atom", *Nature*, vol. 508, no. 7495, pp. 237–240, Apr. 2014, ISSN: 1476-4687. [Online]. Available: `https://doi.org/10.1038/nature13177`.

[84] F. Kimiaee Asadi, S. C. Wein, and C. Simon, "Cavity-assisted controlled phase-flip gates", *Phys. Rev. A*, vol. 102, p. 013 703, 1 Jul. 2020. [Online]. Available: `https://link.aps.org/doi/10.1103/PhysRevA.102.013703`.

[85] A. Durrant, H. Chen, S. Hopkins, and J. Vaccaro, "Zeeman-coherence-induced transparency and gain without inversion in laser-cooled rubidium", *Optics Communications*, vol. 151, no. 1, pp. 136–146, 1998, ISSN: 0030-4018. [Online]. Available: `https://www.sciencedirect.com/science/article/pii/S0030401898000522`.

[86] M. Oberst, F. Vewinger, and A. I. Lvovsky, "Time-resolved probing of the ground state coherence in rubidium", *Opt. Lett.*, vol. 32, no. 12, pp. 1755–1757, Jun. 2007. [Online]. Available: `https://opg.optica.org/ol/abstract.cfm?URI=ol-32-12-1755`.

[87] K. Lemr, A. Černoch, J. Soubusta, K. Kieling, J. Eisert, and M. Du šek, "Experimental implementation of the optimal linear-optical controlled phase gate", *Phys. Rev. Lett.*, vol. 106, p. 013 602, 1 Jan. 2011. [Online]. Available: `https://link.aps.org/doi/10.1103/PhysRevLett.106.013602`.